Performance of a Low-Pressure, Helicon Driven IEC ^{3}He Fusion Device

Gregory R. Piefer

December 2006

UWFDM-1303

Ph.D. thesis.

FUSION TECHNOLOGY INSTITUTE

UNIVERSITY OF WISCONSIN

MADISON WISCONSIN

Performance of a Low-Pressure, Helicon Driven IEC ^{3}He Fusion Device

Gregory R. Piefer

Fusion Technology Institute
University of Wisconsin
1500 Engineering Drive
Madison, WI 53706

http://fti.neep.wisc.edu

December 2006

UWFDM-1303

Ph.D. thesis.

Performance of a Low-Pressure, Helicon Driven IEC ^{3}He Fusion Device

by

Gregory R. Piefer

A dissertation submitted in partial fulfillment of

the requirements for the degree of

Doctor of Philosophy

(Nuclear Engineering & Engineering Physics)

at the

UNIVERSITY OF WISCONSIN-MADISON

2006

Abstract

The study of the $^3He(^3He,2p)^4He$ fusion reaction is interesting for many reasons ranging from nuclear physics to astrophysics to fusion energy. While this reaction has been studied in particle accelerators, its behavior at low energy (< 1 MeV) is not fully characterized due to low accelerator beam currents (< 1 mA) and the low reaction cross-section. The spherical recirculation of ions in an Inertial Electrostatic Confinement (IEC) device offers the potential to explore these reactions at sub MeV energy levels, but with ion currents as high as 100 mA or more. Such a capability would improve counting statistics tremendously, and be a valuable tool for characterizing this reaction at these low energies.

This dissertation focuses on the development of an IEC device toward this end, with the final goal of detecting $^3He(^3He,2p)^4He$ reactions. Many facets of IEC technology were enhanced to accomplish this, and these enhancements will also play a major role in the development of IEC devices for near-term applications.

Some of the major enhancements at the University of Wisconsin IEC facility were:

1. the maximum operating voltage was increased from 55 kV to 170 kV
2. the lifetime of insulators was increased from about 1 month to 6 months
3. a gas recycle system was developed that allowed the reuse of ^3He gas after it flowed through the system
4. a helicon ion source was developed that allowed operation at 1/3 the previous minimum pressure with seven times the current
5. the same helicon ion source was developed to give independent control over the ion current
6. a proton detection system was developed that reduced the noise level in the detection system by two orders of magnitude.

These developments allowed for the detection of $^3He(^3He,2p)^4He$ reactions at the rates of 144 ± 44 reactions / sec at 124 kV, and 400 ± 67 reactions / sec at 134 kV, with a maximum total reactivity of $1.1 * 10^3$ reactions / sec. These results agree to within 50% of the theoretical prediction from the combination of beam-background and beam-embedded fusion, and represent the first time that ^3He-^3He reactions have been observed in an IEC device.

Acknowledgements

Through the years spent on this work, there have been many people who have played roles in shaping the work presented in this dissertation. Some of them have also played a role in shaping my life, and I would very much like to thank them for their influence.

I would like to issue a special thanks to Professor Gerald Kulcinski, for believing in me since the day I first came to ask him about graduate school. He has had a profound impact on my work, as well as my development as a scientist and a person. He taught by instruction and by example, and my life would be quite different if I had chosen another path. I would not have it any other way.

I extend my thanks also to John Santarius, who is quite possibly the most well informed person in our field that I know. In addition to teaching me an uncountable number of scientific methods, John taught me never to jump to conclusions, and to always view things with a sense of humor. I would also like to thank John for his patience and understanding when I would become too convinced by the wrong ideas.

Another person who played a key role in this work was Robert Ashley. I would like to thank Bob for always being supportive, especially when it seemed things were so bad I felt like quitting. He taught me never to give up, but just to step back and take a deep breath when it looked like things couldn't get worse.

I'd like to thank Harrison Schmitt, for being an inspiration to me. He's been an amazing person to work with, and his support can make one believe in even the most impossible dreams. I am so grateful for this, and will always try to keep dreaming.

I’d like to thank Professor Noah Hershkowitz, for giving me the insights and advice I needed to finish my work. His expertise is immense, and his enthusiasm for teaching young minds unparalleled.

This work could not have been accomplished without the help of my fellow students. I’d like to thank Ross Radel, who has been with me from the beginning. He’s been a great friend and co-worker and helped me get through it all. I’d also like to say a thank you to the other students who helped with wonderful ideas and endless hard work. John Weidner, Ben Cipiti, Alex Wehmeyer, Tracy Radel, Kunihiko Tomiyasu, Krupaker M. Subramanian, Dave Boris, Thad Heltemes, Brian Egle, Eric Alderson, Sam Zenobia, and Chris Seyfert, thanks for everything, both the good times and the amazing work.

The staff of the FTI, particularly Joan-Welc Lepain and Dennis Bruggink have been very helpful and even better become great friends. They have been instrumental in making things happen, and I am grateful to have worked with them.

A special thanks goes out to Greg Winz and Paul Nonn, experts not associated with our group who provided a tremendous amount of help out of love for the field. When I didn’t know how to do something, odds are they could come up with something and I am glad they were there when those times came around.

Last, but probably most importantly, I’d like to thank my family; my sisters Kristin and Karen, and my brother Mark for always being there for me; and most importantly my parents, Rick and Judy. They have given me all the opportunities I now have, and made me open as many doors as I could. For believing in me, especially when some said I could never do it, I owe them everything. I could not have asked for a better family.

Finally, I would like to offer my thanks to the groups that have funded my work. Without the generous support of the Grainger Foundation, Wilson Greatbatch, the University of Wisconsin, and the Department of energy, this dissertation would not have been possible. Their dedication to research and the advancement of mankind is without question, and their support moves us all forward.

Table of Contents

Table of Figures

Chapter I

Chapter IV

Chapter V

Chapter VI

Chapter VII

Chapter VIII

Appendix C

Table of Tables

Chapter VI

Chapter VIII

Appendix A

Appendix D

I. Introduction

Since the beginning of written history, people have attempted to find new forms of energy to fuel their needs. Today, the energy challenges for the future are more difficult than they ever have been. A balance must be struck between growing demand, exhausting resources, and preserving the ecology of our environment. A solution that could strike this balance is in sight: nuclear reactions, which generate millions of times more energy for a given amount of fuel than their chemical counterparts [1,2,3], promise massive amounts of energy with very little waste. Nuclear fission reactors, currently used all over the world, and admittedly a very promising solution for the near term, have inherent proliferation risks [2] and safety issues [2,3], and generate radioactive waste [2,3] that make a safer, cleaner solution desirable.

The fusion of light nuclei promises the benefit of nearly unlimited energy to those who can master its challenges. For over half a century these fusion reactions have been studied [4,5,6,7,8], and a world-wide program has been instituted to attempt to harness their energy for use in multiple applications. A tremendous natural resource (in the form of deuterium) exists from which this energy can be created [4,5,6] and the waste products generated are far more benign than those from fission reactions [4,5,6]. Furthermore, the dangers of nuclear proliferation are greatly reduced [4], which is of critical interest in the current political climate.

Among the energy generating fusion reactions, the one between deuterium (D) and tritium (T) has been investigated the most, due to its high probability for fusion at relatively low energies. The reaction sequence is shown in figure I-1:

Figure I-1: D(T,n)^{4}He fusion reaction

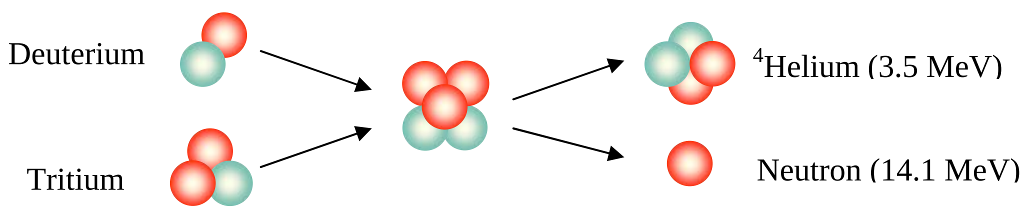

The D-T reaction is frequently called “first-generation”, because most of the first-generation fusion power plant designs use it as the fuel of choice. The D-T cycle is attractive because of its high fusion probability, high energy output, and the high energy neutron it generates can be useful for breeding tritium, and for many near-term applications [9] where the reactor output is less than the power input (Q<1). This same neutron, however, is less desirable in power plants since it can damage the reactor containment vessel and induce large amounts of radioactivity (albeit, with half-lives of 10’s to 100’s of years), as well as restrict energy conversion efficiencies. An additional drawback is that one of the reactants is tritium; a radioactive fuel that does not exist at usable quantities in nature due to its 12.3 year half-life. This necessitates a system for breeding tritium, which dramatically complicates the design of power reactors and introduces hundreds of millions of curies of radioactive material [4,5,6].

Another reaction of interest is the D-D reaction:

Figure I-2: The D(D,n)^{3}He and D(D,p)T fusion reactions

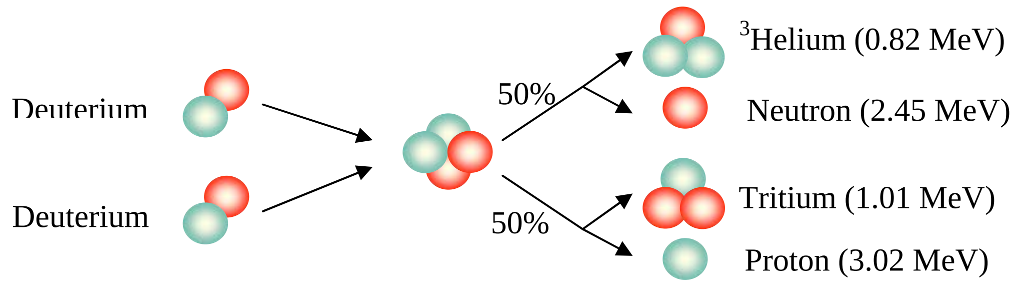

D-D fusion is also referred to as a first-generation fuel, since it also can react at reasonably high rates (Q~1) at relatively low temperatures (~10's of keV) [10]. This reaction produces a neutron 50% of the time, which can be used in some Q<1 near-term applications similarly to the D-T neutron. It also releases a majority (~66%) of the reaction energy in the form of charged particles, which can be directly converted to electricity at high efficiency [11,12]. Unfortunately, since the reaction energy is so low, there are more neutrons generated per kilowatt-hour of fusion energy with D-D than with D-T and activation of the reactor vessel is still a significant problem. Radioactive tritium is also a product, but it should be possible to burn most of this off in the plasma [4]. Finally, D-D reactions are less probable than D-T reactions over typical reactor temperature ranges, and the fusion probability is ~100 times lower in the range of 20-50 keV [10].

The next reaction of interest is the fusion of D with ^{3}He:

Figure I-3: The D(^{3}He,p)^{4}He reaction

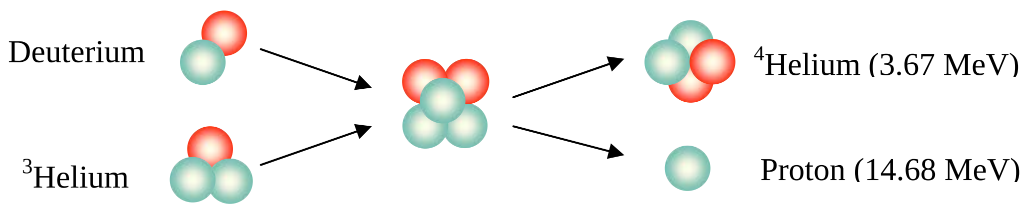

D-^{3}He fusion is referred to as a "second-generation" reaction. It is the easiest reaction to achieve that produces a lower amount of neutrons. While requiring a higher temperature than D-D or D-T, this reaction provides a number of advantages. At Q<1 output levels the high energy proton can be used for many near-term applications [9]. At high power levels, D-^{3}He fusion could eliminate many technical challenges caused by the neutrons generated in the D-T and D-D cycles and provide higher efficiency conversion to electricity. On the other hand, it is very difficult, if not impossible, to cause D-^{3}He reactions without some side D-D reactions occurring as well [4,5]. In fact, Penning ionization of deuterium by excited helium in some reactor designs may actually suppress ^{3}He ionization, causing a greater fraction of D-D reactions than expected [13]. These "side-effect" reactions will introduce some of the difficulties inherent to more neutronic fuel cycles, albeit at a much lower level.

One more reaction of interest is fusion between two ^{3}He atoms:

Figure I-4: The ^{3}He(^{3}He,2p)^{4}He reaction

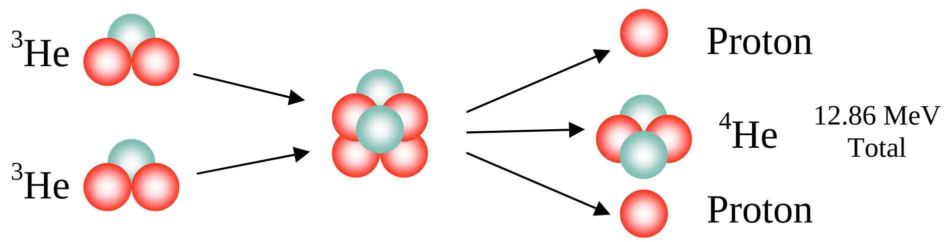

Of all the reactions discussed, ^{3}He-^{3}He it is the most difficult to achieve since the reactants must be brought to extremely high energy for fusion to take place. Like D-^{3}He it is aneutronic, but unlike D-^{3}He, there is no deuterium present to cause side-effect D-D reactions so ^{3}He-^{3}He reactors are almost completely aneutronic. While ^{3}He-^{3}He is too difficult to be considered for low level applications, it offers tremendous potential benefit if it could be used for fusion energy. Since all of the reactants and products in this third generation fuel are stable isotopes, and all of the products are charged particles, ^{3}He-^{3}He fusion could be used to generate electricity at high efficiency with no radioactivity associated with the fuel cycle. Furthermore, this reaction is of interest to nuclear and solar physicists, since its cross-section is poorly measured at low energy and it has been postulated that a resonance may exist below the coulomb barrier [14] that might make it more likely to occur.

This thesis will summarize the development of just one fusion concept, inertial electrostatic confinement (IEC), and the associated technology that could be used to produce ^{3}He-^{3}He fusion reactions. Unique methods to dramatically improve operational space and detection efficiency will be specifically detailed, and experimental measurements of the first $^{3}He(^{3}He,2p)^{4}He$ reactions achieved in an IEC device will be discussed.

I.A. References

[1] J. Orear, “Physics,” Ch. 29, Macmillan Publishing Co., (1979).

[2] Max W. Carbon, “Nuclear Power: Villain or Victim?,” Pebble Beach Publishing, Madison, WI, (1997).

[3] M. M. El-Wakil “Powerplant Technology,” McGraw-Hill, (1984).

[4] W. Hafele, J. P. Holdren, G. Kessler, G. L. Kulcinski, “Fusion and Fast Breeder Reactors,” International Institute for Applied Systems Analysis, (1977).

[5] R. A. Gross, “Fusion Energy,” John Wiley and Sons, (1984).

[6] S. O. Dean, “Prospects for Fusion Power,” Pergamon Press, (1981).

[7] W. M. Stacey Jr, “Fusion An Introduction to the Physics and Technology of Magnetic Confinement Fusion,” John Wiley and Sons, (1984) .

[8] W. J. Hogan, “Energy from Inertial Fusion,” International Atomic Energy Agency, (1995).

[9] G.L. Kulcinski, “Near Term Commercial Opportunities from Long Range Fusion Research,” *Fusion Technology*, **30**, p.411 (December, 1996).

[10] J. R. McNally, “Physics of Fusion Fuel Cycles,” *Nuclear Technology/Fusion*, **2**, [1], p.9 (1982).

[11] R. W. Moir, W. L. Barr, “Venetian-Blind Direct Energy Converter for Fusion Reactors,” *Nuclear Fusion*, **13**, p.35 (1973).

[12] W. L. Barr, R. W. Moir, “Test Results on Plasma Direct Converters,” *Nuclear Technology/Fusion*, **3**, p.98 (Jan. 1983).

[13] H. M. Bevesk and P. E. Siska, “A Vibrationally Adiabatic Theory of Molecular Penning Ionization,” *J. Chem. Phys.*, **102**, [5], p.1934 (Oct. 1994).

[14] V. N. Fetisov, Y. S. Kopysov, “Are the Solar-Neutrino Experiments Suggestive of a Resonance in the $^{3}He + {}^{3}He$ System?,” *Physics Letters*, **40B**, [6], p.602 (Aug. 1972).

II. Conceptual Approach

The production of ^3He-^3He reactions in an IEC device had not been demonstrated before this study, so a conceptual approach was developed to examine the feasibility of these experiments. Previous IEC work had been done on D-T [1,2,3], D-D [1,2,3,4,5,6,7,8,9,10], and D-^3He [9,11,12,13] reactions and the behavior of IEC systems running with these fuel cycles has been fairly well investigated. Since ^3He-^3He reactions are aneutronic, the techniques used for measuring D-D fusion rates, in particular neutron rates were not applicable. Past D-^3He work, however, provided a good starting point to examine the conditions were needed to study the more difficult ^3He-^3He reaction.

Previous IEC experiments at UW had shown that the minimum operating voltage for D-^3He reactions to be detected was around 30 kV. Based on fusion cross-sections, and neglecting all other effects, the approximate operating voltage required to observe ^3He-^3He reactions at a similar rate was 150-200 kV. This threshold presented two major challenges: 1) no IEC device had previously operated at such high voltages, and 2) the experimental facilities available at Wisconsin were limited to 200 kV for the duration of this work. A campaign to operate at voltages this high was very likely to be difficult, so other changes to the D-^3He experimental procedure were required to make sure the reactions were observable.

Previous IEC work with both D-D and D-^{3}He had indicated that at typical operational pressures of around a few mtorr, re-circulating ions frequently collide with background gas [9,13,14,15,16], thereby reducing the average ion energy. Minimizing this effect could increase the average ion energy and hence the ^{3}He-^{3}He reaction rate. In order to do this, the device had to be operated at much lower reaction chamber pressures than were achievable in previous IEC systems, so a campaign to reduce the operational pressure by using external ion sources was needed.

Even if higher voltage and lower pressure could be achieved in present IEC configurations, it was likely that ^{3}He-^{3}He reaction rates would still be very low due to power supply limitation of 200 kV. In order to get good statistics, long runtimes were required. Earlier IEC systems at UW were only capable of running for periods of up to 30 minutes due to heating of the chamber walls, and therefore a new system was needed to allow longer runtimes. Furthermore, past work indicated that contamination from deuterium in previous IEC systems would cause D-^{3}He reactions that would interfere with the ability to observe the much rarer ^{3}He-^{3}He reactions. The combination of these requirements meant that a campaign to set up a new IEC experimental facility was needed as well.

The ability to run for long time periods brought with it another concern. The expense (~$1000/gram) and rarity of ^{3}He gas meant that run time would be cost limited, even if the system could take the heat load. Therefore, a campaign to allow re-use of ^{3}He once it had flowed through the system was also required. This system needed to filter out impurities caused by operation, but allow ^{3}He to recycle-a technique used by others, but which had not been tested in the environment of an IEC device.

Operation at high voltage brought with it an additional complication. Operation of an IEC device at the proposed voltages (>100 kV in a plasma environment) generates electrical instabilities that create electromagnetic pulses. When such pulses are generated near a charged particle detector, broadband noise signals are created which are interpreted falsely by detection software to be protons of varying energy. These false counts turn out to far outnumber the number of counts expected, so a campaign to suppress the contribution from unstable operation was required. Furthermore, even if arcs were suppressed, radiation from x-ray pile-up, protons generated from D-^{3}He reactions due to the natural abundance of deuterium in water, and background radiation could call into doubt whether or not what we observed truly were ^{3}He-^{3}He reactions. The new detection system had to deal with all of these issues.

If all of these challenges could be overcome, it would be possible to observe ^{3}He-^{3}He reactions in an IEC device at steady state ion currents in the 10's to 100's of mA, which are not achievable in particle accelerators. This, coupled with a good understanding of ion recirculation could lead to very accurate cross-section measurements below 1 MeV and allow for certain suspected resonance phenomena to be investigated. Additionally, the development of the systems required to make ^{3}He-^{3}He observable would provide a tremendous boost to existing IEC capabilities and greatly improve the usefulness of the concept to certain near-term applications such as the detection of clandestine materials or the generation of medical isotopes.

II.A. References

[1] Winfield W. Salisbury, "Method and Apparatus for producing Neutrons," United States Patent Office #2,489,436, December 17, 1947.

[2] Philo T. Farnsworth, "Electric Discharge Device for Producing Interactions Between Nuclei," United States Patent Office #3,258,402, June 28, 1966.

[3] R.L. Hirsch, "Inertial-Electrostatic Confinement of Ionized Fusion Gases," *Journal of Applied Physics*, **38**, 4522 (1967).

[4] G.H. Miley et al., "Inertial Electrostatic Confinement: An Approach to Burning Advanced Fuels," *Fusion Technology,* **19**, 840 (May, 1991).

[5] M. Ohnishi et al., "Beam Optics in Inertial Electrostatic Confinement Fusion," *Review of Scientific Instruments,* **71,** [2], 1210 (February, 2000).

[6] K. Yamauchi et al., "Neutron Production Characteristics and Emission Properties of Spherically Convergent Beam Fusion," *Fusion Technology,* **39,** [3], 1182 (May, 2001).

[7] T. A. Thorson, "Ion Flow and Fusion Reactivity Characterization of a Spherically Convergent Ion Focus," PhD thesis, University of Wisconsin—Madison (1994).

[8] Y. Gu, "Experimental Study of Proton Rate Density in a Spherical Inertial Electrostatic Confinement Fusion Device," PhD thesis, University of Illinois (1998).

[9] K. M. Subramanian, "Diagnostic Study of Advanced Fuel (D-D and D-3He) Fusion in an IEC Device," PhD thesis, University of Wisconsin—Madison (2004).

[10] A. L. Wehmeyer, "The Detection of Explosives Using an Inertial Electrostatic Confinement D-D Fusion Device," Masters thesis, University of Wisconsin (2005).

[11] R.P. Ashley et al., "Steady State D-^{3}He Proton Production in an IEC Device," *Fusion Technology*, **39**, p.546 (2001).

[12] J.W. Weidner, "The Production of ^{13}N from Inertial Electrostatic Confinement Fusion," Master's Thesis, University of Wisconsin-Madison (2003).

[13] B. B. Cipiti, "The Fusion of Advanced Fuels to Produce Medical Isotopes Using Inertial Electrostatic Confinement," PhD thesis, University of Wisconsin—Madison (2004).

[14] G.A. Emmert and J.F. Santarius, “A Charge-Exchange Based Model for the Performance of Gridded, Spherical IEC Devices. Part I: single species atomic ions”, University of Wisconsin, (in preparation, 2006).

[15] G.A. Emmert and J.F. Santarius, “A Charge-Exchange Based Model for the Performance of Gridded, Spherical IEC Devices. Part II: molecular ions”, University of Wisconsin, (in preparation, 2006).

[16] K. Tomiyasu, “Numerical Simulation for UW-IEC Device,” Masters Thesis, Tokyo Institute of Technology, (2003).

III. Previous Work

III.A. IEC

III.A.1. Summary

Past studies on IEC physics have focused primarily on the behavior of ion flow and fusion rates versus various operational parameters. Some of the first published work done on IEC devices was performed by Robert Hirsch [1]. Much of the recent experimental work on exploring the physics of gridded systems has been done at the University of Illinois by George Miley [2] and Y. Gu [3], and at the University of Wisconsin by Tim Thorson [4], John Weidner [5], Ben Cipiti [6], K.M. Subramanian [7], Alex Wehmeyer [8], Ross Radel [9], and Bob Ashley [10]. Additionally, recent contributions to theoretical modeling of gridded systems have come from Gil Emmert and John Santarius [11,12] at the University of Wisconsin, Masami Ohnishi [13] and Kunihiko Tomiyasu [14] at the Tokyo Institute of Technology, and Rick Nebel [15] at Los Alamos National Laboratory. A substantial contribution to the theory of gridless devices has come from Nebel [15] and Jaeyoung Park [16] on the Periodically Oscillating Plasma Sphere (POPS) concept, and from R. Bussard [17], M. Rosenberg [18], N. Krall [19], T. Rider [20], B. Nevins [21], Luis Chacon [22], and others, but these discussions focus largely on what happens when ions are confined for longer time scales than our gridded system can manage. This regime was not part of the present thesis, and therefore, the discussion in this section will focus on gridded experiments and theory.

Hirsch [1] performed a theoretical and experimental analysis of expected core behavior and showed indications that a dense core with multiple potential structures could form.

The experiments of Miley and Gu [2,3] focused on measuring the potential structure inside an IEC cathode by measuring the fusion rate as a function of radius from the center. Theoretical models developed at the University of Illinois predicted a double potential well would form as a result of flowing charge in the center of a spherical IEC device. A collimated proton detector system was developed to measure the radial proton release rate, and the data was mathematically unfolded to provide spatial resolution of the proton production rate inside the cathode radius. These experiments took place at neutral pressures ranging from 4 to 9 mtorr and at cathode voltages ranging from 15 to 30 kV. At lower values of cathode current, around 20 mA, the proton rate showed a peak at the center of the device, and fell off as radius from the center increased. From half-width half-maximum measurements, it appeared that ions were focusing into a tight core about 4.5 to 5 mm in radius. At higher cathode currents of 60 to 80 mA, the fusion rate was observed to peak at the device center, drop rapidly with increasing radius, and then peak again at r~5 mm before falling off in a straightforward fashion as the scan continued outward. Finally, a rough approximation of the well depth was calculated from the fusion data to be 22 to 27 % of the cathode voltage.

Early DD experiments done by Thorson [4] at the University of Wisconsin also focused on determining the potential structure inside an IEC device. He used Langmuir probes at lower cathode voltages in addition to fusion rate diagnostics. Thorson's measurements took place at lower pressures than those of Gu and Miley with the hope of achieving a simpler picture of the physics by minimizing ion-neutral interactions. The results of his probe measurements indicated that a single virtual anode was formed inside the cathode grid at the conditions of 0.013 Pa, 5 kV, and 40 mA. These measurements were repeated for different pressures and currents, and showed that the virtual anode tends to get more positive at higher cathode current and higher pressure, but none of the test conditions showed the existence of multiple well structures. Core size measurements were taken by using a CCD camera and filter system to look for H_{α} lines emitted by electron-recombination. The camera measurements showed core radius to increase with increasing grid wire separation, and actually showed core size decreasing with increasing pressure. Thorson also estimated the core density by using two theoretical models and two experimental methods (double probe, and pyrometric), all of which indicated an ion density of $1*10^{15}$ m^{-3} within a 50 % margin of error. Finally, measurements of the total D-D fusion rate were taken as a function of pressure, current, voltage, and cathode transparency. The pressure scan showed the expected linear dependence of fusion rate with background gas density, the current scan showed the expected linear dependence of beam-background fusion on beam current, the voltage scan showed fusion rate scaling similar to the fusion cross sections dependence, and the cathode transparency variation showed little effect at high transparencies, but a large effect when the grid was replaced by a solid target, where the fusion rate dropped significantly.

Emmert and Santarius at Wisconsin have developed a detailed simulation [11,12] that includes atomic processes of interest and follows ion flow as it makes multiple passes in an IEC device. Their calculations have shown that in the usual operating regime of the UW IEC device, the fusion rate in D-D is predicted to be dominated by charge exchange fusion reactions, a prediction consistent with the results of Thorson, and with Ashley and Cipiti, as will be described.

Ashley, Cipiti, and Subramanian [10,6,7] studied the different sources of fusion reactions in IEC devices in order to achieve a better method for producing medical isotopes. Their experiments consisted of using different size disks to block parts of the IEC core and cathode, thereby determining what fraction of reactions came from beam-background and beam-target (fuel ions hitting grid wires). Additionally, experiments that measured fusion rates in the core while simultaneously measuring off-axis rates were done. The results of these experiments detailed the number of reactions occurring in the volume of the IEC chamber. These data were used to determine the percentage of reactions due to fast ions striking background gas inside the cathode, charge-exchange neutrals hitting background gas in the chamber volume, and fast ions striking embedded targets in the cathode wires. They found that in a UW IEC device, operating at 0.27 Pa for D-D, 70% of all reactions occurred in the chamber volume (charge-exchange), 22% occurred inside the cathode grid (most likely beam-background), and 8% occurred within the grid wires over the range of 40-100 kV [6]. For D-^{3}He, however the results were quite different, indicating negligible charge exchange reactions, 5% beam-target reactions, and 95% embedded reactions over the same voltage range [6].

Experiments done by Weidner [5] and Cipiti [6] with medical isotope generation also showed that, while proof of principle experiments were possible with an IEC operating in “embedded mode”, it would be very difficult for such a device to compete with current technology as a result of the linear scaling of fusion output versus input power.

Recent work done by Wehmeyer [8] and Radel [9] studied the application of IEC devices for the purpose of detecting clandestine materials including explosives and highly-enriched uranium. These studies have indicated that the application of IEC technology for such a detection system could be realized in the near term.

R. Nebel [15] from Los Alamos National Laboratory, and M. Ohnishi [13] and K. Tomiyasu [14] from the Tokyo Institute of Technology modified the particle in cell code PDS-1 to effectively model IEC devices. Tomiyasu customized the code to simulate spherical grids and ion flow in the large cylindrical chamber at the UW. His simulations were done at ~ 2 mtorr and show the time evolution as well as steady state behavior of potentials, densities, and atomic and nuclear processes. The result of the PDS-1 simulation is a prediction of a very small potential well. The simulation also indicates a cold electron and ion buildup inside the cathode, as well as a uniform fast neutral flux traveling throughout the device. Additionally, Tomiyasu was able to predict the fraction of reactions occurring due to ion-neutral, fast neutral-neutral, and beam-beam sources in the IEC device. These results demonstrated good agreement with the results of Ashley and Cipiti in basic trend, but not in fusion rate magnitude, where it was off by an order of magnitude.

III.A.2. Discussion

The measurements of Gu and Thorson both show a potential structure that develops inside the cathode. The primary difference is that under special circumstances, Gu saw a multiple potential well structure, and Thorson did not. The significance of a multiple well structure would be to increase fusion rates in the wells due to a trapped ion density. A significant difference between the two experiments was the operating pressure, which affects the mean free path and therefore the frequency of energy loss processes affecting recirculating ions. Ion-neutral collisions would have been far more likely in the Illinois experiment, and the average ion energy may have been substantially degraded. In addition, there is a possibility that thermal ions would have been created inside the cathode grid in Gu's experiments, which would be far more likely to be trapped by an electron potential well, leading to the double well formation. Furthermore, some uncertainty regarding the resolution of the Illinois measurements could have helped contribute to this discrepancy. These uncertainties make it unclear if the observed potential structure observed should persist at lower pressures.

Another important finding is that measurements and calculations by nearly all IEC research groups show fusion rate scaling that is linear with current. In this mode, it will be difficult for IEC to compete with currently existing technologies in some near-term markets. Furthermore, a linear scaling of fusion rate with input power rules out any chance of generating electricity at Q > 1 levels. In order for IEC to be considered for some markets, it must be demonstrated that the fusion rate will scale proportional to I^2 or higher. Based on the results of Thorson [4], and the modeling done by Emmert and Santarius [11,12] and Tomiyasu [14], much lower operational pressures and higher ion currents must be reached if this scaling is ever to be observed.

Along with the above results, the experiments by Ashley, Cipiti, and Subramanian [10,6,7] on the source regions are significant to this dissertation. They showed that for D-^{3}He reactions, most of the observed reactions are expected to take place in the grid wires and only a small percentage occur from beam-target reactions. This result is very likely to have implications concerning the rate of ^{3}He-^{3}He fusion.

III.B. ^{3}He-^{3}He Reaction studies

While ^{3}He-^{3}He reactions had not been studied in an IEC device before, there have been several papers describing experiments performed by particle accelerators that have detected reactions between ^{3}He nuclei. Many of these studies have been motivated by differences in observations and predictions of solar neutrino output. Based on nuclear physics, and theories incorporating solar temperature, radius, and gravity, a prediction can be made of neutrino production from H-H burning. These calculations are nicely summarized in chapter 10 of the book *Cauldrons in the Cosmos* by Rolfs and Rodney [23]. The observed flux of electron neutrinos was too low and therefore the reaction rate of the p-p chain must have been lower than was required to give the sun its current size. To account for the extra heat required for the sun to maintain its size against gravity, a resonance in the ^3He-^3He reaction was suggested by Fetisov in 1972 [24]. Theoretical nuclear physics studies have been performed by Jarmie [25] and Descouvemont [26] to attempt to predict such a resonance, but neither of their analyses did so. Experimental studies of this reaction at relatively high energies have been done by Dwarkanath [27], Greife [28], Junker [29], and Krauss [30], and so far none of them have observed the predicted resonance either. It should be noted, however, that for energy levels in the solar energy regime (< 20 keV) the statistics in these experiments are sufficiently poor that the data is somewhat unreliable. Still, these works provide valuable cross section data and are valuable as a predictive tool for how to design the experiments reported on in this document. More recently, a massive collaboration headed by Ahmad [31] has shown good evidence that the correct number of neutrinos are coming out of the sun, but that they are changing flavor in flight, which causes many of them to be uncountable in older detector setups. The new detectors can count all three neutrino flavors, and the flux now agrees well with the predicted fusion rate in the sun with no ^3He-^3He resonance. Still, larger efforts are being devoted to building a more sensitive detector to confirm this result, and it seems sensible to study the ^3He-^3He nuclear reaction at the same time.

Another cosmic mystery involves the amount of ^3He that is observable in the universe. According to models of stellar evolution, the amount of ^3He that should be present is roughly 10 times the measured amount [32], and theories have been proposed [32,33] to explain how stars might burn more ^3He than expected. The study of fusion reactions involving ^3He at stellar energies could provide valuable insights into the mechanism that causes this additional burning.

III.C. References

[1] R. L. Hirsch, "Inertial-Electrostatic Confinement of Ionized Fusion Gasses," *Journal of Applied Physics*, **38**, [11], p.4522 (Oct. 1967).

[2] G. H. Miley, et al., "Discharge Characteristics of the Spherical Inertial Electrostatic Confinement (IEC) Device," *IEEE Tran. On Plasma Science* **25**, [4], August (1997).

[3] Y. Gu, "Experimental Study of Proton Rate Density in a Spherical Inertial Electrostatic Confinement Fusion Device," PhD thesis, University of Illinois (1998).

[4] T. A. Thorson, "Ion Flow and Fusion Reactivity Characterization of a Spherically Convergent Ion Focus," PhD thesis, University of Wisconsin—Madison (1994).

[5] J.W. Weidner, "The Production of ^{13}N from Inertial Electrostatic Confinement Fusion," Master's Thesis, University of Wisconsin-Madison (2003).

[6] B. B. Cipiti, "The Fusion of Advanced Fuels to Produce Medical Isotopes using Inertial Electrostatic Confinement," PhD thesis, University of Wisconsin—Madison, (2004).

[7] K. M. Subramanian, "Diagnostic Study of Advanced Fuel (D-D and D-3He) Fusion in an IEC Device," PhD thesis, University of Wisconsin—Madison (2004).

[8] A. L. Wehmeyer, "The Detection of Explosives Using an Inertial Electrostatic Confinement D-D Fusion Device," Masters thesis, University of Wisconsin (2005).

[9] R. F. Radel, et al, "Detection of HEU Using a Pulsed D-D Fusion Source," Proceedings 17th ANS Topical Meeting on Technology of Fusion Energy (TOFE) (to be published in Fusion Science and Technology 2006) .

[10] Robert P. Ashley, et al, "Recent Progress in Steady State Fusion Using D-^{3}He", *Fusion Science and Technology*, **44**, p. 564 (2003).

[11] G.A. Emmert and J.F. Santarius, "A Charge-Exchange Based Model for the Performance of Gridded, Spherical IEC Devices. Part I: single species atomic ions," University of Wisconsin-Madison (in preparation, 2006).

[12] G.A. Emmert and J.F. Santarius, "A Charge-Exchange Based Model for the Performance of Gridded, Spherical IEC Devices. Part II: molecular ions," University of Wisconsin-Madison (in preparation, 2006).

[13] M. Ohnishi, et al, “Multi-Potential Well Formation and Neutron Production in IEC Confinement Fusion by Numerical Simulations,” *Proceedings of the 16th IEEE/NPSS Symposium on Fusion Energy* (1995).

[14] K. Tomiyasu, “Numerical Simulation for UW-IEC Device,” Masters Thesis, Tokyo Institute of Technology, (2003).

[15] R. Nebel, “Experimental Observation of a Periodically Oscillating Plasma Sphere in a Gridded Inertial Electrostatic Confinement Device,” *Physical Review Letters*, **95**, p.015003-1 (1 Jul. 2005).

[16] J. Park, “Periodically Oscillating Plasma Sphere,” *Physics of Plasmas*, **12**, p.056315-1 (2005).

[17] Robert W. Bussard, “Some Physics Considerations of Magnetic Inertial-Electrostatic Confinement: A New Concept for Spherical Converging Flow Fusion”, *Fusion Technology*, **19**, pp. 273-293, (Mar. 1991).

[18] M. Rosenberg, Nicholas A. Krall, “The Effect of Collisions in Maintaining a non-Maxwellian Plasma Distribution in a Spherically Convergent Ion Focus”, *Physics of Fluids B*, **4**, [7], pp. 1788-1794 (July 1992).

[19] Nicholas A. Krall, et al, “Forming and Maintaining a Potential Well in a Quasispherical Magnetic Trap,” *Physics of Plasmas*, **2**, [1], pp. 146-158 (Jan. 1995).

[20] Todd H. Rider, “A General Critique of Inertial-Electrostatic Confinement Fusion Systems,” *Physics of Plasmas*, **2**, [6], pp. 1853-1872 (Jun. 1995).

[21] W. M. Nevins, “A Review of Confinement Requirements for Advanced Fuels,” *Journal of Fusion Energy*, **17**, 1, pp. 25-32 (1998).

[22] L. Chacon, et al, “Energy Gain Calculations in Penning Fusion Systems Using a Bounce-Averaged Fokker-Planck Model,” *Physics of Plasmas*, **7**, [11], pp. 4547-4560 (Nov. 2000).

[23] C. E. Rolfs, W. S. Rodney, “Cauldrons in the Cosmos,” The University of Chicago Press (1988).

[24] V. N. Fetisov, Y. S. Kopysov, “Are the Solar-Neutrino Experiments Suggestive of a Resonance in the ^{3}He + ^{3}He System?,” *Physics Letters*, **40B**, [6], p.602 (Aug. 1972).

[25] N. Jarmie, *Nuc. Sci. Eng*. **78**, p.78 (1981).

[26] P. Descouvemont, "Microscopic Analysis of the $^{3}He(^{3}He,2p)^{4}He$ and $^{3}H(^{3}H,2n)^{4}He$ Reactions in a Three Cluster Model," *Physical Review C*, **50**, [5], p.2635 (Nov. 1994).

[27] M. R. Dwarakanath,"$^{3}He(^{3}He,2p)^{4}He$ and the Termination of the Proton-Proton Chain," *Physical Review C*, **9**, [2], p.805 (Mar. 1974).

[28] U. Greife, et al, "Laboratory for Underground Nuclear Astrophysics (LUNA)," *Nuclear Instruments and Methods in Physics Research A*, **350**, p.327 (1994).

[29] M. Junker, et al, "Cross Section of $^{3}He(^{3}He,2p)^{4}He$ Measured at Solar Energies," *Physical Review C*, **57**, [5], p.2700 (May 1998).

[30] A. Krauss, et al, "Astrophysical S(E) Factor of $^{3}He(^{3}He,2p)^{4}He$ at Solar Energies," *Nuclear Physics A*, **467**, p.273 (1987).

[31] Q. R. Ahmad, et al, "Direct Evidence for Neutrino Flavor Transformation from Neutral-Current Interactions in the Sudbury Neutrino Observatory," *Physical Review Letters*, **89**, [1], (July 2002).

[32] P. Eggleton, "Deep Mixing of ^{3}He: Reconciling Big Bang and Stellar Nucleosynthesis," *Science Express*, (Oct. 26th 2006).

[33] D. Dearborn, "Three Dimensional Numerical Experimentation on the Core Helium Flash of Low-Mass Red Giants," *Astrophysical Journal*, **639**, [1], p.405 (2006).

IV. IEC Theory

IV.A. Basic IEC Theory

Most IEC fusion devices today are of the type first built and studied by Philo. T. Farnsworth and one of his collaborators, Robert L. Hirsch [1]. Their system consisted of six ion sources in close proximity to a spherical cathode that could be biased negatively with respect to the sources. Since then, most IEC experiments have operated in an even simpler configuration, consisting of either two concentric spherical or coaxial cylindrical grids. A large negative potential difference is created between the grids causing a radially inward electric field, which accelerates positively charged ions inward. In the most basic model these ions oscillate through the core until they collide and fuse, or are lost to a collision with the grid. Since the ions are directed almost purely radially, they converge to a small volume as they pass through the cathode, creating a high ion density, as depicted in figure IV-1:

Figure IV-1: Basic IEC Model

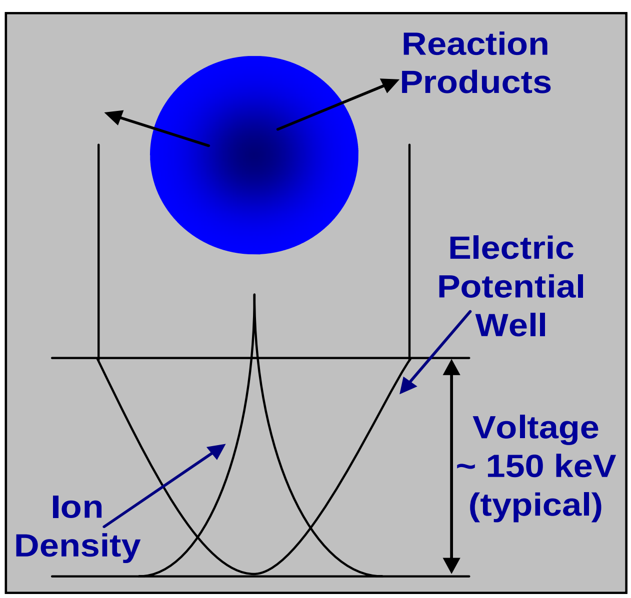

While the Farnsworth system used a series of ion sources to generate plasma, most current research devices rely on Paschen breakdown or filament assisted discharges to operate. A schematic of the large IEC system at UW-Madison is shown in figure IV-2:

Figure IV-2: Large UW-IEC Device

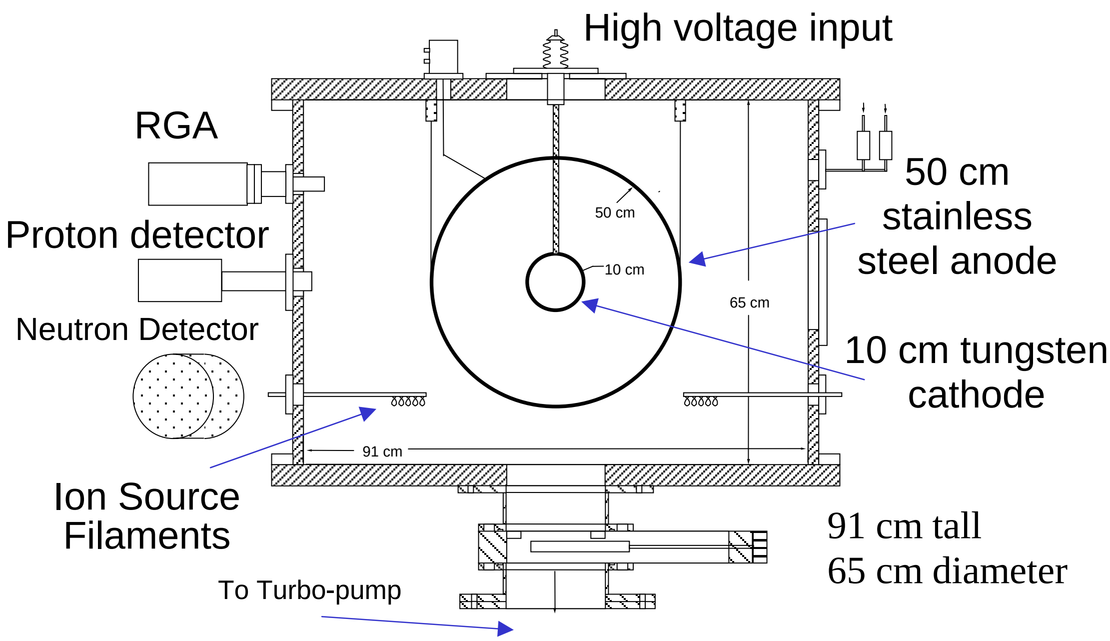

In this system, gas is flowed into the main vessel, then ionized by Paschen breakdown (P>5mtorr) or electrons from hot filaments (P>0.2mtorr). The positively ionized fuel then gets pulled toward the cathode grid and starts to oscillate between the anode and the center of the device until it either fuses, scatters out of the system, or collides with the cathode grid. The diagnostics on the left side include neutron and proton detectors for detecting at fusion reactions and a residual gas analyzer (RGA) for diagnosing impurity concentrations.

The use of this type of machine to produce fusion reactions with advanced fuels is straightforward. The very high ion energies required can be obtained by applying a high voltage to the cathode grid. In the absence of atomic and space charge phenomenon, the kinetic energy of any ion inside the cathode grid will be:

$$E_{ion} = \left| q_{ion} * V_{cath} \right| \tag{IV-1}$$

Where q is the charge on the ion, and V_{cath} is the potential difference between the cathode and the anode. In this very simple model, it is possible to get ion energies of over 100 keV with power supplies capable of 100 kV or more. This is very difficult for most fusion systems, especially for Maxwellian plasma systems and so IEC devices are better suited for studying 2nd and 3rd generation fuels. However, such a simple model is not entirely realistic and many complications exist. Interactions with background gas particles cause ion attenuation and energy loss, as well as fusion reactions in locations other than the core.

IV.B. IEC Source Regions

In reality, fusion in IEC devices is known to occur in a few different locations, from atoms in different physical states. These include the interaction of fast re-circulating ions with neutral fuel in the space inside the anode, the interaction of fast neutral particles (generated by charge exchange reactions) with neutral fuel everywhere in the device, and the interaction of fast re-circulating ions with each other inside of the cathode. Interactions between fast neutrals and fast ions are neglected since the fusion rates are proportional to the density of both species, and nowhere in the device are these both expected to be large.

The first type of interactions can be separated into two categories; those between fast ions and neutral gas which will from now on be referred to as **beam-background** interactions, and those between fast ions and fuel ions that have become embedded in the cathode wires, which will from now on be referred to as **beam-embedded** interactions. The second type of interactions can also be subdivided into two categories; those between fast neutral particles and neutral gas hereafter referred to as **fast neutral-background** reactions, and those between fast neutral particles and fuel ions that have become embedded in any solids in the device, hereafter referred to as **fast neutral-embedded** reactions. The third type of reactions, which has the possibility for high density only in the core of the device, will from now on be called **converged-core** reactions. A description of each reaction type in more detail is listed below.

IV.B.1 Beam-background reactions

These reactions occur between ions trapped in the IEC potential well and a neutral atom or molecule of fuel gas. Such interactions can occur anywhere inside the anode, however the probability for fusion $\sigma(E)$ goes up rapidly as the ion energy increases, which means that an ion is much more likely to undergo fusion near the cathode grid since it is at its highest possible energy there. A plot of the ^{3}He-^{3}He cross section is shown in figure IV-3 [2]:

Figure IV-3: ^3He-^3He Projectile-Target Fusion Cross Section versus Energy

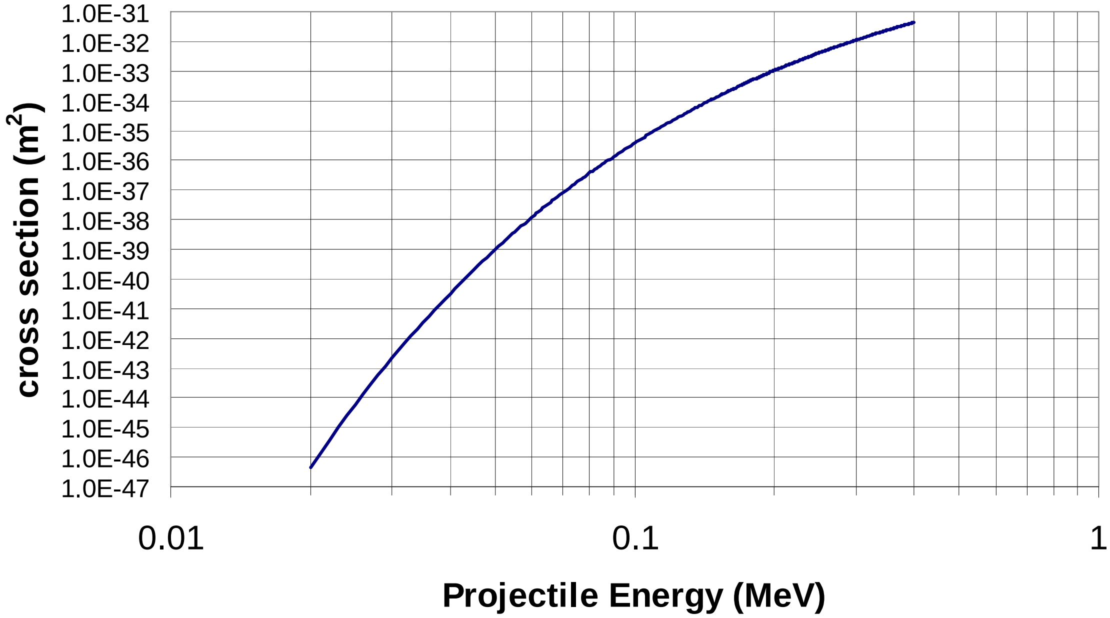

If an IEC is capable of operating at sufficiently low pressure so that atomic processes do not degrade the ion energy, equation Eq. IV-1 accurately will describe the energy of ions near to and within the cathode. In this case, the specific reaction rate R_s (reactions/m^3) for beam-background reactions can be expressed as:

$$R_s = n_b n_i \sigma(E)\sqrt{\frac{2E}{m_i}} \tag{IV-2}$$

Where E is the ion energy, n_b is the background gas density, $n_i(E)$ is the energy dependent ion stream density, $\sigma(E)$ is the fusion cross section between a cold background particle and ion of energy E, m_i is the ion mass, and all units are SI. For the case of an ion beam traveling through an IEC this result can further be simplified to give the total fusion rate in terms of ion current

$$R = n_b I \sigma(E) l \tag{IV-3}$$

Where l is the interaction path length in meters, which in this case will be the path length over which the detection system observes the beam. This result gives the expected fusion rate from beam-background reactions and will be compared to the other source regions later.

IV.B.2 Beam-embedded reactions

When an IEC device is operated for an extended period of time, the cathode grid and other solid structures in the device become loaded with some amount of the fuel atoms. This is due to ions and neutrals that have sufficient energy to penetrate the surface of these structures and then remain trapped within. Densities of such trapped ions can become quite high, and fast particles which eventually collide with these structures can generate fusion reactions. Experimental evidence thus far has indicated embedded helium densities as high as 3.5×10^{21} particles / cm^3 [3] and recent SEM measurements indicate densities of up to 2.5×10^{22} particles / cm^3 in W samples [4]. From a known target density in the cathode, an expected fusion rate can be calculated due to fast ions colliding with this structure. Since the embedded density may be on the order of the metal density, the stopping power of the grid may be higher or lower than the pure metal depending on whether the implanted ions are interstitially located or cause displacement of the grid atoms. Since this is not well known, the characteristics of the pure metal will be used to approximate the ion energy as it travels through the grid wires. This ion energy, as a function of depth with the embedded density can be used to get a fusion rate as a function of depth, and integrated to produce a total fusion rate from embedded reactions. If the stopping power of tungsten (a typical cathode material) is used, the ion energy as a function of path length into the material is described in figure IV-4 for ^{3}He ions:

Figure IV-4: He^{+} Ion Energy versus Path Length in Pure Tungsten (E_o = 200keV)

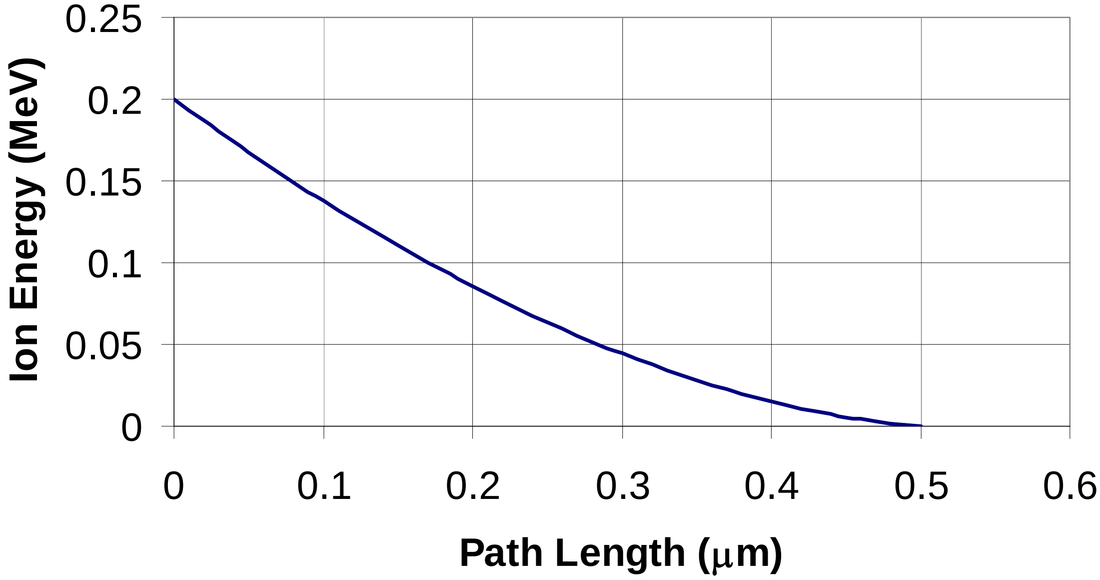

(data from NIST ASTAR database for alpha particles and converted from ^{4}He to ^{3}He using the Bethe-Block formula[5])

A program called TRIM [6] can also be used to model the range of ions in matter, and a simulation with 200 keV He^{+} impacting tungsten shows that some ions actually don't make it as far as the smooth slowing down approximation indicates due to large angle scattering along the path. This means the approximation used above will give an upper limit to the reactivity, since some ions lose energy faster than indicated. The result of the TRIM simulation showing the random walk of ions is shown in figure IV-5:

Figure IV-5: Helium Particle Trajectories in Tungsten (500 histories, E_o=200 keV)

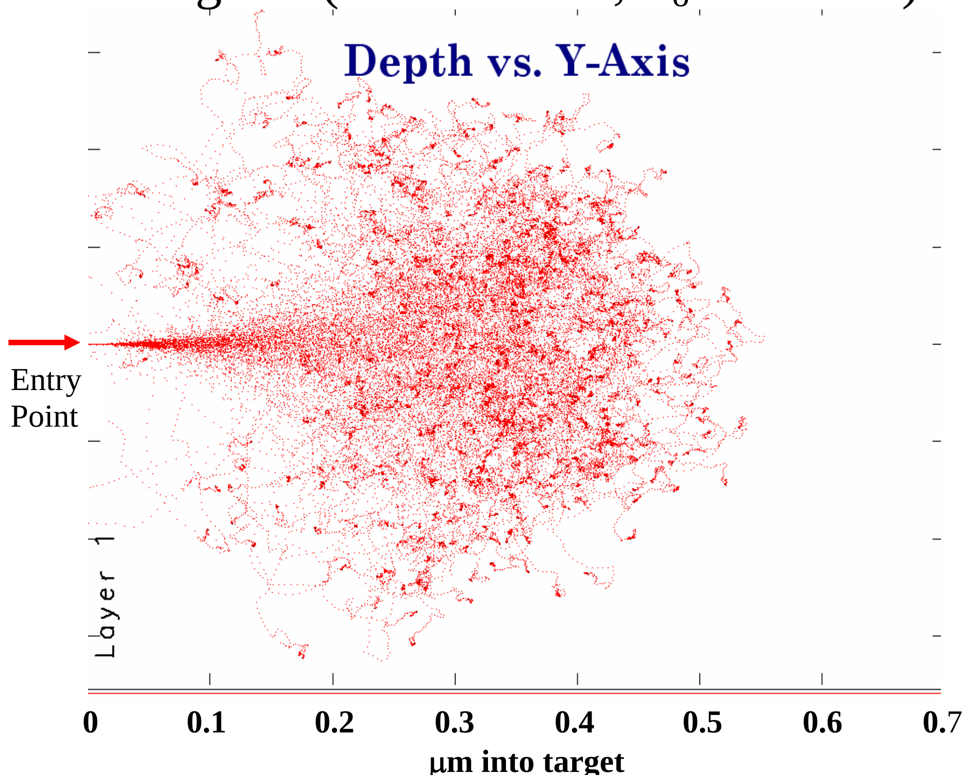

With the ion energy as a function of path length into the tungsten, the embedded density, the cross section and the ion density, a fusion rate, F within the grid wires can be calculated:

$$F = \int_0^{\ell_{final}} I n_{emb} \sigma(\ell) d\ell \tag{IV-4}$$

Where l_{final} is the path length of an ion colliding with the grid, n_{emb} is the embedded number density of fusion fuel in the grid wires, and $\sigma(l)$ is the fusion cross section as a function of depth.

The contribution of fusion due to fast neutral atoms fusing with fuel atoms embedded in IEC structures other than the cathode can be neglected since the proton detection system does not observe any other structures that are expected to have a high embedded density.

IV.B.3 Fast neutral-background reactions

Fast neutral particles are generated from ions that have gained some energy, and then lost their charge, typically through a charge-exchange process. This process results in a neutral particle that has some energy but is no longer confined in the electrostatic well, and a new ion with no significant energy. The fast neutrals will continue in a straight line until they collide with another particle, normally those atoms comprising the vacuum vessel wall. The probability of a charge-exchange collision occurring is related to the energy of the ion and the density of neutral targets. Therefore, an estimation of the ion speed as it travels through the IEC device is necessary to approximate the number of fast neutrals. To first order, the vacuum fields in a spherical IEC can be calculated using Gauss' law and the appropriate boundary conditions:

$$\oint E \cdot dA = \frac{1}{\varepsilon_o} \int \rho dV \qquad \text{(IV-5)}$$

where E is the electric field on the surface of interest (in this case the surface is spherical and the field is constant at constant radius), dA is the differential area of the surface, ε_o is the permittivity of free space, ρ is the charge density, and dV is the differential volume that the charge density exists within.

For the case of two concentric spheres, if only the region between them is considered, the solution to this equation is:

$$E(r) = \frac{Q}{4\pi r^2 \varepsilon_o} + C \qquad \text{(IV-6)}$$

Where Q is the total charge on the cathode, r is the radial distance from the center of the device but is confined to the region between the cathode and anode, and C is a constant of integration that will be set by the boundary conditions.

At the anode wall, the electric field in the device must equal zero, and this sets the value of the constant C:

$$C = -\frac{Q}{4\pi r_a^{\ 2} \varepsilon_o} \qquad \text{(IV-7)}$$

Where r_a is the anode radius.

The electric potential ϕ is related to the field by the relationship:

$$E(r) = \frac{Q}{4\pi \varepsilon_o}\left(\frac{1}{r^2} - \frac{1}{r_a^{\ 2}}\right) = -\nabla\phi \qquad \text{(IV-8)}$$

Since our case is symmetric in angle, only the radial part of the gradient is non-zero, and therefore, the potential can be written as:

$$\phi(r) = -\frac{Q}{4\pi\varepsilon_o}\left(\frac{r}{r_a^{\,2}} + \frac{1}{r}\right) + C \tag{IV-9}$$

The values for C and Q are determined by applying the boundary conditions in potential, $\phi=0$ at $r=r_a$, and $\phi=\phi_o$ at $r=r_c$, where ϕ_o is the applied voltage on the cathode, and r_c is the cathode radius. The vacuum potential in an IEC device can then be written as:

$$\phi(r) = -\frac{Q}{4\pi\varepsilon_o}\left(\frac{r}{r_a^{\,2}} + \frac{1}{r} - \frac{2}{r_a}\right) \tag{IV-10}$$

Where Q from the cathode boundary condition is:

$$Q = -\frac{4\pi\varepsilon_o\phi_o}{\left(\frac{r_c}{r_a^{\,2}} + \frac{1}{r_c} - \frac{2}{r_a}\right)} \tag{IV-11}$$

The theoretical vacuum field for the IEC configuration used in this thesis is plotted below for r_a = 0.305m, and r_c=0.05m:

Figure IV-6: IEC Vacuum Potential Versus Radial Position for Spherical Geometry

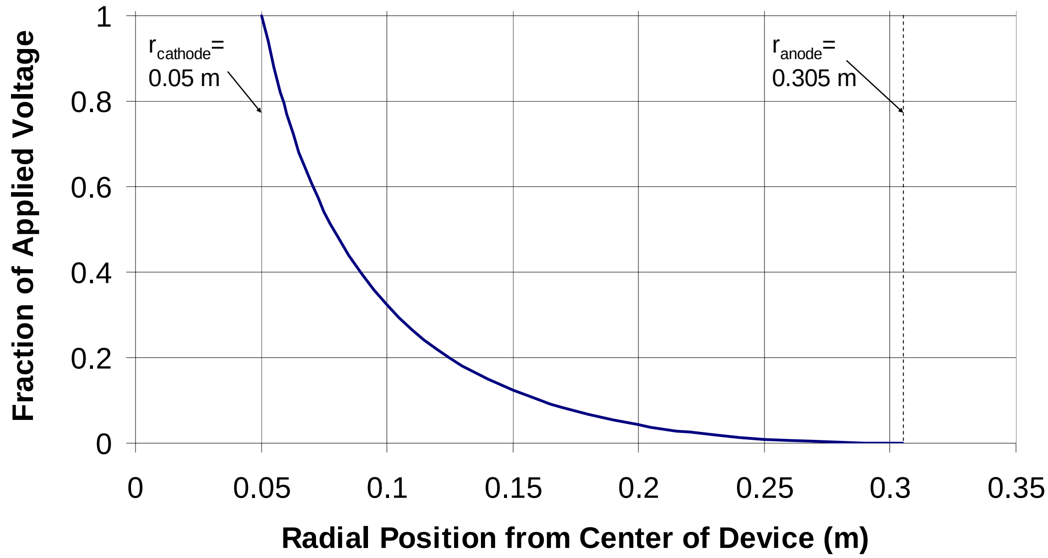

Since the vacuum field does not include the presence of space-charge, the effects of such charge on the potential should be considered. For the range of operation considered in these experiments, space charge is not expected to have a large effect since the ion current present in the device is far below the space-charge current limit. Nonetheless, the effects of this charge will be considered in a simple model. This model will use the vacuum field and total ion current to calculate the spatial ion distribution neglecting space charge to establish an initial condition, and then the ion charges will be added to the field profile. The profile will be adjusted, and the iteration will repeat until a convergent solution is reached. This model considers only non-collisional ions and does not include the effects of electrons, but should be useful in obtaining an approximate solution. Electrons may be neglected since the electron density from the source region scales as:

$$n_e(r) = n_{eo} e^{-\frac{e\phi(r)}{T_e}} \tag{IV-12}$$

Where $n_e(r)$ is the electron density as a function of radius, n_{eo} is the electron density in the source, $\phi(r)$ is the potential as a function of radius, and T_e is the electron temperature. Since T_e in the source region is only expected to be a few eV, the exponential term becomes small very quickly beyond the anode meaning very few source electrons will penetrate. Furthermore, electrons generated from ionization and secondary emission in the high field region have a very short residence time due to their small mass and subsequent high velocity, and therefore their density is much smaller than that of the slower moving ions in that space.

With these assumptions, the ion density as a function of radius for $r>r_{cath}$ can be expressed as:

$$n_i(r) = \frac{I}{4\pi r^2 v_i(r)} = \frac{I}{4\pi r^2}\sqrt{\frac{m_i}{2\phi(r)q_i}} \tag{IV-13}$$

Where n_i is the ion density in coulombs/m^2, $v_i(r)$ is the ion velocity as a function of r, I is the total ion current, m_i is the ion mass and q_i is the ion charge.

For typical IEC operation, I ~ 100 mA and the ions are singly charged ^{3}He. The iterative solving process described above converges to within less than 1% in three iterations, and the voltage difference is plotted in figure IV-7 for a cathode voltage of 200 kV:

Figure IV-7: Voltage Difference Between Vacuum and Plasma Fields ($V_{cathode}$ = 200 kV)

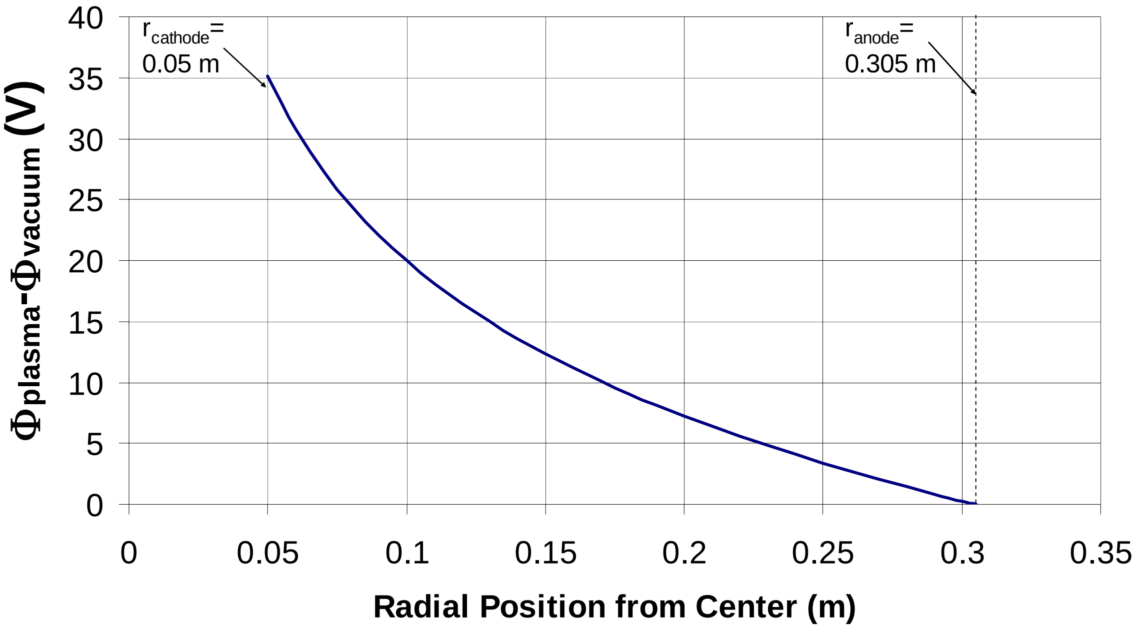

This shows there is no significant difference between the vacuum fields and the plasma fields, and therefore the effects of ion space charge do not need to be considered when describing the voltage profile of an IEC device under these conditions.

With information on ion density and ion energy, the probability that an ion will charge exchange before impacting the cathode grid can be found. The mean free path is a good interpretation of this and can be expressed as follows:

$$\lambda(V_o) = \frac{\int dr}{n_b \int \sigma_{cx}(r) dr} \qquad \text{(IV-14)}$$

Where n_b is the density of the background gas, and $\sigma_{cx}(r)$ is the charge exchange cross section as a function of radius. Typically, σ_{cx} is given in terms of energy, but the energy of an uncollided ion in an IEC is proportional to radius as shown above, and therefore σ_{cx} can be be expressed as a function of radius from the device center. A plot of the charge-exchange cross-section [7] versus ion radial position is shown below for an applied cathode voltage of -200 kV and a background gas pressure of 0.2mtorr:

Figure IV-8: Charge Exchange Cross Section versus Ion Position (P = 0.2 mtorr, V_{cath} = 200kV)

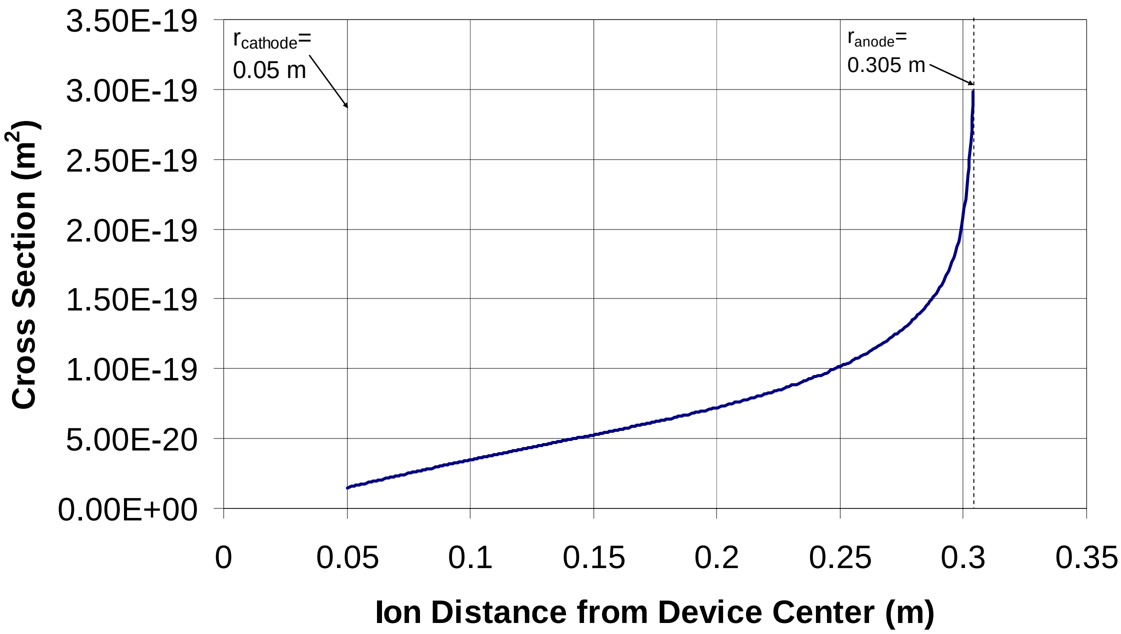

This information can be used to solve the integral above, and the effective mean free path for a He^+ ion at these conditions is around 2.5 meters or about 4 passes through the device. Clearly if the number of passes is around 10 (determined from the grid transparency) an average ion will charge exchange in its lifetime. The mean free path, however is highly dependent on energy and the probability of a charge-exchange event is only high when the ion is moving slowly. As a result, neutrals formed from charge exchange have relatively low energy, and ions formed will still be able to obtain most of the cathode voltage. To get a good feel for this it is useful to consider the probability of an ion undergoing charge exchange at a given energy. The probability of an ion undergoing charge exchange in a thin shell can be written as:

$$P = 1 - e^{-\frac{1}{mfp}\Delta r} \qquad \text{(IV-15)}$$

Where mfp is the mean free path and Δr is the shell thickness. If an ion were allowed to re-circulate until it neutralized through charge-exchange, the probability that the event would occur at a given energy is plotted below:

Figure IV-9: Probability of Charge Exchange at a Given Ion Energy for Infinite Transparency (He^{+1})

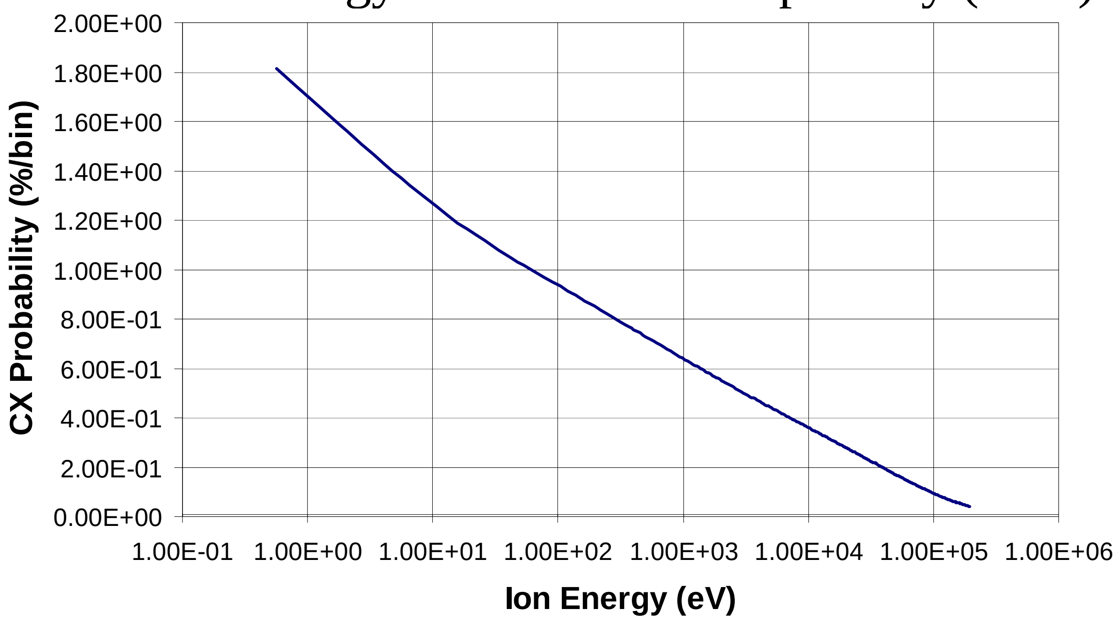

This shows that as the ion energy gets above a few kV, the chance for charge exchange is much lower. Since the ^3He-^3He cross section at voltages likely for charge exchange are so low, the rate of fusion from slow charge-exchange neutrals can be neglected compared to the fusion rate from beam-background fusion.

IV.B.4 Converged Core Reactions

The most desirable reactions in an IEC system are converged core reactions. These occur between two fast ions, which results in higher center of mass collision energy and there is no need for background gas particles that can cause energy loss. Since re-circulating ions in this case are colliding with each other, the fusion rate is expected to be proportional to the ion current squared, which is desirable since fusion gain increases with current. So far however, no one has observed this reactivity scaling with current, and therefore little or no experimental experience with converged core reactions is available. Models have been constructed by many to attempt to predict what would happen, but most of these models assume ideal experimental conditions (such as purely radial acceleration and impossibly high grid transparencies) which do not exist in the laboratory. Therefore, no particular model is able to accurately predict the fusion rate, and therefore no prediction will be made here. Care was taken experimentally, however to observe the scaling of the fusion rate compared to the ion current. Since no I^2 trend was seen, it is assumed these reactions did not play a significant role in our observations.

IV.C. Source Regions-Analysis

It is necessary to compare the fusion rates expected from the different source types in order to have an accurate measurement of the fusion cross sections. Based on the discussion above of the different source regions, it is expected only to have a considerable contribution of fusion reactions from beam-background and beam-embedded reactions. This analysis is consistent with earlier analysis of IEC systems using D-^{3}He [3] and is expected to be even more dramatic with the higher energy cross section of ^{3}He-^{3}He. The reactivity due to beam-background reactions can be written as:

$$R_{bb} = n_b I \sigma(E) l \qquad \text{(IV-16)}$$

For the intended operating conditions of 0.027 Pa, 200 kV, I=100 mA, and an observed interaction length of 20 cm, the beam background fusion rate would be ~ 850 reactions/second [8].

If the cathode grid is also in the field of view of the detector, then the reactivity in the cathode wires is given by:

$$R_{emb} = \int_0^{r_{final}} I n_{emb} \sigma(r) dr \qquad \text{(IV-17)}$$

This reaction rate is based on the amount of ion current striking the cathode, which is more like 10mA. Solving this integral, with the empirically measured value for n_{emb} by Cipiti of 3.5 * 10^{21} particles / cm^3 gives a fusion rate of 1.2 * 10^4 reactions/sec [9] in the grid, of which only half will be observable since the other half of the detectable protons will head deeper into the grid wires. Recent SEM measurements indicating a density of 2.5 * 10^{22} particles / cm^3 by Radel [4] would result in a fusion rate of 7 * 10^4 reactions / sec if the W metal maintained a pure structure and higher if He implantation was displacing W atoms. Either way, these calculations indicate that a majority of observed reactions could come from embedded fusion in the grid wires. Therefore it would be important to keep the cathode grid out of the field of view of the detector to minimize the component of any beam-embedded fusion reactions if accurate cross section measurements were to be made.

IV.D. References

[1] Philo T. Farnsworth, "Electric Discharge Device for Producing Interactions Between Nuclei," United States Patent Office #3,258,402, June 28, 1966.

[2] A. Krauss, "Astrophysical S(E) Factor of $^{3}He(^{3}He,2p)^{4}He$ at Solar Energies," *Nuclear Physics A*, **467**, p.273 (1987).

[3] B. B. Cipiti, "The Fusion of Advanced Fuels to Produce Medical Isotopes using Inertial Electrostatic Confinement," PhD thesis, University of Wisconsin—Madison, (2004).

[4] R. F. Radel, University of Wisconsin—Madison, Private Communication (2006).

[5] G. F. Knoll, "Radiation Detection and Measurement," 3rd Edition, John Wiley and Sons Inc. (2000) .

[6] J. F. Ziegler and J. P. Biersack, "SRIM The Stopping and Range of Ions in Matter," Vers. SRIM-2003.26, From SRIM.com (2003).

[7] R. K. Janev, ALADDIN Database, IAEA-AMDIS (2006).

[8] See appendix A for beam-background calculation.

[9] See appendix A for beam-embedded calculation.

V. Ion Source Theory

V.A. Neutral and Ion Flow from an Aperture

As established in chapters II and IV, the need to operate an IEC device at low pressure necessitates an external ion source. To choose the type of source, a determination of what plasma density and neutral gas pressure are required had to be made. For most of the experiments of interest to this thesis, the background gas pressure desired in the reaction chamber was ~ 200 μtorr. To benchmark operational characteristics of these experiments against experiments with other gasses, the ion current should be similar to that from past runs as well, which means ion currents on the order of ~10 mA were desired. These two parameters are all that is necessary to determine what source capabilities are necessary.

Almost all ion sources require a higher operational pressure than that which is desired for IEC operation. For this reason, a low conductance aperture is required to separate the source from the IEC device. The conductance equation for such an aperture can be used along with the desired pressure differential in order to determine the approximate size for the hole, but first the flow regime must be determined. The Knudsen number, K is useful for making this determination and is expressed as:

$$K = \frac{\lambda}{d} \qquad \text{(V-1)}$$

Where λ is the mean free path of the gas molecules and d is the dimension of the chamber. If K << 1, then the flow is viscous, and if K > 1 the flow is molecular. When 0.01 < K < 1, the flow is in an intermediate stage known as the transition or Knudsen state. For an ion source suitable for feeding the IEC device, λ will be around 2 cm (corresponding to roughly 5 mtorr) and the diameter of the source will be on the order of 5 cm, which gives K ~ 0.4. This puts the flow in the transition region, and since the pressure on the high side of the aperture is considerably more than twice the low side, this qualifies as choked flow. The conductance C in m^3/s for choked flow according to O'Hanlon [1] can be written as:

$$C \approx 0.85A\left(\frac{kT}{m}\frac{2\gamma}{\gamma+1}\right)^{\frac{1}{2}}\left(\frac{2}{\gamma+1}\right)^{\frac{\gamma}{\gamma-1}} \tag{V-2}$$

Where A is the hole area in m^2 and γ is the specific heat ratio which for monatomic gasses is 5/3. Assuming the temperature of the neutral gas, T is roughly room temperature, solving for C as a function of A gives:

$$C = 363A\,(\mathrm{m}^3/\mathrm{s}) \tag{V-3}$$

To get from conductance to flow rate, one simply multiplies the conductance by the pressure differential across the aperture. To determine the pressure in the IEC chamber, one must set the flow into the system equal to the flow out of the system. The flow out of the chamber is simply equal to the turbopump speed, in this case it is 0.6 m^3/s for He, times the pressure over the pump. Equating these two terms gives:

$$C * P_{source} = 0.6P_{IEC} \tag{V-4}$$

Where P_{source} is the pressure in the ion source and P_{IEC} is the pressure in the IEC device. This allows for the hole size to be determined in terms of the desired pressure ratio:

$$A = \frac{0.6}{363} \frac{P_{IEC}}{P_{source}} \tag{V-5}$$

If the source pressure is around 5 mtorr, and the desired IEC pressure is 0.2 mtorr, a hole with an area of ~ 0.6 cm^2 would be required.

With the aperture size being set to control the neutral pressure, the necessary plasma density in the source can be calculated to provide the desired beam current. The maximum ion current that can be extracted through a small hole is limited to the Bohm current. This current limit is expressed in equation V-6:

$$I_b = 0.61 nqA \left(\frac{kT_e}{m_i} \right)^{\frac{1}{2}} \tag{V-6}$$

Where n is the plasma density, q is the ion charge, A is the aperture area, T_e is the electron temperature, and m_i is the ion mass. If as specified above, the desired current is 10 mA, and the hole size is 0.6 cm^2, and an electron temperature of 1 eV is assumed, then the required plasma density is ~ $4*10^{17}/m^3$.

There are several source types that theoretically can provide for this combination of pressure and density including hollow cathodes, inductive sources and helicon sources

[2]. The first two, however would certainly be operating near their limit and since He gas is notoriously difficult to ionize, it is possible they would be unable to meet the task. Furthermore, it would be nice if it were possible to go to higher currents and lower pressures if desired, and it is this consideration that makes the choice of a helicon source stand out above the others.

V.B. Helicon Sources

First discovered by Boswell [3], helicon sources bear a slight resemblance to inductive sources in the way that the antenna is coupled to the plasma. However, unlike inductive sources, helicon sources can develop very high densities with very high efficiency. In fact, it has been experimentally demonstrated for many years now that launching helicon waves into a plasma source can generate very high plasma densities (10^{19} – 10^{20} m^{-3}), with relatively low RF power (~100W) and magnetic field (~500G) [4,5,6,7]. Unfortunately, there is no current theory which accurately describes the ionization efficiency that helicon waves cause in plasma sources, and there is much speculation over which waves actually cause this ionization to happen. A good summary of some of the current theories about plasma excitation by helicon waves has been written by Chen [8], and his paper also includes a guide for designing helicon sources. One of the most critical components for these designs is the RF antenna. Many different geometries have been proposed and tested that can successfully launch different wave modes. The exact shape and length of the antenna is determined by what type of wave one wishes to excite, the desired plasma density, and the gas species. A few examples, created by Ben Longmier [9] of the University of Wisconsin are shown in Figure V-1:

Figure V-1: Examples of Possible Helicon Antenna Designs

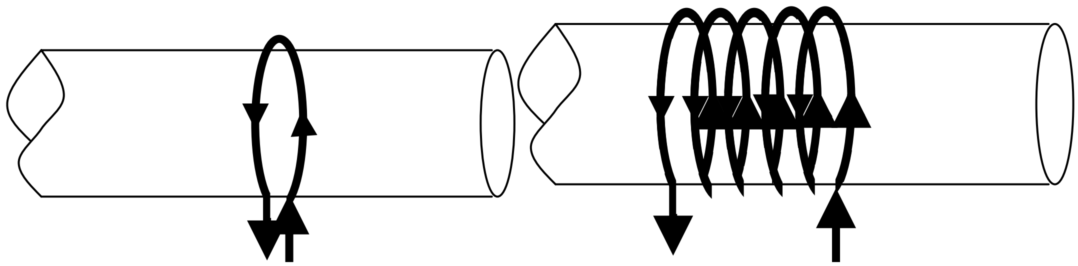

a) m=0 antennas—single loop (left) and helical (right)

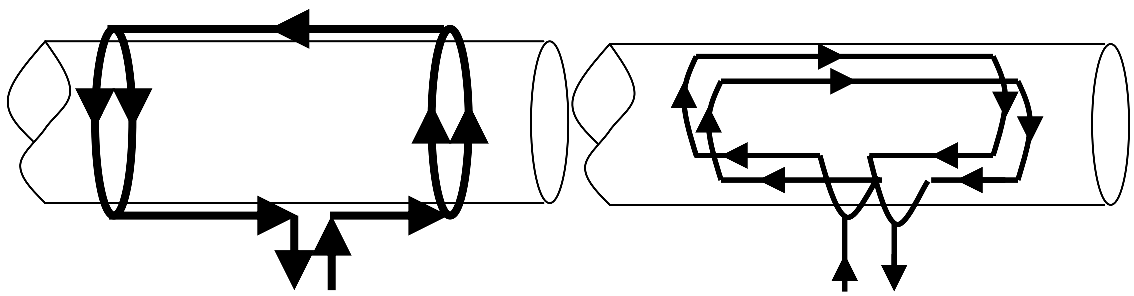

b) m=±1 antennas—Nagoya III (left) and Double Saddle (right)

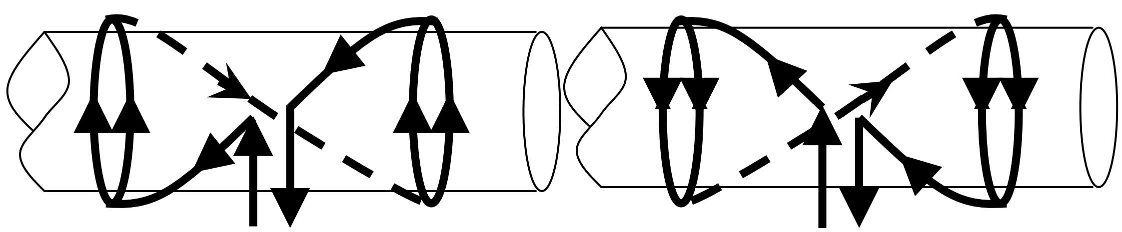

c) m=-1 (left) and m=+1 (right) antennas

So far, most papers indicate that antennas which launch the m=+1 modes are the most efficient, but for the purposes of these experiments, a well tested design, the Nagoya III type antenna shown in V-1b was chosen for its ease of construction, versatility, and good documentation.

V.C. Extraction Geometry

In order to provide for a well collimated beam, special attention must be given to the shape of the extraction electrode which the beam passes through. If collimation is important, an injector section is required in order to quickly accelerate the beam before space charge pushes it apart. For the experiments presented herein, it is not particularly important, but basic care was taken to collimate the beam nonetheless. Since the beam's internal forces push outward, it is desirable to generate an external electrostatic force that pushes inward. This is effectively done by shaping the anode (in this case the exit aperture) in such a way as to create electric field lines that would be "uphill" for ions and therefore there would be an opposition to spreading. The details of how to design these electrodes is very well documented in Chapter 7 of the book "Charged Particle Beams" by Stanley Humphries, Jr. [10] For the low to medium perveance ($I/V^{3/2}$) source used in these experiments, the approximation that the source resembles a Pierce gun was made and an angle of 67.5^{o} was chosen for the anode wall. This is not by any means a perfectly collimated source, but as stated previously, perfect collimation is not necessary for these experiments.

V.D. References

[1] J. F. O'Hanlon, "A User's Guide to Vacuum Technology," 3rd Edition, John Wiley and Sons Inc., (2003).

[2] H. Conrads, M. Schmidt, "Plasma Generation and Plasma Sources," *Plasma Sources, Science, and Technology*, **9**, p.441 (2000).

[3] R. W. Boswell, "Plasma Production Using a Standing Helicon Wave," *Phys. Lett. A*, **33**, p.457 (1970).

[4] I.S. Hong, "Ion Beam Characteristics of Novel Helicon Ion Sources for Different Plasma Parameters," *Review of Scientific Instruments*, **71** [3], (2000).

[5] Y.S. Hwang, "Conceptual Design of a Helicon Ion Source for High-Current DC Accelerators," *Review of Scientific Instruments* **69** [3] p.1344 (1998).

[6] G.S. Eom, "Helicon Plasma Generation at Very High Radio Frequency," *Plasma Sources Science and Technology*, **10**, p.417 (2001).

[7] R. Soulsby, "Design and Construction of a Compact Helicon Source," APS DPP99 Poster session, (1999).

[8] F. F. Chen, "Plasma Ionization by Helicon Waves," *Plasma Physics and Controlled Fusion*, **33**, [4], p.339 (1991).

[9] B. W. Longmier, University of Wisconsin—Madison, private communication (2006).

[10] S. Humphries Jr., "Charged Particle Beams," John Wiley and Sons Inc. (1990).

VI. Experimental Setup and Technique

Many different pieces of hardware were developed in order to accomplish the experiments described in this work. Chapter II described the need for all of this hardware, and this chapter will discuss each of them in detail.

VI.A. Vacuum Environment

To meet the needs described in chapter II, four components were designed for the vacuum environment. These components are (1) the main vacuum system which consists of a chamber and pumping system, (2) the water cooling system, (3) the gas control system, and (4) the gas recycle system. The first two are partially coupled, and the third and fourth are independent.

VI.A.1 Vacuum chamber and pumping system

The main vacuum chamber is a stainless-steel spherical vessel with a 61 cm inner diameter which has a sealed water jacket wrapped around it. This jacket allows for effective cooling of the inner wall. There are 18 conflat ports of varying sizes to enable a spectrum of diagnostic and performance enhancing hardware to be added to the device. When using copper seals and blank flanges and an o-ring between the hemispheres, this chamber has been tested down to $1.3*10^{-6}$ Pa in a helium leak bath. A schematic of the spherical IEC chamber is shown in Figure VI-1:

Figure VI-1: Spherical IEC Main Vacuum Chamber (left: front view, right: 45^o from top view)

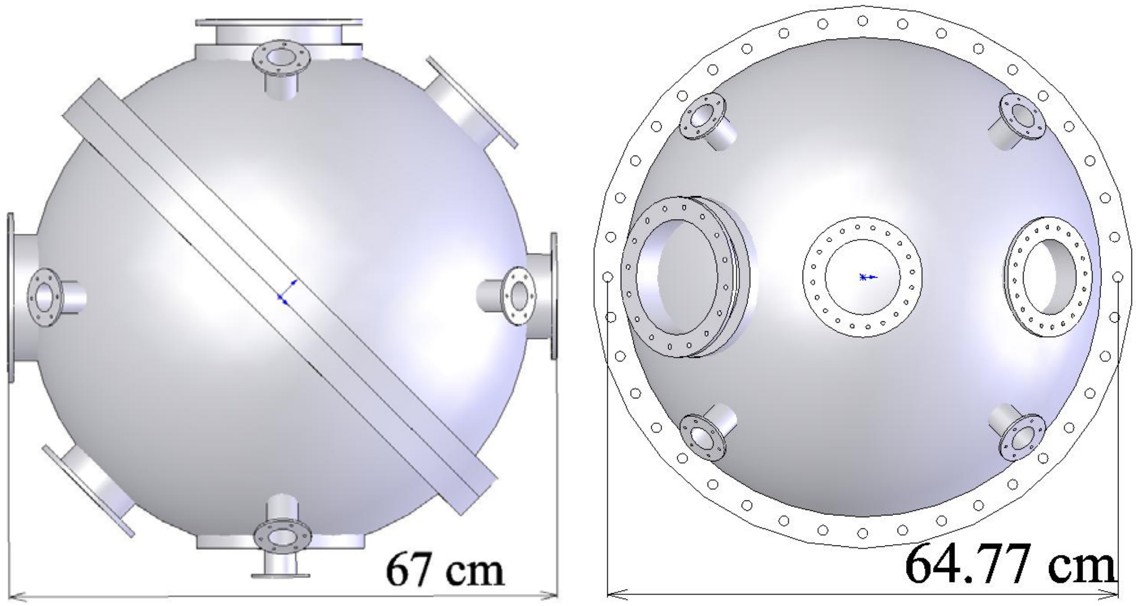

Vacuum is obtained in this system with a 550 l/s Varian MacroTorr turbo-molecular pump, which is connected to the vacuum chamber on an 20 cm conflat elbow for high conductivity. It is exhausted to a 1.1 kW Leybold direct drive roughing pump. The elbow has a 90^o bend in order to keep the pump out of the path of fast electrons from the IEC plasma, which would otherwise damage the rotors. Pumping speed can be adjusted by changing the pump rotational speed and the pressure can be adjusted by a gate valve between the vacuum chamber and the pump.

VI.A.2 Pressure Diagnostics and Gas Flow Control

Pressure measurements are made with a Varian model 580 nude ion gauge, accurate to 10^{-10} torr, and foreline pressure is measured with a thermocouple gauge accurate to 10^{-3} torr. The readout for both of these gauges is a Varian Sentorr model

BA2C gauge controller. Fill gas quality and impurity levels are monitored with a Stanford Research Systems model SRS100 residual gas analyzer (RGA) that can operate both as a closed ion source (CIS) or a RGA. This allows for partial pressure measurements of gasses down to 10^{-8} torr; however amplitude resolution on a large signal is limited to 2-3% of the partial pressure of that gas. A schematic of the vacuum and pressure sensor diagnostics is shown in figure VI-2:

Figure VI-2: IEC Device with Pumping System and Gas Diagnostics

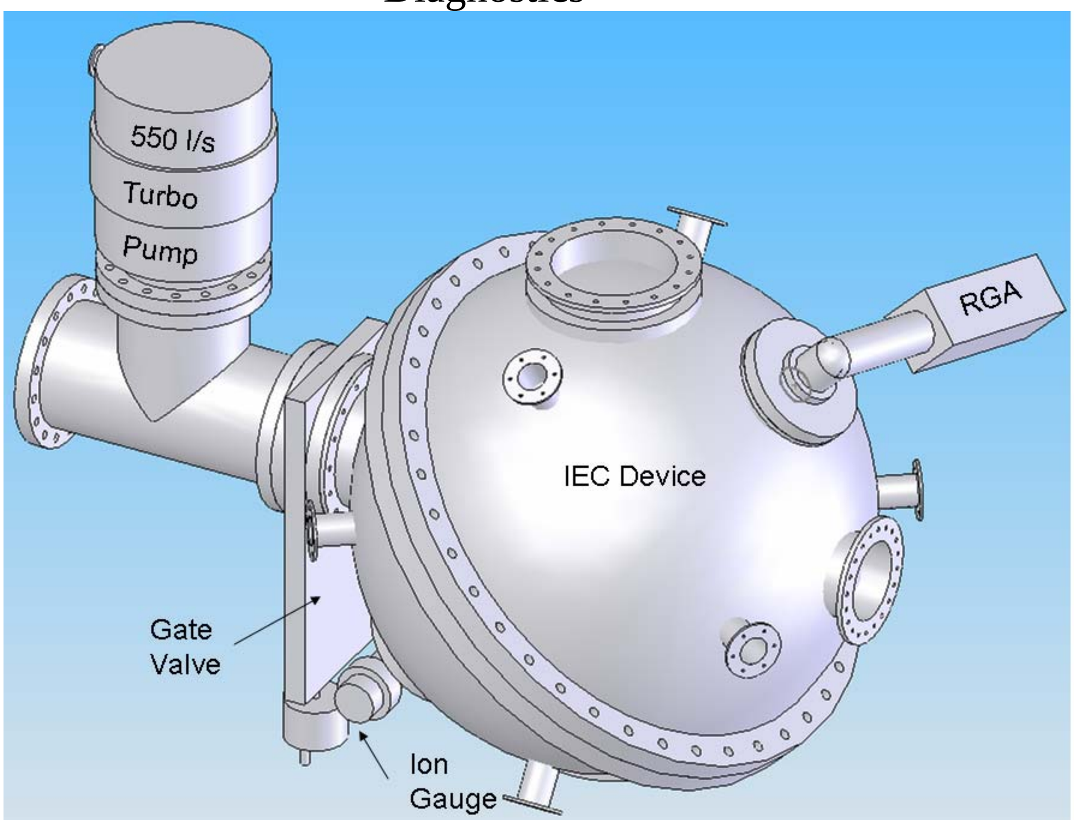

Gas flow is regulated by two different mass flow control systems, one for ^{4}He gas and one for ^{3}He gas. Both systems use two stage regulators and deliver 170 kPa gas to MKS instruments 1179A21CS1AV mass flow controllers. These have a maximum flow of up to 20 standard cubic centimeters per minute (SCCM) and are accurate to within 0.1

SCCM. They are controlled by a MKS 247C four channel readout/control unit. All tubing in the gas fill system is made of copper or stainless steel, and sealed with Swagelok technology. The gas can be fed into the ion source (not pictured) or directly into the main vacuum chamber. Typically, gas would flow first into the ion source and leak into the main chamber at a sufficient rate to generate the pressures desired.

VI.A.3 Gas Recycle System

The gas recycle system is an optional component in the pumping system, and is operated only when extended ^{3}He runs are performed. In this case, exhaust from the turbo-pump is redirected away from the roughing pump and into a two stage cold trap. These traps are 1 liter and 4 liter liquid nitrogen cooled vessels that condense impurity gasses from the exhaust. The remaining (typically helium with a very small amount of hydrogen) gas then flows back into the vessel through high conductance tubing which reduces the need for an additional compression stage. A schematic of the recycle system is shown in figure VI-3:

Figure VI-3: Recycle System Block Diagram

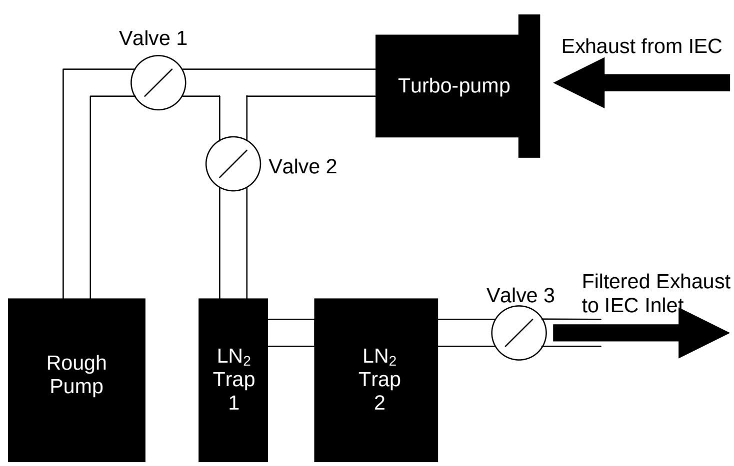

During normal operation, valve 1 is opened and valves 2 and 3 are closed, which vents the turbo-pump exhaust into a large mechanical pump that removes it from the system. During recycle operations, valve 1 is closed, and valves 2 and 3 are opened. This allows the turbo exhaust to be flowed over the LN_2 traps and back into the system. Ceramic insulation of approximately 1 cm thickness surrounds the traps to increase the lifetime of the LN_2 which gives about 1-2 hours of runtime before the traps need to be refilled

VI.A.4 Cooling System

The water jacket is supplied with cold water by a two loop heat exchanger. The secondary loop is open, and the primary loop is a closed system filled with de-ionized water to prevent corrosion of the vacuum chamber welds. Early experiments with this vessel revealed that a single open loop cooling system caused leaks in the welds on multiple occasions due to corrosion. The heat exchanger has 0.7 m^2 of exchange area through thin copper pipes and can handle a maximum flow rate of 120 liters per minute. The secondary loop is typically supplied by cold filtered tap water and the primary loop is driven by a $1/6^{th}$ horsepower 3000 rpm re-circulating pump. A pressure relief valve and a reservoir are installed on the primary side in order to prevent an overpressure should the water boil, and to keep the jacket filled if there are any small losses. A schematic of the cooling system is shown in figure VI-4:

Figure VI-4: Cooling System Block Diagram

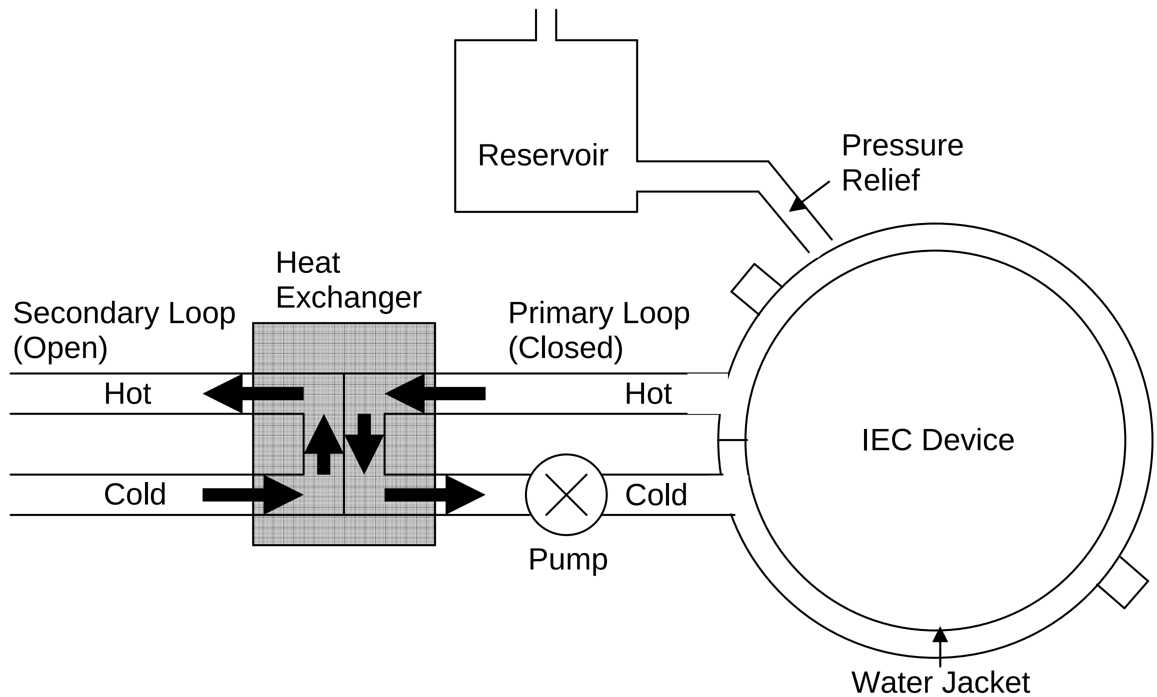

When operating at power levels > 6 kW, the temperature difference between the hot and cold side of the heat exchanger is about 10^{o}C, and both sides of the secondary loop remain cold due to the fact that it has a much higher flow rate..

VI.B. Power Supplies and Buffer Circuit

VI.B.1 High Voltage Power Supply

The high voltage power supply used to supply the cathode grid in these experiments is a Hipotronics model 8200-75. It is a DC power supply fed by a large step-up transformer which is controlled by a 480 V 3 phase variac. The maximum output voltage is about 185 kV at its full load of 75 mA. Ripple on the power supply at full load is 2% of the DC output, and there is a 10% variation in the output level going from no load to full load due to internal resistance. It is oil cooled and insulated by 218 gallons of Diala AX high voltage oil and is rated for continuous duty. The 8200-75 is protected by a fast current sensing circuit that will shut the system off by disconnecting a three phase contactor in between the variac and the transformer. The trip current is adjustable from 10-110% of the supply's rated current. In practical use, the maximum overload limit is reached routinely, and operation of IEC devices at voltages exceeding 50 kV is impossible without some form of buffer circuit. This is due to inherent instabilities in the DC discharge that cause arcing which leads to large currents being pulled from the supply. A picture of the Hipotronics control unit and transformer/rectifier unit is shown in figure VI-5:

Figure VI-5: Hipotronics 8200-75 Transformer (left) and Controller (right)

VI.B.2 Buffer Circuit

As stated earlier, normal operation above 50 kV with the 8200-75 power supply is very difficult due to the inherent instabilities of the IEC discharge. In order to mitigate the effects of arcs, a buffer circuit was designed to limit the amount of current that can be drawn during an arc. A simple way to do this is to add a large resistance in series with the circuit. The value of the resistance should be chosen so that it plays a small role during normal operation, but prevent massive currents during an arc. In addition to limiting current, this resistance will provide a quenching affect on the arcing by dropping additional voltage. Ohm's law dictates the relationship between voltage drop and current in an ideal resistor:

$$\Delta V = I * R \qquad \text{(VI-1)}$$

Where ΔV is the voltage drop across the resistor, I is the current through the resistor, and R is the resistance. The present experiments, the maximum current was limited to roughly 1 A during an arc for safety reasons, and since the maximum voltage we can run at is 200 kV, we chose a resistance of 250 kΩ for our buffer circuit. There is an unfortunate side effect of this high value on normal operation that must be considered—at typical operating currents of 60 mA, there is a noticeable loss of voltage as a result of the presence of the buffer. The voltage drop at 60 mA is 15 kV, and this must be accounted for when determining the actual experimental voltage. The relationship between actual and measured voltage is:

$$V_{cathode} = V_{meter} - I_{meter} * R_{buffer} \qquad \text{(VI-2)}$$

Where V_{meter} is the voltage measured at the output of the 8200-75 power supply, I_{meter} is the current flowing through the buffer circuit, and R_{buffer} is the buffer circuit resistance—in this case $250 \pm 10k\Omega$.

In order to provide a safe work environment, all of the components in the buffer circuit must be kept inside of grounded conducting enclosures. The high voltages used in these experiments would very likely be fatal to a person, so extra precautions have been taken to make sure human contact cannot be made with any high voltage components during operation. These enclosures must also be large enough to dissipate the power generated in the buffer circuit and also must provide sufficient space between different components so that the high voltage cannot arc over the circuit partially or entirely. Since the latter two requirements set the minimum amount of space required, they must be considered first, and then the whole system must be enclosed.

To determine the size of the components, the power dissipation rate was calculated with the formula:

$$P = I^2 R \tag{VI-3}$$

Where I is the current through the resistor and R is the resistance value. For our experiments, the maximum current available is 75 mA, and R is 250 kΩ. This gives a power dissipation of 1.4 kW, and to do this an assembly of eight 125 kΩ, 250 W resistors was used. These were arranged into 4 series sets of 2 parallel resistors which yields a total resistance of 250 kΩ and a total power dissipation capability of 2kW.

The 8 resistors were enclosed in a 55 gallon drum of Envirotemp FR-3 high voltage fire resistant oil in order to improve cooling and eliminate high voltage breakdown. Experience has shown that poor design will not only contribute to shutdowns and failures but can constitute a safety hazard as well. In one case, arcing due to sharp points vaporized a small amount of Diala AX oil inside of the barrel which has a much lower flash point than the FR-3. This vapor formed a mixture which ignited causing a minor explosion. Fortunately the steel drum contained the energy released, but it had visibly deformed and could have caused a fire. To prevent this, great care was taken to make sure all connections were rounded and smooth to prevent large electric fields that can initiate breakdown. Furthermore, careful periodic inspections of all high voltage components are scheduled, the oil was upgraded from Diala AX to FR-3, and nitrogen gas is forced over the top of the oil during all high voltage operation to prevent vapor buildup. A picture of the inside of the buffer circuit components while opened up is shown in figure VI-6:

Figure VI-6: High Voltage Buffer Circuit

The buffer circuit resides in series between the 8200-75 power supply and the IEC device as illustrated in figure VI-7:

Figure VI-7: High Voltage Buffer Circuit Block Diagram

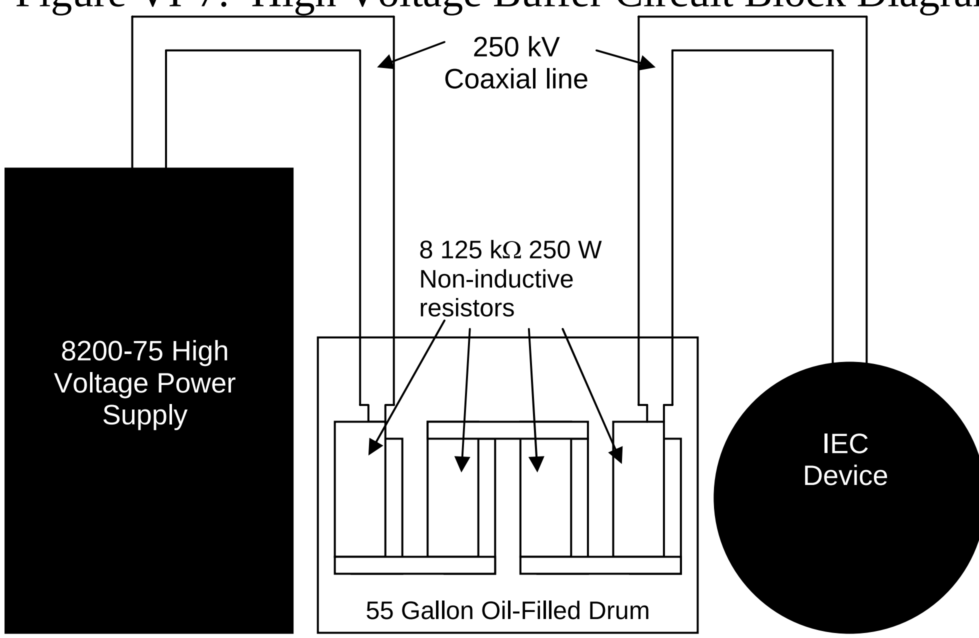

VI.B.3 Non-Ideal Behavior

The actual response of the buffer circuit to instabilities is not ideal. Real resistors have capacitive and inductive components which complicate their response to transients, and the amplitude of this response becomes larger if the transient is fast. Most resistors are wire-wound and can have values of inductance that are in the 10's of mH. The response of such an inductor to a change in current can be described by the equation:

$$V = -L * \frac{dI}{dt} \tag{VI-4}$$

Where V is the voltage induced in the inductor, L is the inductance and dI/dt is the time rate of change of current through the inductor. An early version of the buffer circuit used on the IEC high voltage system used a resistor assembly with an equivalent inductance of about 15 mH. For such an inductance, a change in current of 0.1A/ns can cause an induced voltage as high as 1500 kV. High speed measurement circuits indicate that oscillations during an unstable event happen in the 10's of Mhz range with rise and fall times of at most 10 ns, which means this inductance could produce abnormally large voltages in our circuits. Such large voltages would be destructive to many components in the high voltage system, and therefore it is important to try to minimize the inductance of the buffer circuit resistors.

Capacitance has a similar effect on the time-behavior of the voltage. A circuit with a large capacitance will prevent voltage levels from changing rapidly but allow for higher than normal currents to flow. The relationship between capacitance, current and time rate of change of voltage is:

$$I = C * \frac{dV}{dt} \tag{VI-5}$$

Where C is capacitance, and dV/dt is the time rate of change of voltage across the capacitor. One can see from this description that it might be desirable to have a large capacitance across the output of the buffer circuit to prevent large changes in voltage on the cathode due to inductive fluctuations in the rest of the buffer system that are caused by arcing. This turns out to be a poor solution however, because it supplies additional stored energy to the arc, allowing it to last longer and cause more damage to the grid and insulator materials. Furthermore, an arc that persists for a longer time will pass a greater amount of charge, which will require a greater output from the power supply in order to maintain voltage. This will frequently result in the power supply hitting its overload limit and shutting down. For this reason, there is likely an ideal value of capacitance, which would be based on the resistance and inductance of the buffer, the inductance and capacitance of the 8200-75 power supply, the sensitivity of the overload circuit in the 8200-75, and the characteristic time for arcs to form and quench based on measurements. Unfortunately we were unable to make these measurements accurately enough (1 GHz resolution is likely necessary) and instead added no additional capacitance to the circuit, leaving it with its intrinsic value of 890 ±10 pF. Improvements to stability of operation could almost certainly be obtained by a more detailed investigation of these behaviors.

The characteristics that have been measured or calculated are given in table VI-1:

Table VI-1: Summary of Buffer Circuit Electrical Characteristics

Buffer Circuit Characteristic	Value	Method
Resistance	250 ±10kΩ	Measurement by Ohm-meter
Inductance (wire-wound resistors) (see Appendix B)	12.6 ± 0.1mH	Calculated based on solenoid approximation: $L = \frac{\mu_o N^2 A}{l}$
Inductance (non-inductive design) (see Appendix B)	2.6 ± 0.1μH	Calculated based on coaxial approximation: $L = \frac{\mu_o}{2\pi} \ln\left(\frac{r_o}{r_i}\right)$
Inductance (non-inductive, return path not through shield) (see Appendix B)	10.5 ± 0.1μH	Calculated based on straight wire approximation: $L = 2 * 10^{-7} * l \ln\left(\frac{2l}{r} - 1\right)$
Frequency of ring on arc	~35 Mhz, but limited by response time of measurement circuits	Measured by 100 Mhz oscilloscope, 30 Mhz voltage divider circuit
Amplitude indicated by measurement circuits	> 1 MV	Measured by oscilloscope, voltage divider circuit

VI.C. High Voltage Feed-through/Stalk

A tremendous amount of thought and work has gone into the construction of the high voltage feed-through and stalk components. These components are what allows the high voltage from the power supply to transition into the vacuum chamber and through the plasma environment to the cathode. Due to the same voltages being present as in the buffer circuit, this design also had to be completely contained by a grounded enclosure for safety. It had to provide a vacuum boundary and be able to withstand transient voltages generated by arcs and charge build-up in the plasma environment, as well as provide an easy method to attach the cathode grid to the electrode. Finally, it had to survive the harsh plasma environment.

VI.C.1 Feed-Through

The high voltage feed-through serves as an interconnection between the high voltage cable and the stalk, and also serves as a vacuum boundary. It is filled with Envirotemp FR-3 high voltage oil which serves to prevent arcing and keep the contact cool. The connection between the cable and the stalk is a banana style connector, and is guided into position by a tight fitting sleeve. The sleeve is made from polyvinyl chloride (PVC) and is suitable because of its high dielectric strength and chemical stability with the high voltage oils used. The dielectric strength of the feed-through on the atmosphere side is further enhanced by an additional PVC sleeve that sits between the interconnection and the feed-through wall. The base of the feed-through is equipped with a 2.5 cm Swagelok style fitting that creates the vacuum boundary for the stalk. A schematic of the feed-through is shown in figure VI-8.

Figure VI-8: Two Views of the High Voltage Feedthrough System

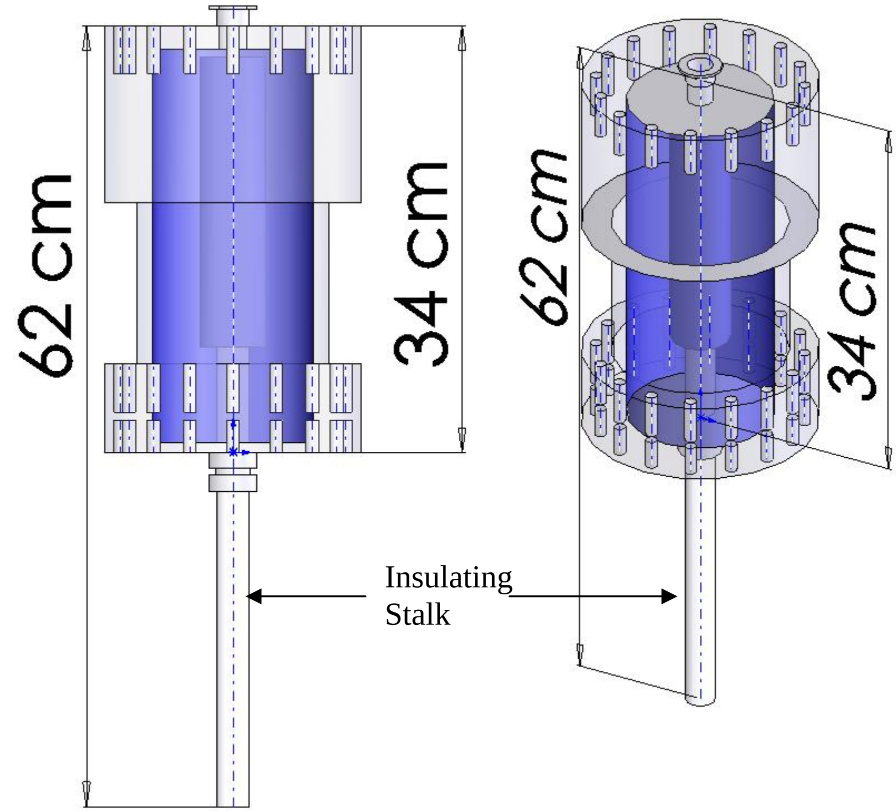

The high voltage stalk consists of an inner conductor and an outer insulating sleeve. Materials for these components must be carefully chosen, since they are subjected to very strong electric fields and an extremely harsh plasma environment. The current design is the result of a theoretical analysis of the material capabilities and extensive experimental testing with a variety of materials, geometries and preparatory processes.

VI.C.2 Stalk Center Conductor

The choice of material for the center conductor is a somewhat simpler matter than choosing the insulator that surrounds it.   Perhaps the most important characteristic is the melting point of the metal. Temperatures of > 1200^{o}C are routinely seen with pyrometer measurements at the connection point between the grid and the stalk. The temperature must not exceed the center conductor's melting point. Another important property is the sputtering coefficient of the metal. This property will be covered more extensively in the section describing grid material, but lower sputtering coefficients cause slower deposition of conductor material onto the stalk insulator, and therefore allow for longer working lifetimes. One more property that is important at high temperature is the metal's thermionic emission coefficient. If a low work function metal was chosen, thermionic electrons would cause inaccuracies in the ion current calculated from the measured cathode current. The metal chosen for its combination of good qualities for these experiments is molybdenum.

The importance of smoothness on the center conductor has been demonstrated multiple times empirically. Stalks with rough inner conductors fail prematurely and at lower voltages than ones where great care is taken to polish the metal. It is worth noting also that any grounded metal outside of, but near to the stalk must also be kept smooth and polished. In at least one case where metal filings became trapped between the stalk and the feed-through, the failure voltage was one half of that which is typically seen and about one third of that which has been demonstrated by the best performers. Because of this issue, all metal surfaces on the vacuum chamber, feed-through and central conductor in these experiments were polished with fine (600 grit) sandpaper. A software package called Maxwell™ can model electric fields from this type of defect, and a simulation of the field enhancement near an imperfection is shown in figure VI-9. The figure shows a very small 0.1 mm tall defect on the conductor (white, circled in black). On the large scale(left), the field enhancement is not noticeable, since it is only short ranged. The close-up on the right side, however shows the same defect at 10,000 times magnification. At this magnification it can be seen that the electric field at the point of the defect is roughly 4 times higher than in the rest of the insulator, which leads to accelerated failure of the insulator:

Figure VI-9: Sharp Defect on Conductor Causes Significant Field Enhancement

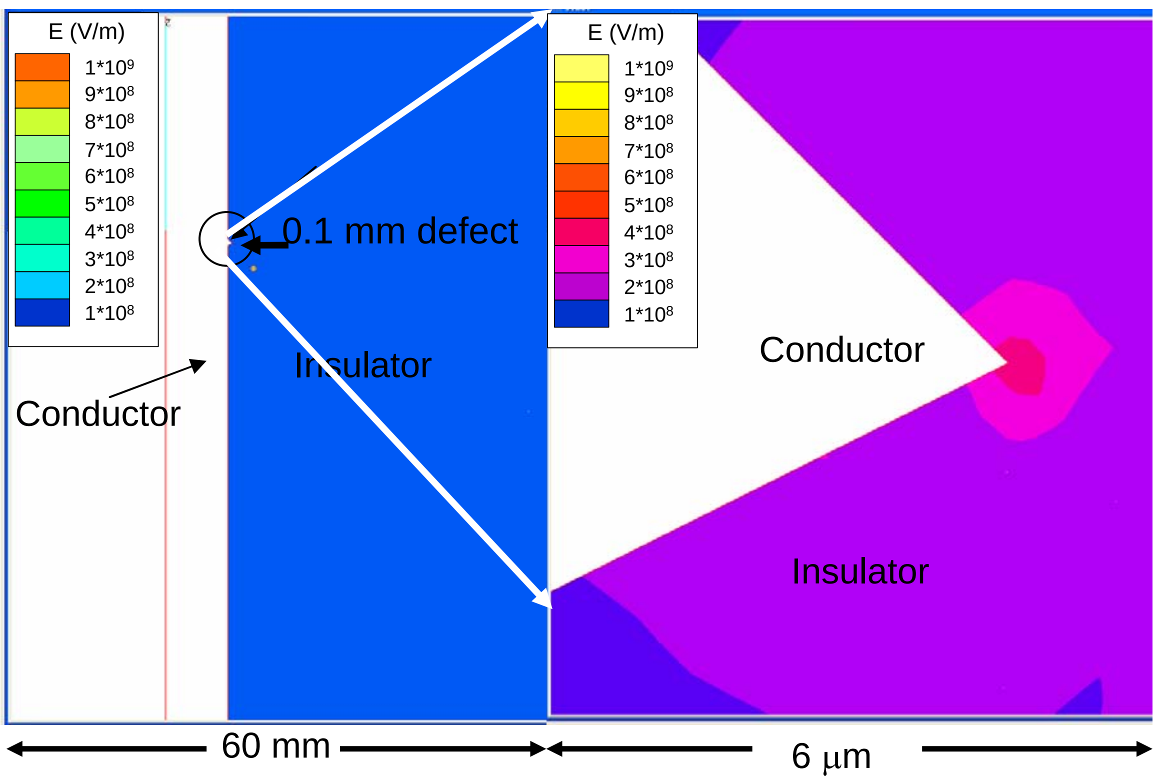

The diameter of the central conductor also has an effect on the strength of the electric field seen by the insulator; however there is little empirical evidence so far to suggest that one diameter conductor fails more easily than any other. Still, an intelligent choice for the inner conductor diameter should be made. From Gauss' law, the electric field around the center conductor of a coaxial cable can be written as:

$$E(r) = \frac{C}{r} \tag{VI-6}$$

Where C is a constant which takes into account the charge density and integration constants and r is the radial distance from the center axis (but constrained to the area between the inner and outer conductors). In order to obtain the value for C, the electric field must be integrated to get potential so the voltage boundary conditions can be applied:

$$-\nabla \phi(r) = \frac{C}{r} \tag{VI-7}$$

$$\Rightarrow \phi(r) = C \ln r + D \tag{VI-8}$$

Where D is another constant of integration. In the IEC configuration, the electric potential is zero on the outer conductor and ϕ_o on the inner conductor. First, D is obtained by using the first boundary condition:

$$\phi(r_o) = 0 = C \ln r_o + D \tag{VI-9}$$

$$\Rightarrow D = -C \ln r_o \tag{VI-10}$$

Now C can be obtained from the last boundary condition:

$$\phi(r) = C \ln r - C \ln r_o \tag{VI-11}$$

$$\phi(r_i) = \phi_o = C \ln r_i - C \ln r_o \tag{VI-12}$$

$$\Rightarrow C = \frac{\phi}{\ln \frac{r_i}{r_o}} \tag{VI-13}$$

Plugging this value of C back into the electric field equation gives:

$$E(r)=\frac{\phi_o}{r\ln\frac{r_i}{r_o}} \qquad \text{(VI-14)}$$

In order to reduce stress on the insulator, it is desirable to find the ratio of r_i to r_o that minimizes this function. By recognizing that the E field is strongest where $r=r_i$, and assigning r_o the arbitrary value of 1 unit of whatever size r_o is, this can be done by differentiating E with respect to r_i and setting the result equal to zero

$$E_{\max}(r_i)=\frac{\phi_o}{r_i\ln\frac{r_i}{r_o}} \qquad \text{(VI-15)}$$

$$dE_{\max}(r_i)=\frac{-\phi_o\left(\ln r_i+1\right)}{\left(r_i\ln r_i\right)^2} \qquad \text{(VI-16)}$$

Then setting the numerator equal to zero:

$$\ln\left(r_i+1\right)=0 \qquad \text{(VI-17)}$$

$$\Rightarrow r_i=\frac{1}{e}=0.368 \qquad \text{(VI-18)}$$

And since this was solved in units of r_o:

$$r_i=0.368r_o \qquad \text{(VI-19)}$$

This is the ratio that theoretically will give the weakest electric field between the two conductors, however it is not necessarily optimum since it does not maximize the insulator thickness. Examining figure VI-10, it can be seen that the field is near minimum for quite a wide range of values of r_i/r_o:

Figure VI-10:

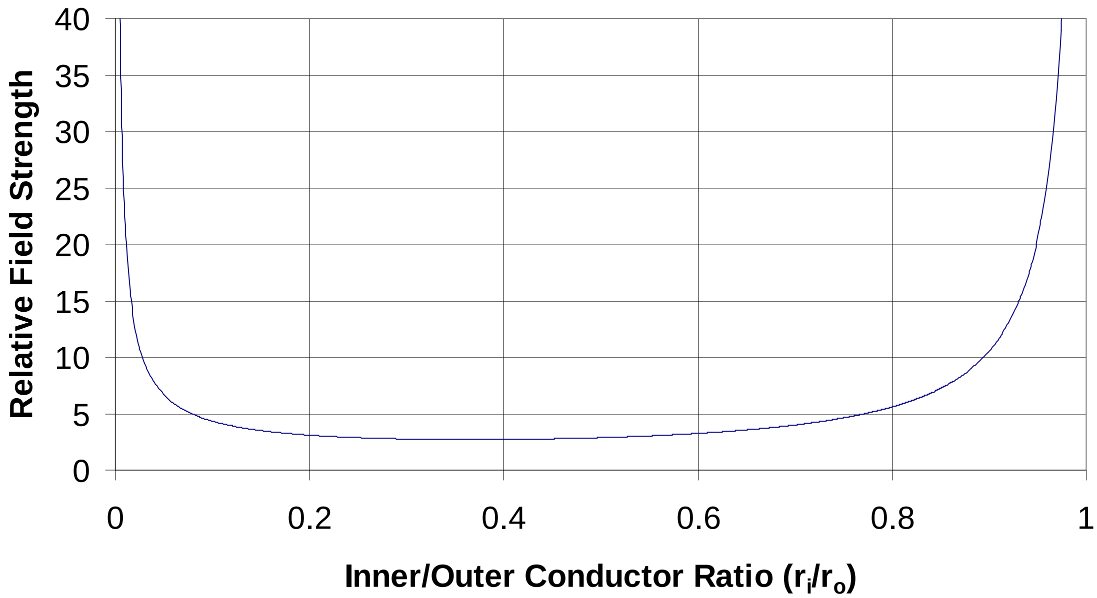

Since this is the case, it makes sense to increase the thickness of the insulator a little more and incur only a slight penalty in the field strength. Due to this and the ease and availability of parts, the inner conductor diameter used in these experiments was chosen to be 0.5 cm, while the outer diameter is 2.5 cm.

VI.C.3 Stalk Insulator Material

The choice of material used in the high voltage insulation system results from the consideration of several factors. The material must be able to withstand high temperatures at high voltages, must be able to serve as a vacuum boundary, and needs to be resistant to bombardment by high energy ions. Finally, the material must be machineable, or at least come in sizes that will fit the hardware we have to work with.

After extensive searching based on calculated values and many trials experimentally, Boron Nitride (BN) was chosen as the best candidate. Previous experiments with Alumina (Al_2O_3), quartz, and mullite insulators had shown them unable to withstand voltages much in excess of 100 kV. BN promised improved dielectric strength, excellent temperature resistance, excellent chemical and plasma resistance, and excellent machineability. Furthermore, BN is not difficult to get in many shapes and sizes, and seems more resistant to sputtered metals than Al_2O_3. The only undesirable characteristic of this material is that it is not impervious to gasses, and thus provides a poor vacuum boundary. A summary table of the relevant properties of BN and a few other insulating materials is shown in table VI-2:

Table VI-2: Summary of Important Properties for Possible Insulator Materials

Material	Dielectric Strength (kV/mm)	Temperature and Plasma Resistance	Vacuum Characteristics	Machineability	Sputtering Resistance
BN	67[1]	Excellent	Fair	Standard tools Excellent	Excellent
Al_2O_3	14.6[2]	Fair	Excellent	Diamond tools Poor	Poor
Mullite	9.8[3]	Good	Excellent	Diamond tools Poor	????
Quartz	30[4]	Good	Excellent	Diamond tools Poor	????
Diamond	1000[5]	Excellent	Excellent	Extremely difficult but thin layers possible	????

1: Saint-Gobain Website: http://www.bn.saint-gobain.com/Data/Element/Product/product.asp?ele_ch_id=P0000000000000001636
2: http://www.accuratus.com/alumox.html
3: http://www.accuratus.com/mullite.html
4: http://www.accuratus.com/fused.html
5: Sp3 website: http://www.sp3inc.com/diamond.htm

The geometry of the high voltage insulator also plays a role in how long it lasts and withstands high voltage surges. The standoff voltage increases as thickness increases, but thicker stalks also tend to intercept more ion flow from the IEC, resulting in lower ion current and lower fusion rates. Furthermore, there has been some evidence that charge build-up on the stalk causes breakdown to increase and device performance to decrease. Many empirical methods have been employed to attempt to improve insulator performance including adding ridges to the material, coating the material with thin layers of metal, filling the void between conductor and insulator with castable ceramic, and preparing the insulator in different fashions. For these experiments, the state of the art is a 2.5 cm diameter BN grade HP stalk with ridges roughly 0.13 cm deep and 0.25 cm apart. The rings extend the entire length of the stalk in the vacuum area and stop where the vacuum seal with the feed-through is made. A schematic of a grooved stalk is shown in figure VI-11:

Figure VI-11: Grooved Stalk

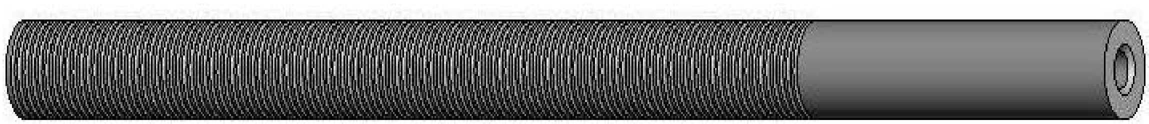

VI.C.4 Stalk Assembly

The Mo conductor is inserted through a hole of slightly larger diameter in the BN and a vacuum seal is made at the top of the stalk with a Torr-Seal or equivalent high vacuum epoxy. The Mo/BN assembly is baked to 300^{o}C in vacuum to remove excess moisture from the BN layer just before installation. The BN material covers all but 2.5 cm of conductor on the oil side for making the connection with the HV line, and all but

7.5 cm of conductor on the vacuum side. The extended conductor on the vacuum side results in improved stability of operation. A small hole with a slightly larger diameter than that of the grid wires is drilled into the bottom of the rod to make the connection. A picture and schematic of the high voltage feed-through installed on the IEC device is shown in figure VI-12:

Figure VI-12: IEC Device Grooved Stalk/Feedthrough Assembly and Schematic of Installed Assembly

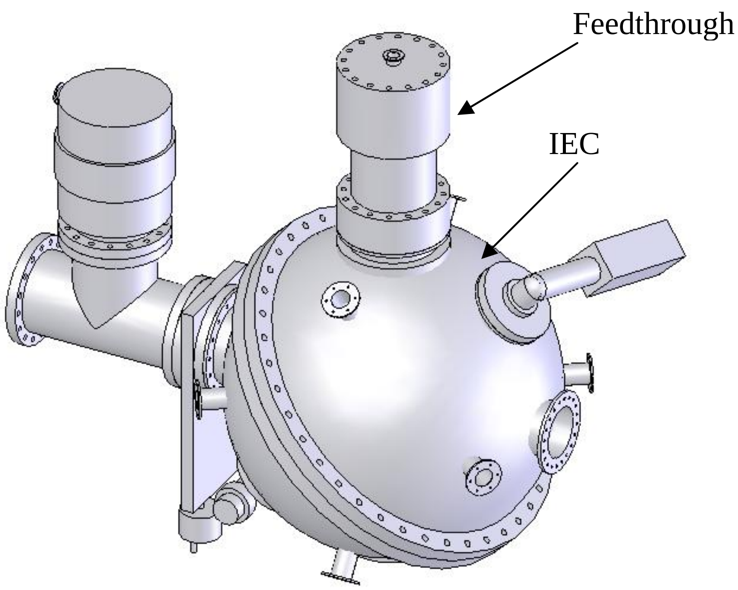

VI.C.5 Stalk Failures

Despite all the efforts made to minimize stresses on the stalk and feed-through, failures still occur. Possibly due to high voltage transients caused by arcs, or imperfections in the construction process, every stalk seems to have a limited lifetime. When they fail, it is almost always in the same way, though not in the same place. The failure always consists of a pinhole sized weakly conductive (10's of kΩ) path through the radius of the insulator. A picture of such a failure is shown in figure VI-13:

Figure VI-13: Pinhole Failure of Insulator (Non-grooved type)

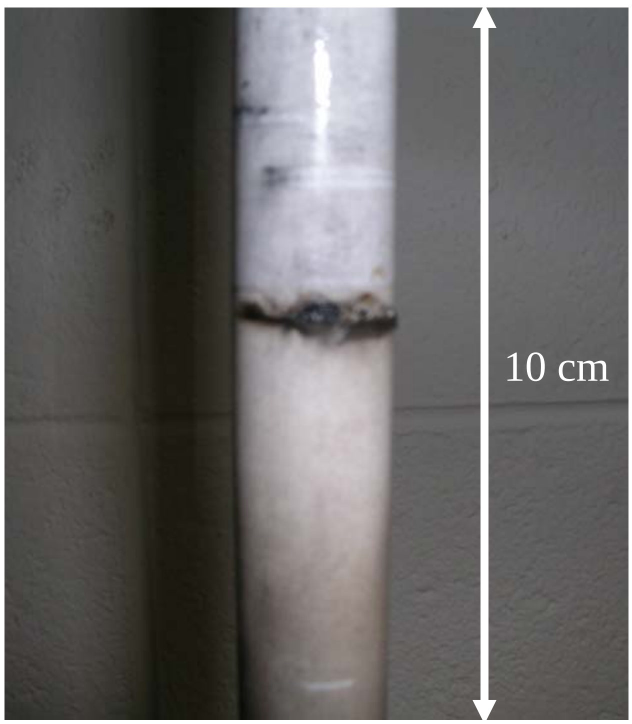

It is currently the belief that these failures are the result of short duration voltage spikes that do not destroy the insulator in one shot, but rather damage it a little bit at a time from the inside out. There are two clues that seem to indicate this: the first is that the insulator is designed to take far more voltage than we apply to it. The stalks that have a 0.5 cm Mo rod, and a 2.5 cm BN insulator should be good for up to 700 kV if the dielectric strength is constant over the entire thickness. Only during arcs do we see voltages in excess of this. Since these transients are so short lived—around 100 ns, it is not likely they would be able to do enough damage in one shot to destroy the insulator.

The second clue was an analysis performed by David Boris and Greg Sviatoslavsky of the UW-Madison. They cut a failed stalk near the point of failure, and shaved thin layers off it in order to follow the path of the arc. Pictures were taken at different depths, and then combined into a composite diagram that shows the arc path. A visualization of the failure path is shown in figure VI-14 (circled dots mark actual measurements at different heights):

Figure VI-14: Arc Path Visualization

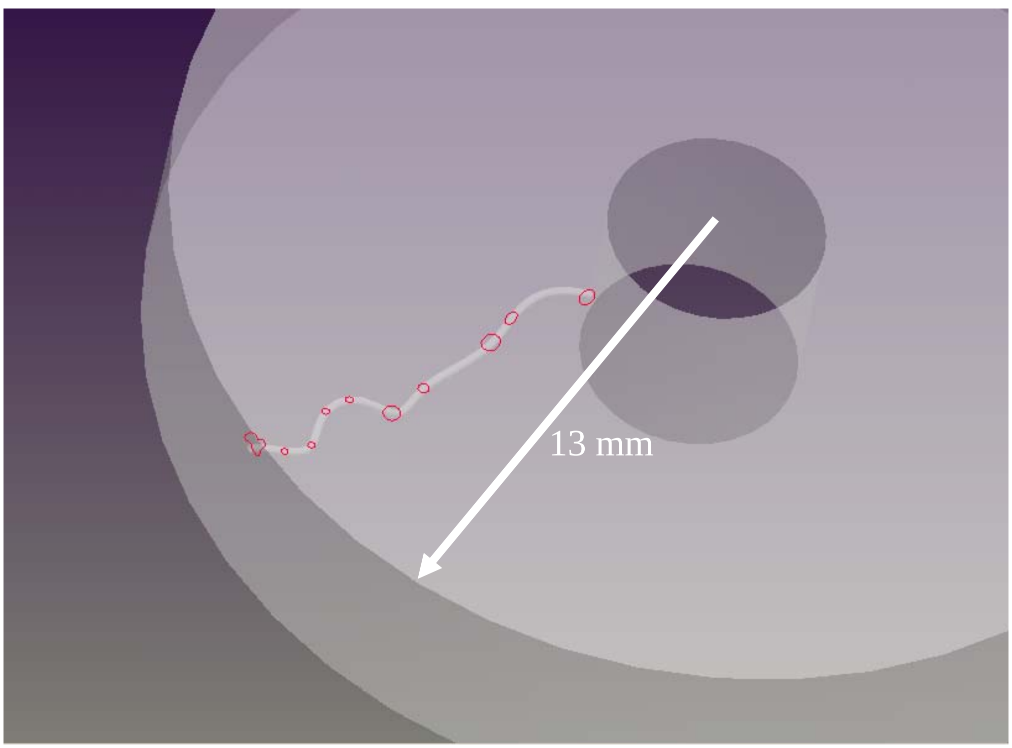

If the failure happened all at once it would be unlikely to have such a non-linear path. Furthermore, this analysis showed several other tracks such as the one above within the failed stalk that had not yet reached the outer edge of the stalk. This evidence indicates that damage occurs from the inside out, and is not caused by fast ions moving inward.

VI.D. Cathode Grid

Perhaps the most obvious hallmark of an IEC device is the glowing cathode grid. A couple of pictures of IEC cathodes in operation are shown in Figure VI-15:

Figure VI-15: IEC Cathodes in D_2 gas at ~ 1 Pa

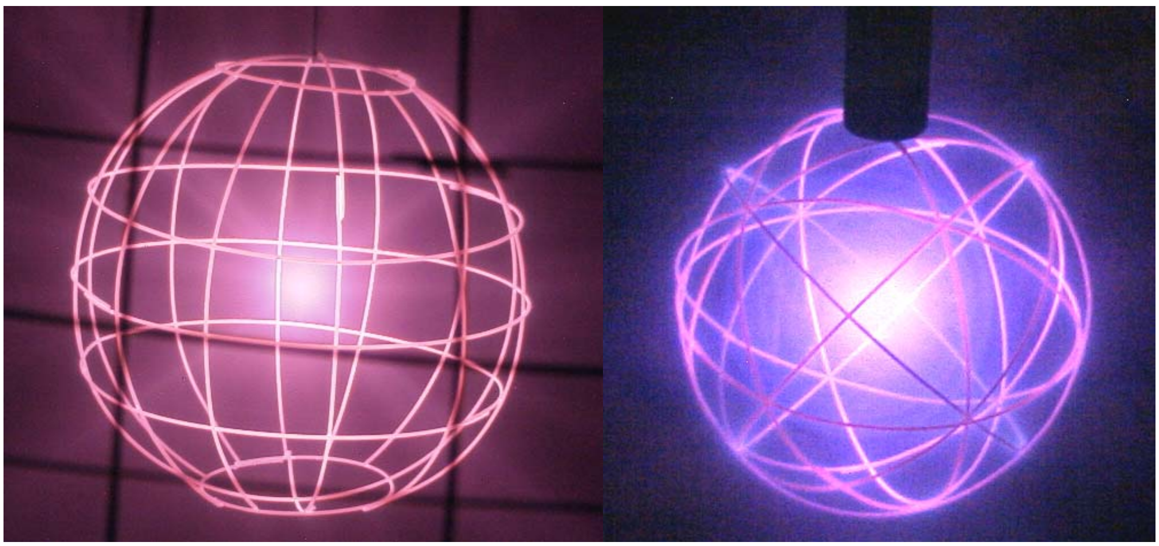

VI.D.1 Materials

It is at the cathode where ions are at their highest energy, and where fusion is most likely to occur. It is also the most intense area of the device, suffering bombardment by the highest density of ions at velocities equivalent to those of particles at billions of degrees C. The choice of material for a grid to survive in this environment is critical. Many metals would simply melt at the power levels per unit area involved in these experiments. Others might survive the high temperatures but emit thermionic electrons causing excessive power loss in the device. Sputtering should be considered as well, since insulator lifetime seems dependent on the rate at which metal from the grid deposits on the stalk. Conventional wisdom was that low sputtering was desired, however recent experiments seem to indicate that BN stalks with thin metallic coatings on them may perform better than those with virgin surfaces, and therefore a higher sputtering coefficient may lead to a faster conditioning process. Another consideration is the resistance the metal has to damage by ion irradiation. For these experiments, He gas was the primary ion type and He irradiation tends to be extremely damaging to metal surfaces. Figures VI-16 illustrates the difference between an un-irradiated and irradiated surface. The irradiated surface experienced a flux of > 10^{19} He atoms / cm^2 as a result of extended use in an IEC device:

Figures VI-16: Unirradiated W Sample (left) and Irradiated W-Re Alloy Grid Wire (right)

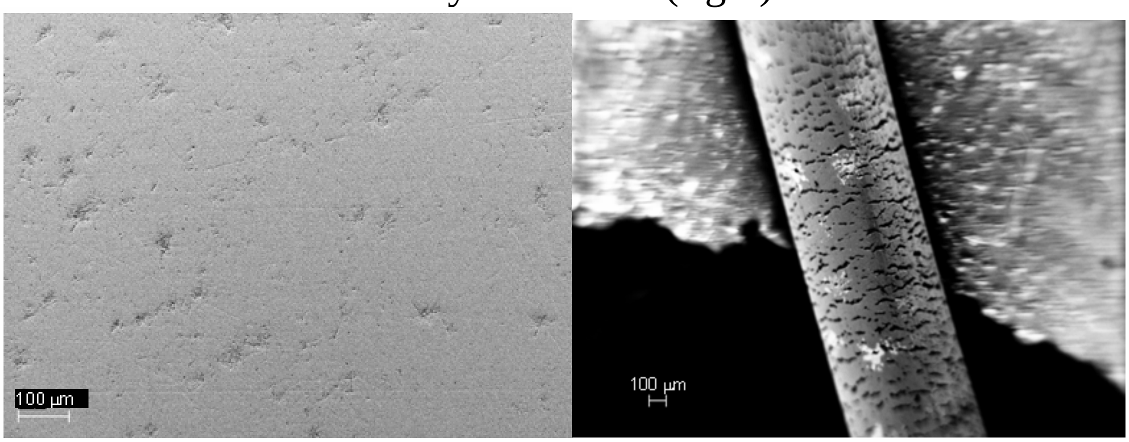

A closer view of the grid wire shows an unfortunate dendritic-like structure that forms:

Figure VI-17: High Magnification Shows Dendritic-like Growth on W-Re

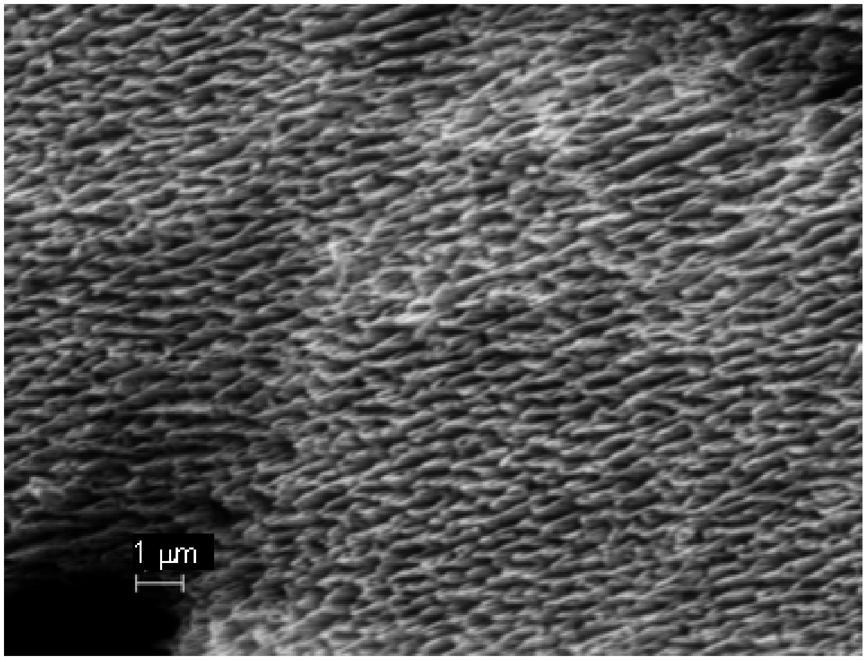

This structure will likely enhance the local electric field at the tips of these dendrites which has the effect of increasing the rate of arcing, shutdown, and damage to high voltage components during IEC operation.

While operating at high temperature, no material known to this author is immune to damage from He irradiation that would also serve as a good cathode material. Recent indications however suggest that. A summary table of some of the materials tried in these experiments is listed in table VI-3, along with their important characteristics:

Table VI-3: Summary of Important Properties of Select Grid Materials

Material	Melting Point	Work Function	Secondary Emission Coefficient at 100 kV (He perp incidence)	Sputtering Coefficient at 20 kV (He perp incidence)
75%W-25%Re	~3300°C	NA but TE can be a problem at high power levels	NA	0.02 (W)[1]
Stainless Steel	~1400 C Melts at high power	Melts before TE occurs	NA	0.08 (Fe)[1]
W	3407°C	4.55 eV TE can be a problem at high power	2.9[2]	0.02[1]
Nb	2468°C	4.3 eV TE can be a problem at high power	NA	0.03[1]
Ta	2996°C	4.25 eV TE can be a problem at high power	NA	0.025[1]
Re	3180°C	4.96 eV	NA	0.035[1]

NA=Not Availible TE=Thermionic Emission

1: Data from NIFS DATABASE at https://dbshino.nifs.ac.jp
2: L. N. Large, "Secondary Electron Emission from a Clean Tungsten Surface Bombarded by Various Positive Ions," *Proc. Phys. Soc.*, **81**, p.1101 (1963)

Experiences with all of these materials have suggested that W-Re or Re are the best material choices for high voltage He operation.

VI.D.2 Geometry

The geometry of the grid has been seen to have little effect on standard IEC operation [1,2]. Most experiments however were performed under conditions where the background gas pressure was high, and likely attenuated the ion flow before grid effects could become substantial. The present experiments were conducted at a considerably lower pressure, and the ion source was a single point source instead of a distributed source. This resulted in the ions recirculating in a beam-like geometry and heavy attenuation of the primary ion flow occured when grid wires intersected the beam. Furthermore, the collision of the primary beam with the grid wires caused excessive heating of those wires and it became impossible to run at the desired power levels since thermionic emission became overwhelming. A picture of a standard cathode grid with the primary beam incident on the wires is shown in figure VI-18:

Figure VI-18: Heavy Attenuation of Primary Beam with Standard Cathode Design

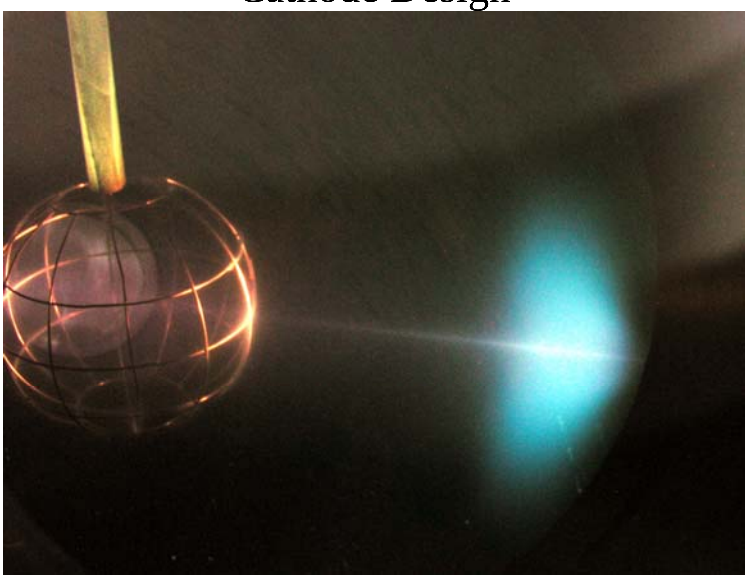

As a result of this problem, two solutions were attempted: The first was to install a cylindrical cathode whose axis was along the beam, and the second was to install a standard spherical grid but remove the wire sections that intersected the beam. The cylindrical solution worked well for distributing the beam, but proved problematic when trying to reach high voltages. A picture of the cylindrical grid in operation is shown in figure VI-19:

Figure VI-19: Cylindrical Grid Design Limits First Pass Attenuation

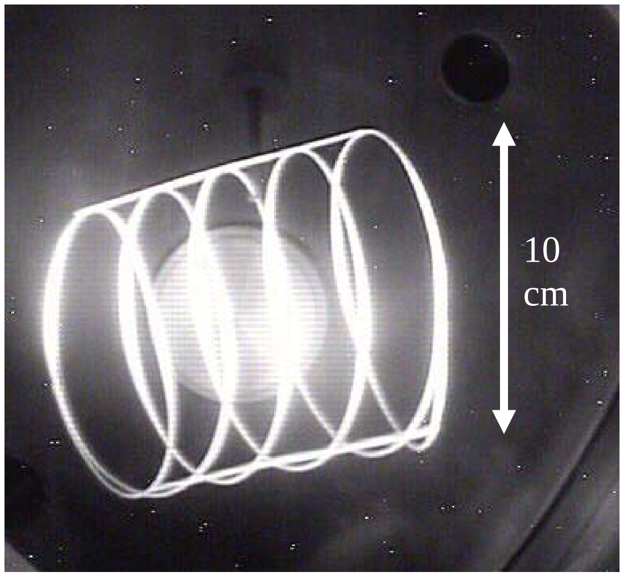

The spherical grid that was used for these experiments was a 10 cm diameter W-Re or Re grid. The grid wires were oriented such that the grid surface was divided into equal area triangles. The wires that crossed the ion beam primary were removed and the grid was attached to the feed-through by breaking a weld on top of the grid and inserting it through the small hole in the stalk. The weld was then redone and the grid was locked into its hanging position. A picture of a full grid just after construction and before the wires were cut is shown in figures VI-20. Also shown is a picture of the spherical grid during a high power run with the cross wires removed:

Figures VI-20: Equal Area Grid Design (Left) and Grid Operating with Wires on Beamline Removed (Right)

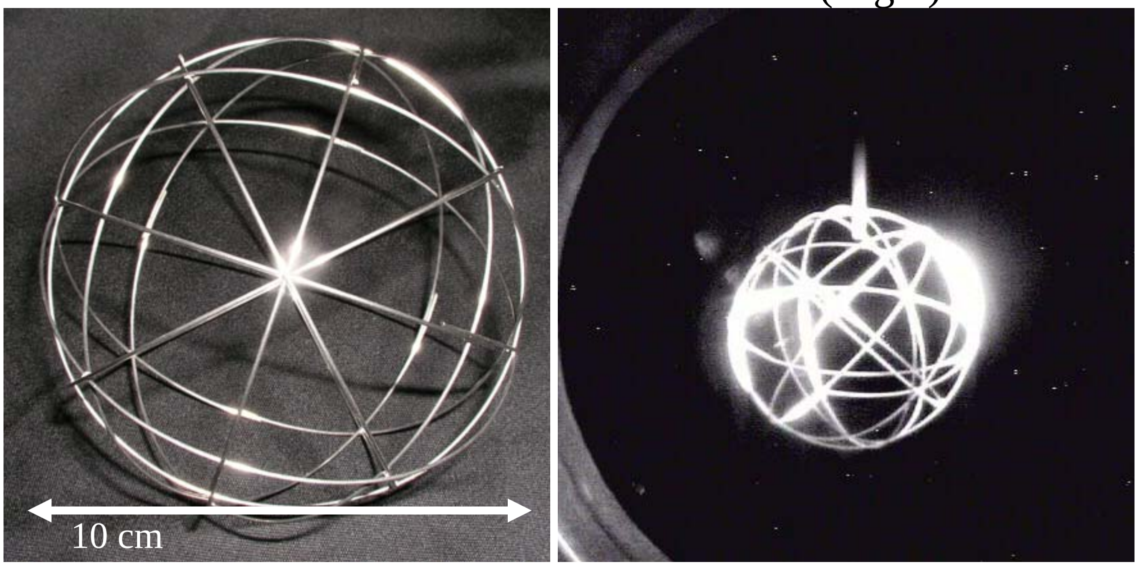

One additional factor that is worth mentioning, but was not studied extensively in these experiments, is the fact helium gas tends to become trapped in metals. The maximum helium density for different materials has not been well measured yet, but current estimates for W metal places the embedded density in the range of 4% [1] to 40% [3] of the metal atom density. Measurements for other materials like Rhenium have not yet been done.

VI.E. Ion Source

VI.E.1 Source Types

The low gas pressures used in these experiments (~ 0.2 mtorr) and the low ionization cross section of He made standard filament assisted discharges impossible. Therefore, it seemed logical to design a plasma source that generated ions from a higher pressure gas outside of the main vessel, and then extract these ions preferentially into the

IEC. The source density requirements discussed earlier indicated a high density source would probably be required, but hardware limitations restricted the rate at which different concepts could be tested, and so we used what was available at the time. Initial designs of this source included DC, capacitive and inductive discharge sources that were differentially pumped. The DC and capacitive sources were of essentially identical construction and were built inside of a 25 cm Huntington vacuum chamber. A schematic of the layout used for these ion sources is shown in figure VI-21:

Figure VI-21: Schematic of Ion Source Design for Capacitive and DC Discharges

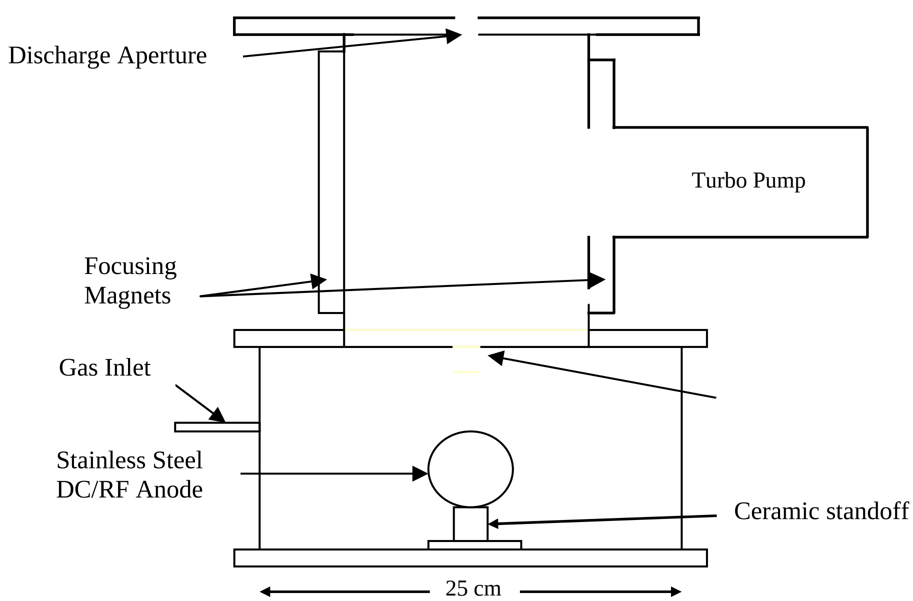

Visible discharges were obtained in both the DC and RF versions of this source, and it was possible to operate with a discharge in the source and have the desired pressure in the IEC vessel. The extractable ion current however, was not measurable. This was because the measurement circuit was not accurate at low currents, but it was confirmed that less than 0.1 mA of beam current was generated.

With more RF experience, and as newer, higher power equipment became available, a more intense source was designed. This was an inductive source that consisted of a five turn copper tube wrapped around a 2.5 cm diameter Al_2O_3 tube. Gas was fed into the bottom of the tube which was in turn connected to the differential pumping section. Relatively intense discharges were possible in this source, however thermal stress on the tube often caused it to crack and leak. A picture of this source in operation is shown in figures VI-22, as well as the ion beam discharging into the main IEC device:

Figures VI-22: Inductive Ion Source (Left) and Ion Beam Generated by Inductive Source (Right)

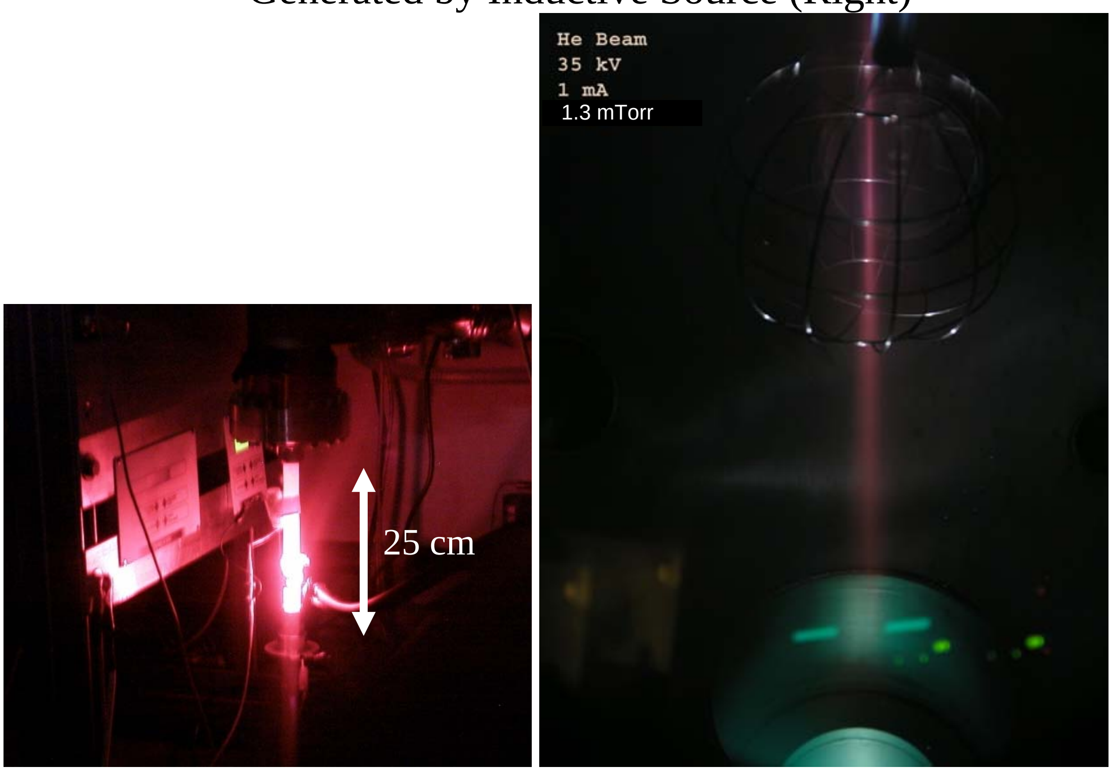

A quartz tube eventually replaced the alumina tube since it was much more resistant to thermal stress. Furthermore, the beam was oriented horizontally so the stalk would not be in the direct beam path. A picture of this source is shown in figure VI-23:

Figure VI-23: Quartz Inductive Ion Source

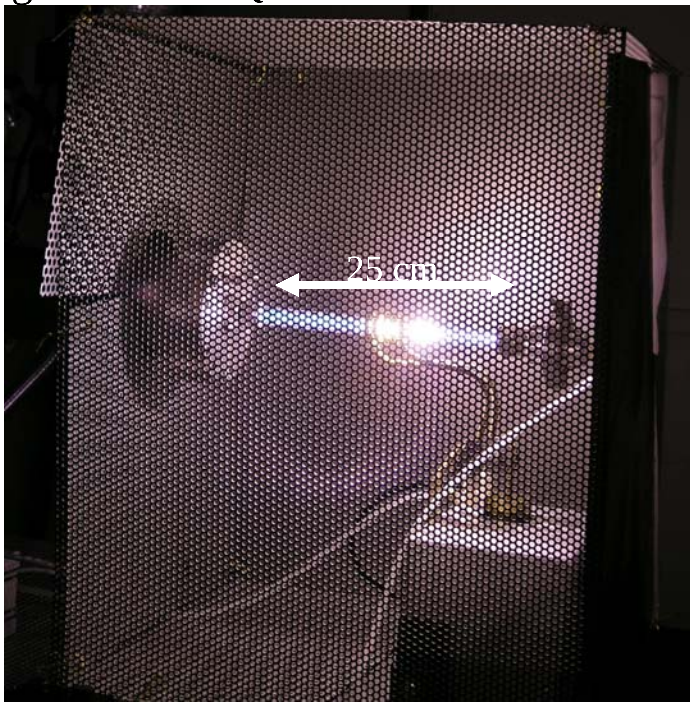

This source was successful at producing ion beams that were measurable (around 1mA cathode current) but was not able to operate at pressures low enough to be suitable for these experiments.

Since the desired cathode current was about 30 mA, and lower pressure was needed, still another source was developed. The highest density relatively low pressure steady state source known is a helicon source, and so with equipment and experience now permitting, efforts were directed toward making such a source work. Helicon sources are somewhat more complicated, and need a magnetic field and an antenna whose geometry is capable of launching helicon waves. A description of the different components of the helicon source now in use at the UW follows.

VI.E.2 Helicon Source Physical Layout

The helicon source vacuum area consists of a 52mm ID 56mm OD quartz tube that is 44 cm long and sealed on both ends by o-ring compression seals. Quartz is required because of its low thermal expansion coefficient. The inlet end is inserted into a brass coupler which has a 6 mm Swagelok fitting soldered into it to allow for easy connection to a gas feed system. The outlet end of the tube is inserted into a stainless steel coupler that is in turn welded to a 11.4 cm conflat flange to allow for easy mating to the IEC vacuum chamber. The front and back seals, as well as the conflat mating flange have water cooling lines soldered to them to ensure a good heat rejection. The inlet o-ring is made of Viton rubber and the outlet o-ring is made of Kalrez perflouroelastomer. The exotic material for the outlet o-ring is required since the temperature of the quartz tube near the o-ring reaches > 260^{o}C. Even with the Kalrez material, a radiative and insulating shield is necessary to prevent plasma light and collisional heating of the wall from causing even higher temperatures. This shield is made from castable alumina and is in the form of a sleeve that is inserted into the quartz tube. Also on the outlet side of the source, there is an aperture which restricts the flow of neutral gas and focuses the beam. It is made of iron and further serves to shield fringing magnetic fields from the extraction area. A drawing of the ion source is shown in figures VI-24, as well as a schematic showing it connected to the IEC device:

Figures VI-24: Helicon Source Model (Left) Mated to IEC Device (Right)

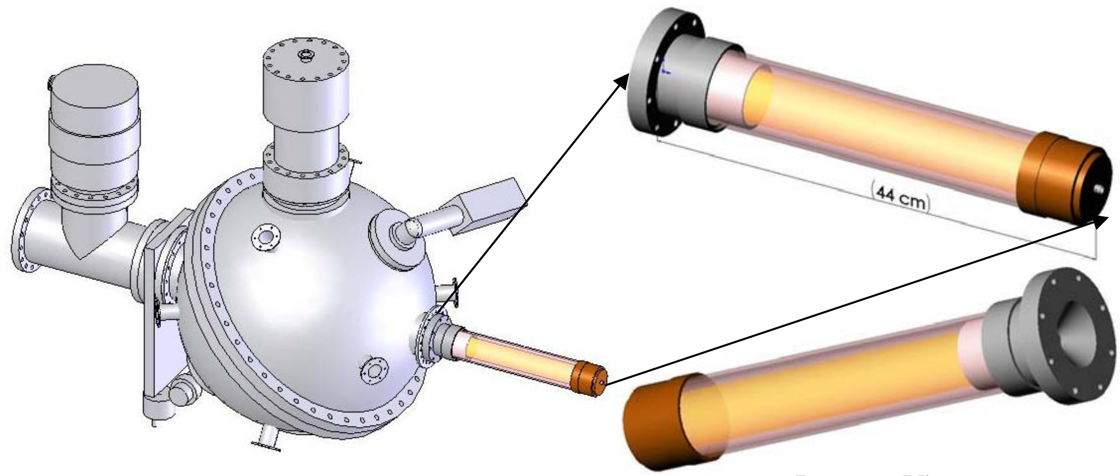

VI.E.3 Helicon Source Electrical Setup

In order to generate a helicon plasma, an antenna must be designed in such a way as to launch helicon waves. There are several antenna configurations that have been tested by many research groups, but the Nagoya III design stood out because of its ease of construction, high efficiency, and good documentation. For this ion source, the antenna had an ID of 58mm, and a length of 80mm. An illustration of the Nagoya III antenna used on this source is shown in figure VI-25:

Figure VI-25: Nagoya III Antenna (Left) Installed (Right)

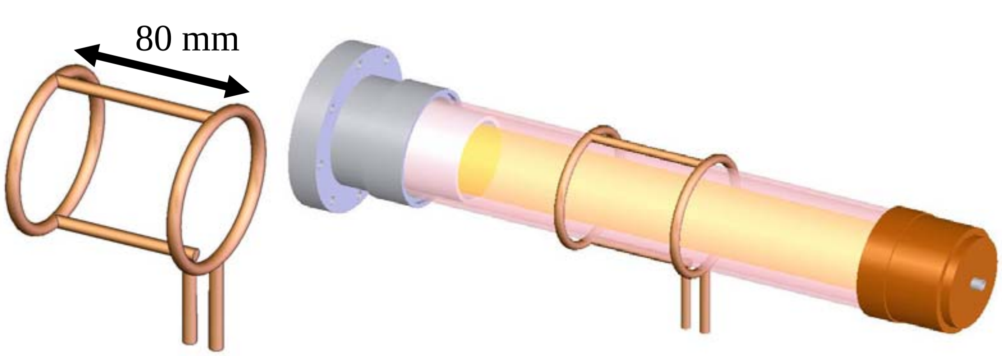

The antenna is made from 6mm copper tubing so that it can be water cooled and standard tube unions are used to make the junctions. The back lead of the antenna is connected to the matching circuit and the more forward lead is connected to ground.

The small size of this antenna makes operating at high power levels very difficult. Its configuration has a low radiation resistance and therefore needs very high current flow to couple the power from the RF power supply into the plasma. It is not unusual for antenna voltages to reach ~ 2000 V RF during normal operation. Such voltages and currents cause resistive heating to become a run-away problem with increased wire temperature causing increased resistance which in turn causes the wire to get even hotter. Therefore, all components in the matching circuit as well as the antenna require water cooling if any run longer than about a minute are expected. Many antenna designs were tried that were not actively cooled and all of them melted.

Another complication arises from the wide range of source impedance when there is no plasma compared to when there is very dense plasma. The effective radiation resistance of the antenna increases dramatically when plasma is present and therefore the matching circuit must be adjusted in order to keep efficient power transfer from the RF generator to the antenna. In order to match most RF generators the matching circuit must transform the impedance of the antenna from its natural value to $Z=50 + 0j\ \Omega$ (j designates the imaginary component). To do this, a simple ‘L’ type matching circuit was designed. A schematic and picture of the matching circuit used is shown in figures VI-26:

Figures VI-26: "L" Type Matching Circuit used for the Helicon Source

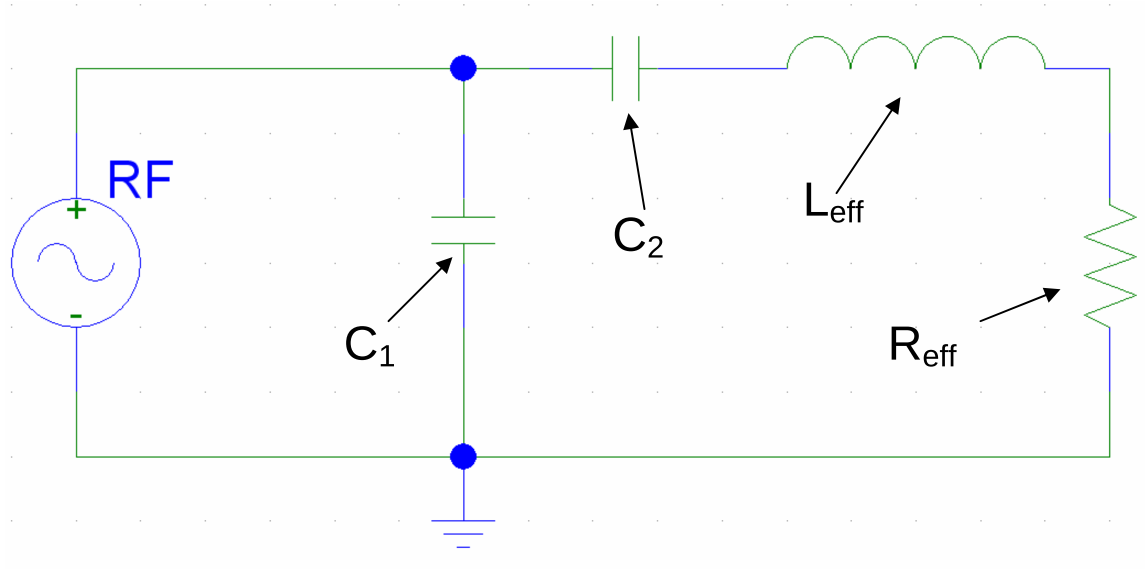

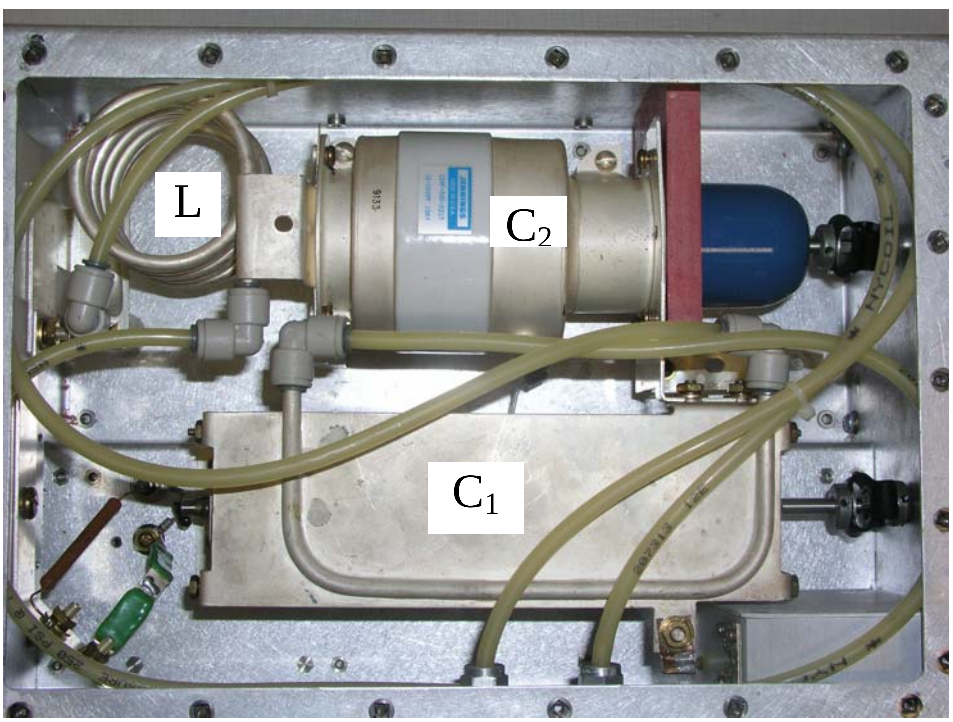

For this type of matching circuit, L_{eff} and R_{eff} are uncontrolled variables dependent on the physical properties of the matching circuit, the antenna, and the plasma. L_{eff} is the sum of the matching circuit and antenna inductance, and R_{eff} is the sum of the ohmic resistances of the matching circuit and the antenna as well as that due to radiation resistance and is often called the feedpoint resistance. C_1 and C_2 are both variable capacitors that can be adjusted to meet the impedance requirement needed by the generator. The two capacitors are needed to meet the two impedence conditions required—the real part of Z must be equal to 50 Ω and the imaginary part must be 0. The effective impedance of this circuit is:

$$Z_{eff} = 50 + 0j = \left(\frac{1}{Z_{C1}} + \frac{1}{Z_{C2} + Z_{Leff} + Z_{\mathrm{Re}\,ff}} \right)^{-1} \qquad \text{(VI-20)}$$

where:

$$Z_{c1} = \frac{1}{j\omega C_1}, Z_{C2} = \frac{1}{j\omega C_2}, Z_{leff} = j\omega L_{eff}, Z_{\mathrm{Re}\,ff} = R_{eff} \qquad \text{(VI-21)}$$

After some algebra, the following matching equations are obtained:

from the imaginary part:

$$50C_1 - 50\omega^2 C_1 C_2 L + 50C_2 - C_2 R = 0 \qquad \text{(VI-22)}$$

And from the real part:

$$1 + 50\omega^2 C_1 C_2 R - \omega^2 C_2 L = 0 \qquad \text{(VI-23)}$$

From these two equations, values of C_1 and C_2 can be chosen if all of the other values are known. As stated earlier, the value of R is dependent on conditions in the plasma, but ω is 13.56 Mhz. The value of L_{eff}, while also dependent on the plasma, can be dominated by an inductance put into the matching circuit, and in this case is approximately 5 μH. Curves of the values for C_1 and C_2 that provide the match condition versus loadpoint resistance are plotted in figures VI-27

Figures VI-27 Value of C_1 and C_2 Required to Match Given Loadpoint Resistance

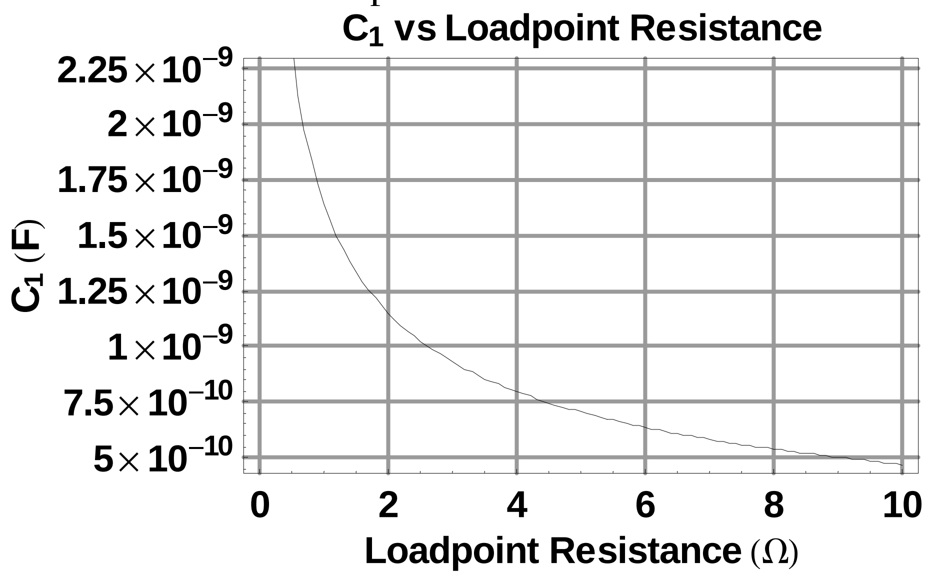

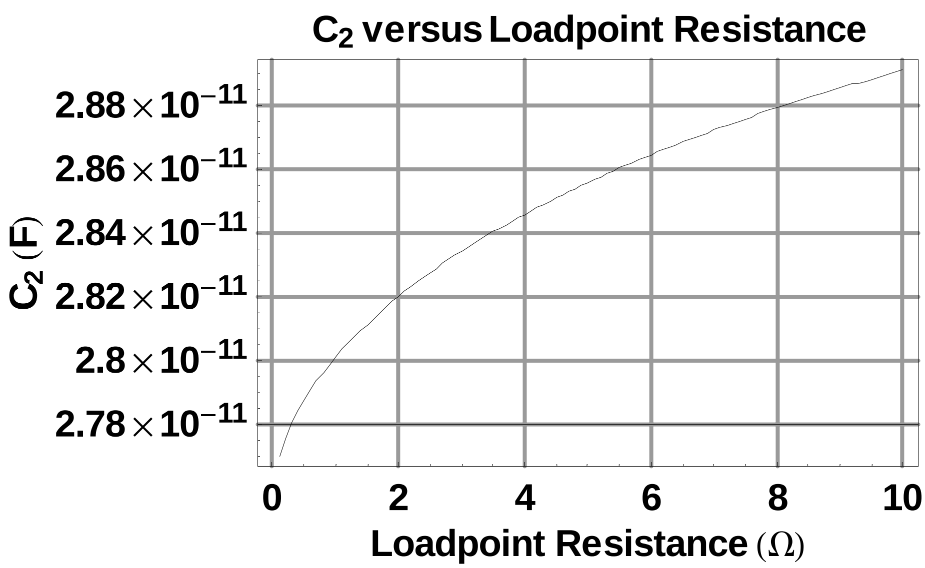

Note that the calculations above are used as design guidelines only, intended to give a range over which C_1 and C_2 should be able to extend. This design must include a considerable margin for error, and real matching must be done empirically with measurements of forward and reflected power, as well as measurements of the amplitude of the RF voltage on the antenna. The matching circuit used for this source is an automatically tuning Advanced Energy AZX-90 modified with fixed capacitors to bring the standard C_1 and C_2 ranges to those desired for this application. When a discharge is present, it will tune the rf circuit to provide less than 1% reflected power. It adjusts adaptively as source conditions are changed and is therefore ideal when variability of the ion source density is required.

This source has been operated at up to 3 kW for a short time and at 2 kW for steady state operation. Extended operation at 3 kW would be likely to melt even the exotic Kalrez o-ring on the front end of the source.

The RF power was supplied to the matching circuit through a 13.56 Mhz 0-3kW Comdel model CPS-3000 power supply.

VI.E.4 Source Electromagnets

A necessary component in any helicon type source is a magnetic field. This field can be generated with electromagnets or with permanent magnets, and in this case an electromagnet was used in order to have additional control over the source density. Earlier versions of the ion source used very large water cooled electromagnets which were inefficient, hard to align, and had fringing fields that extended well into the IEC device or extraction section. A picture of these magnets in operation along with a picture of the plasma with the magnets poorly aligned is shown in figures VI-28:

Figures VI-28: First Generation Helicon Source Suffered from Alignment Difficulties

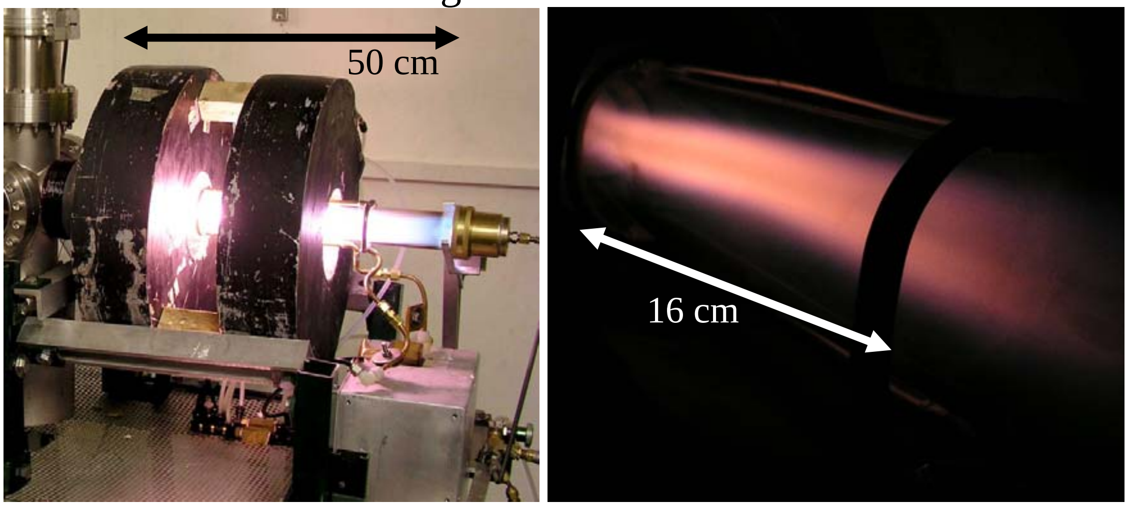

The current magnet system is a modified, water cooled Varian commercial electromagnet pair, which is enclosed in a ferritic cage. This cage minimizes fringing fields and provides a solid mount so that the magnets can be well aligned. Furthermore, the magnets are a more compact design, which means they are more efficient and actually turn out to use about 10% of the power of the previous ones for a given field. The field may be varied continuously from < 1 G to 2 kG which provides excellent control over the ion current output by controlling the source density. A picture of the source with these magnets as well as one showing the source coupled to the IEC device is shown in figures VI-29:

Figures VI-29: Second Generation Helicon Source

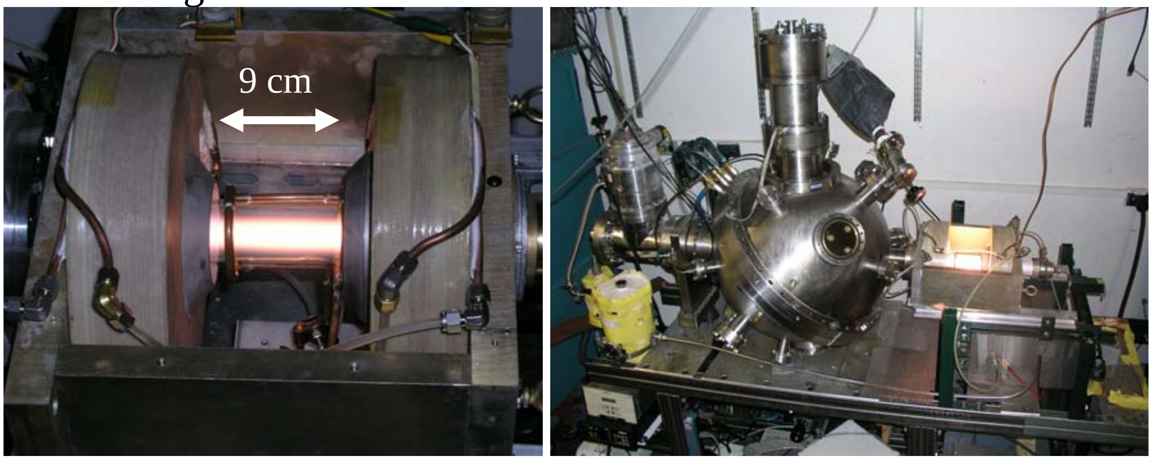

These magnets are operated by a 0-150 VDC power supply which consists of a homemade full-wave rectifier with a large ballast capacitor to minimize ripple that is driven by a simple variac. A long exposure photograph of the device operating with this helicon source at low power is shown in figure VI-30 (the white circle inside the grid is a viewport on the opposite side of the vacuum chamber):

Figure VI-30: High Exposure Photo of Ion Beam

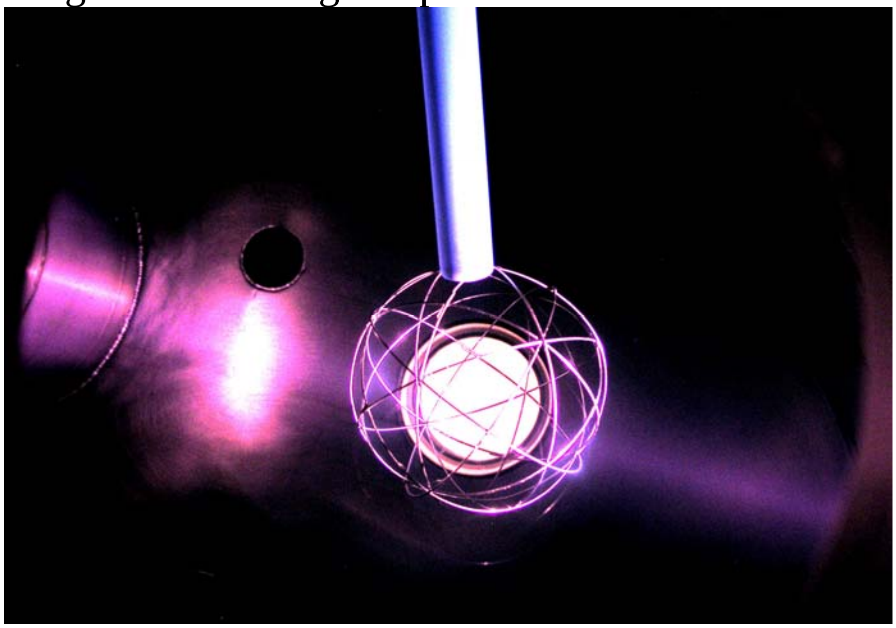

VI.E.5 Extraction Section

An earlier design of the ion source included a region over which ions would be accelerated and neutral gas would be differentially pumped out in order to generate even lower operational pressures in the IEC. This system incorporated a high voltage acceleration electrode that would move the ions quickly across the region whereas neutral gas was more likely to be removed by a turbo-pump. A schematic and picture of one of the extraction systems used is shown in figures VI-31:

Figures VI-31: 2nd Generation Source with Differential Pumping

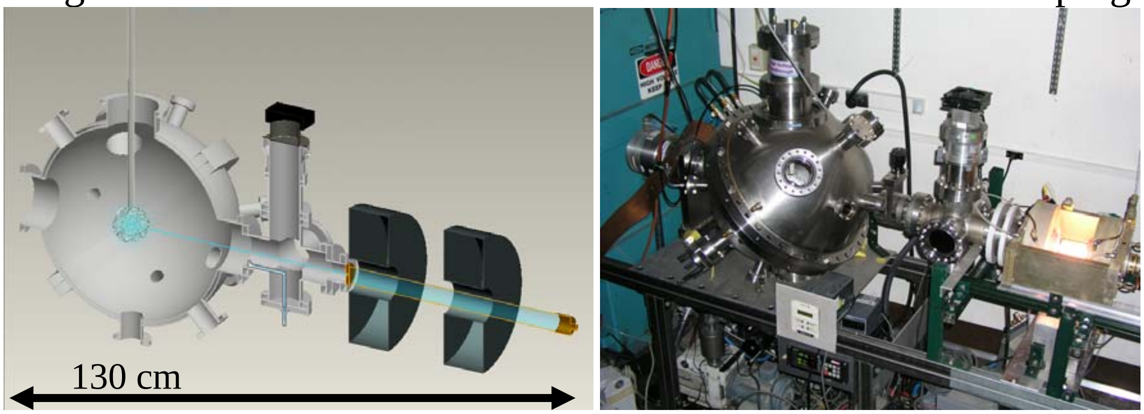

Many different geometries for the extraction electrode were tried, but all of them suffered from the same problem—the current desired for the IEC device caused too much space charge spreading of the beam. This resulted in most of the ion beam being deflected into the walls of the extraction section before it could make it to the IEC device. This limited our maximum current to only a few milliamps, and therefore the extraction system, after much effort, was removed. It may be possible for something like this to be revisited in the future, but the extraction voltage will need to be higher than that used in this system which was a maximum of about 25 kV. For this reason, the extraction system was eliminated, and the source was connected directly to the IEC vacuum vessel.

VI.F. Proton Detection System

VI.F.1 Detector Physical Setup

For these experiments two very similar detector setups were used. The first consisted of a single 700 μm thick 1200 mm^2 silicon detector which was mounted perpendicular to the primary ion beam 68 cm away from the center of the device. The second was an identical configuration, except that a 150 μm thick transmission detector was mounted in front of the thicker detector. For the single detector, a sheet of lead 225 μm thick was mounted in front of the detector to attenuate x-rays and a similar but thinner 50 μm thick Pb sheet was used in front of the dual detectors. The detector(s) were mounted on a 11.5 cm conflat flange and the distance from the chamber was provided for by a combination of flanges and tubes. There was a large horseshoe magnet (B~1 kG) about halfway between the bottom of the IEC device and the detector face which causes electrons from the device to be deflected away from the detector and into the wall of the tube. A diagram of the detector connected to the IEC is shown in figure VI-32:

Figures VI-32: Detector Assembly (Left) Mated to IEC Device (Right)

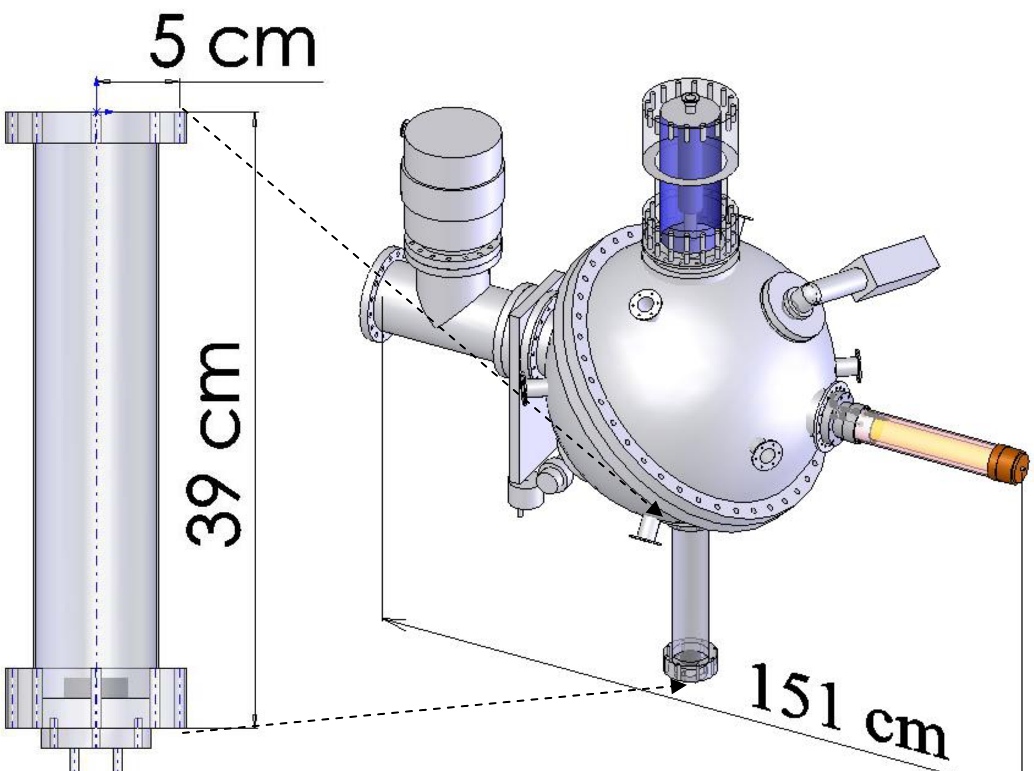

The efficiency of the single detector system can be described as:

$$\eta_{tot} = \eta_{\det} * \eta_{geom} * \eta_{foil} \qquad \text{(VI-24)}$$

Where η_{det} is the detector efficiency, η_{geom} is the geometric efficiency, and η_{foil} is the efficiency that relates to the number of protons that make it through the foil. For charged particles η_{det} is very close to 1. η_{geom} can be calculated as the ratio of the detector area to the total area of the sphere at the radius of the detector:

$$\eta_{geom} = \frac{A_{\det}}{A_{sphere}} = \frac{12cm^2}{4\pi(68)^2 cm^2} \approx \frac{1}{5000} \approx 2*10^{-4} \qquad \text{(VI-25)}$$

η_{foil} is computed using a software such as SRIM by programming the energy spectrum of the fusion protons into the code and running particles through the foil to find out what fraction will penetrate to the detector. For a 225 μm foil, this is 24.5%. Combining these results gives an overall efficiency of 1/20000 or 1 detected count for every 20000 reactions in the field of view.

For the two detector system the efficiency calculation is very similar but there is an extra term which relates to the number of protons that penetrate the detector. For the 50 μm of lead plus the 150 μm of Si, the efficiency is 55%. The overall efficiency of this system is therefore about 1/9000.

VI.F.2 Detector Electronics and Dealing with Noise

One of the big challenges of detecting ^3He-^3He reactions is that even under the best conditions the reaction rate is likely to be so low that background radiation will contribute substantially to the total number of counts measured. Another major challenge is that an IEC device generates a listening environment that is far from the best conditions. Nuclear detection systems are sensitive to very small amounts of charge and noise from ground disturbances and electro-magnetic pulses (EMPs) will appear to most of these systems as real counts. An IEC device operating at high voltage tends to have regular arcing which results in both ground disturbances and EMPs. For more typical fuel cycles (D-D, D-^{3}He) the reaction rates far exceed counts due to noise and a standard detection system is used. The first detection system used is diagrammed in figure VI-33:

Figure VI-33: First Generation Detection System

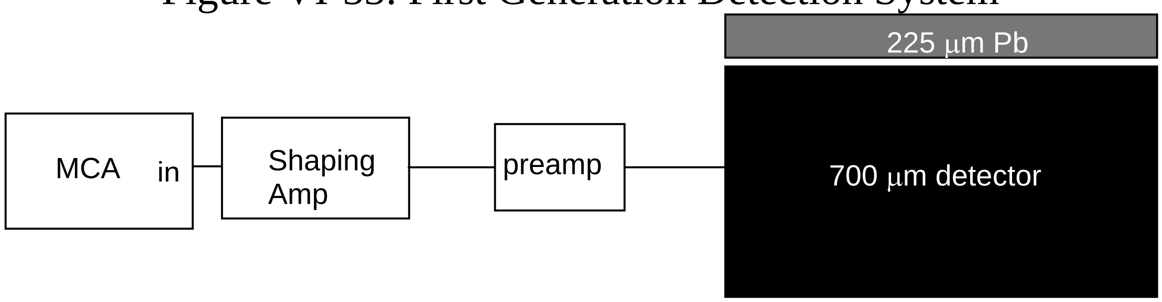

In this case a 700 μm thick 1200 mm^2 solid state detector, biased at 100 V by a Tennelec TC953 dual power supply, releases an amount of charge proportional to the energy of the protons which strike it. This charge is then converted by an Ortec model 142C preamplifier to a voltage output, then amplified and shaped by an Ortec 672 spectroscopy amp and sent to an Ortec Trump PCI Card which serves as a multi channel analyzer (MCA). The MCA tells how many events were detected and what the energy of each event was.

The largest source of broadband noise in our detection system was due to arcing and had to be dealt with if ^{3}He-^{3}He reactions were to be observed. To do this, it was necessary to disable the MCA for a short period of time before and after an arc. The first method involved listening for a pulse that would release more energy than a proton could possibly deposit in the detector, and then disabling the counting system. An Ortec 850 quad SCA was set to create an output pulse when the energy was too high, which in turn triggered an Ortec 719 counter to create a logic pulse for an adjustable time window. The 719 module was modified by adding some additional logic to make it reset its counters if two start signals came in within one count period. This was necessary since arcs often happen together and the reset time on the counter was long enough to allow some noise through during an arc cascade. Next, the detector signal was delayed on its way to the MCA or it would get counted before the gate could be generated. This delay was accomplished with two Ortec 427A delay amps which each have unity gain. After being delayed, the signal would then proceed to the MCA which would be disabled by a gate input if the electronics had detected an arc. A schematic of this system is shown in figure VI-34:

Figure VI-34: Second Generation Detection System

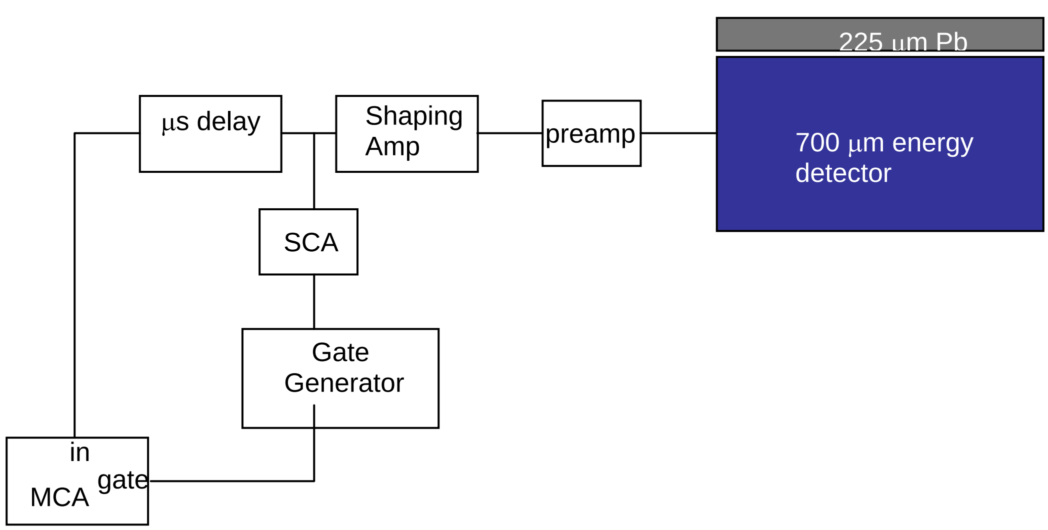

This setup did reduce the noise due to arcing by a factor of three or so, but did not decrease it far enough to achieve a good signal to noise ratio. Not all arcs generated pulses high enough to trigger the SCA, and therefore too much noise was still present. To solve this problem, a method to measure the arcs themselves was devised. A high speed voltage divider circuit was made that could measure voltage fluctuations on the cathode, since any arc will cause such a phenomenon. The divider upper resistor was 500 MΩ and the lower resistor was 5.6 kΩ, which gave a ratio of 89,600:1; therefore a 100 kV grid voltage gave a signal of about 1.12 V. This signal was then passed through a capacitive AC coupler and then to a line driver that amplified and conditioned it. The line driver also allows for the divider to be connected to a variety of different electronic equipment without fear of changing the divider ratio. From there it went to the SCA and timer circuitry to produce the gate signal. A diagram of this system is shown in figure VI-35

Figure VI-35: Third Generation Detection System

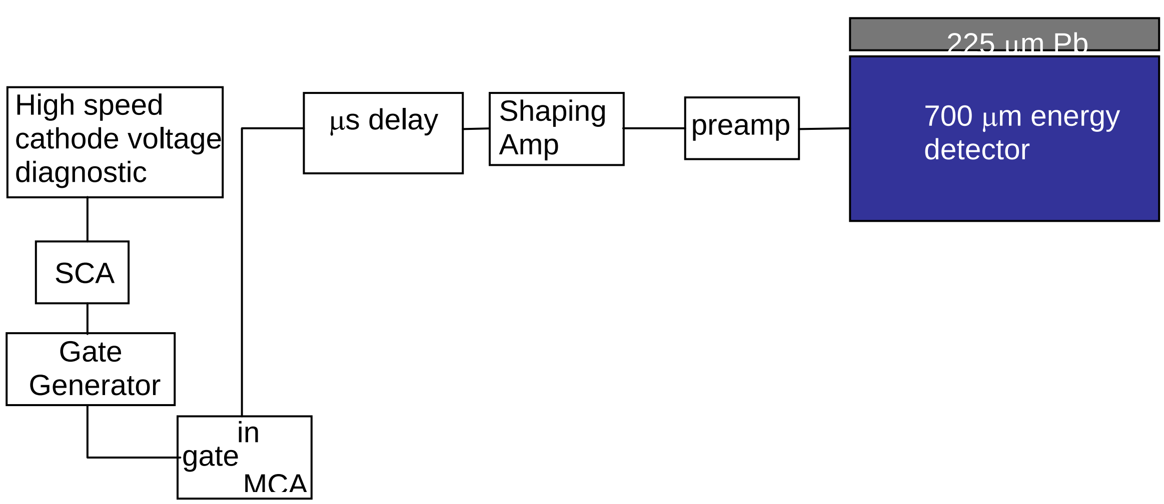

This system is only capable of removing arc noise however, and other sources of noise are still present. This means that while the noise level will drop significantly, the signal to noise ratio was still only high enough to detect ^{3}He-^{3}He fusions at voltages greater than about 130 kV, due to the higher reaction rate at that voltage. However, if measurements at lower energy are desired, the signal to noise ratio will again be low and the remaining counts will need to be eliminated or at least very much reduced. The remaining counts are believed to come from two sources: actual background radiation and pile-up radiation. The background radiation is a combination of D-^{3}He reactions, cosmic rays, naturally radioactive isotopes present in the room, and induced radioactive isotopes formed by a nearby neutron generating IEC device. Pile up radiation is due to a very high flux of x-rays. While none of the x-rays individually have enough energy to show up where they do, a combination of x-rays that strike the detector within the response time of the detection system will add together, generating this anomalously large signal. It would be beneficial to remove these additional sources of noise from the MCA as well as leaving only counts that are likely due to ^{3}He-^{3}He fusion.

For this purpose the two sources of noise were treated separately. The first source—background counts from actual radiation events can best be removed by a transmission detection system. This system incorporates a pair of detectors located on the same axis. The first detector is what is frequently referred to as a transmission or dE/dx detector which was a solid state 150μm thick and 1200mm^2 detector that is biased at 35 V. Its thickness is chosen such that a charged particle passing through it deposits only a fraction of its energy and emerges from the other side. Behind this detector is the thicker detector described above, which will stop the charged particle entirely. It will have a stronger signal and therefore be good for energy resolution. By measuring the signal from both detectors simultaneously, background radiation can be eliminated since most sources of background will not trigger both detectors at the same time. Also, D-^{3}He protons can be eliminated since they will deposit less energy in the dE/dx detector than protons from ^{3}He-^{3}He. For these experiments, the range of energies deposited in the transmission detector by ^{3}He-^{3}He protons is calculated using SRIM and is used to determine when signals in the thick detector should be counted. The layout for the fourth generation circuitry looks like the schematic in figure VI-36

Figure VI-36: Fourth Generation Detection System

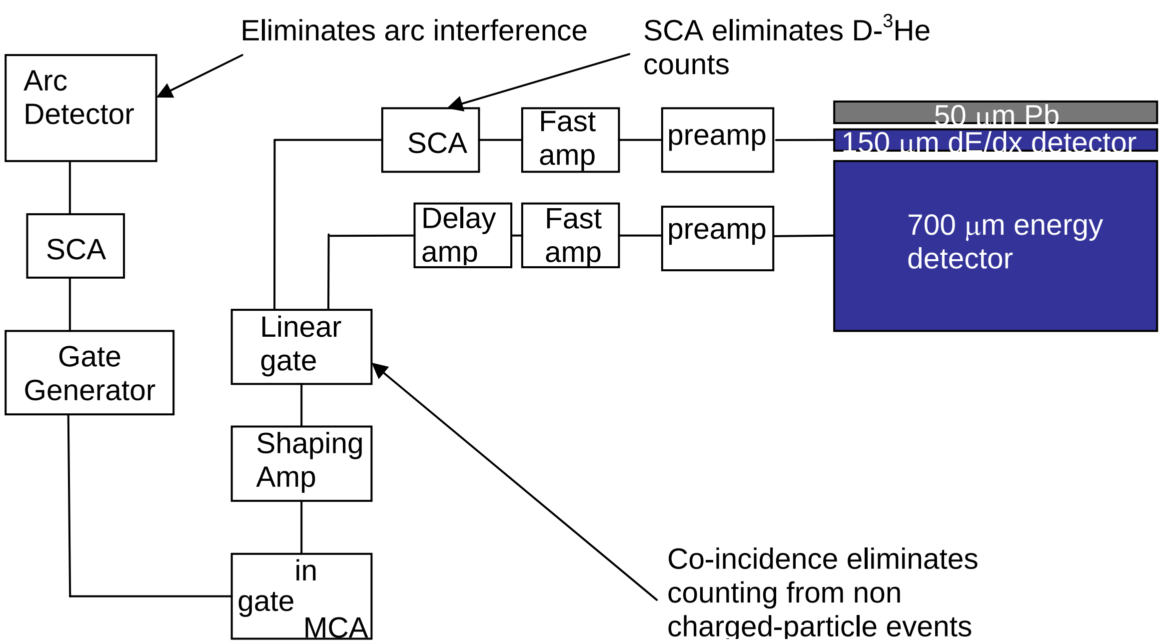

Here the same SCA as described above is set to an energy range so that only protons from ^{3}He-^{3}He will cause it to send out a pulse. This pulse then allows the Ortec

426 linear gate to pass the signal from the energy detector to the MCA. It is necessary to delay the signal from the detector slightly to allow the gate the necessary time to open. This delay is processed by an Ortec 427A delay amplifier. The gate will then close 1 μs later, which makes the probability of a background count getting through in the window caused by a ^{3}He-^{3}He proton extremely small.

The pile-up problem is caused by long integration times in the shaping amplifier and the MCA. Pile-up would also affect the transmission detector setup because it could possibly trigger the SCA on the dE/dx detector continuously. Therefore, a pair of Ortec 474 timing filter amplifiers are used instead of normal amplifiers after the dual 142C preamp stage. The integration time on these amps can be set to less than 20 ns, compared to a 500 ns minimum for the shaping amp. This discriminates x-ray signals much more effectively than the shaping amp and therefore pile-up is greatly reduced. Since the MCA will only be counting single proton events, it will appear that there is no pile-up effect at all on the data coming out even though its effect will be present. The energy resolving detector will still have a pile-up signature, but it will only be transmitted to the MCA when a proton from ^{3}He-^{3}He is detected. This means that whatever pile-up level exists in the energy resolving detector when the gate opens will be integrated with the proton energy causing a shift and spread in the proton energy signal that gets counted by the MCA. As yet, there does not appear to be an easy way around this problem other than to find a gate that can close more quickly. This would prevent many x-ray pulses that follow the proton from adding on to its signal, which would minimize the shift and smear. At the time of these experiments, the fastest gate we could find was 500 ns which will likely cause a shift of around 1 MeV and a smear of another 1 MeV.

Calibration of the timing for the two detector system is done with another IEC device that is generating D-^{3}He protons. These protons pass through the transmission detector and energy resolving detector, creating a test signal which is very similar to that from a ^{3}He-^{3}He proton. Calibration of the energy range on the detectors and their electronics is done independently with a 5.5 MeV ^{241}Am alpha particle source.

VI.G. Helicon Source Measurements Configuration

A preliminary characterization of the helicon source was done in order to provide an idea for readers what source conditions were necessary to drive the IEC device irrespective of the specific hardware used in these experiments. The IEC configuration for these measurements is irrelevant, as it would have no impact on the source properties. For the measurements in the results section, the source configuration was as described in the helicon source subsection of section VI.E. Gas flow was ^{4}He at ~ 5 SCCM. In this generation of source, there was no way to measure the source neutral gas pressure directly, but with some work it could be inferred from the physical layout and the reaction chamber pressure of 200 ± 50 μtorr to be around ~ 5 mtorr (see section V.A.).

VI.H. Ion Current Calibration Configuration

In order to calibrate the ion current from the helicon source, a material with a known secondary emission coefficient was used in place of the cathode grid. A 10 cm x

10 cm tungsten plate was polished with diamond paste and then electro-polished in a bath of NaOH. This polishing was necessary, because most published data on SEC's refer to a sample being bombarded at perpendicular incidence by an ion beam. The plate was oriented perpendicular to the ion beam, and the plate current was measured as a function of voltage for different source parameters. A picture of the plate in one of the calibration runs is shown in figure VI-37

Figure VI-37: W Plate During Source Calibration (90 kV, 20 mA)

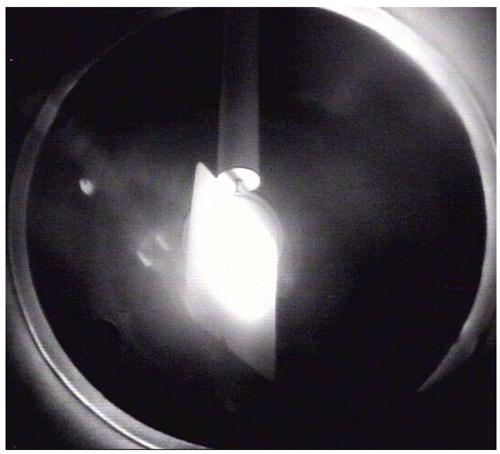

The source current is related to the current on the plate by the SEC, γ as shown in eq. VI-26:

$$I_{source} = \frac{I_{plate}}{(1+\gamma)} \qquad \text{(VI-26)}$$

The known value of γ was taken from L. Large [4], and is displayed in figure VI-38 This value was used to compute the ion source current, which is necessary to compare experiment to theory.

Figure VI-38: Secondary Emission Coefficient for He Perpendicular on Polished W

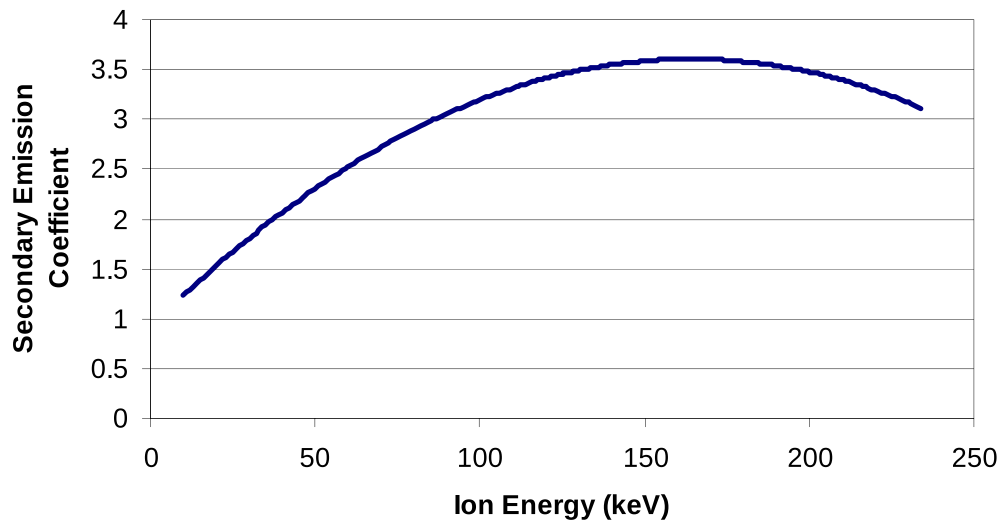

For these calibration runs, the system was operated in non-recycle mode with the device configured as described in sections VI.B, VI.C, and VI.D. ^{4}He gas was flowed in at ~ 5 standard cubic centimeters per minute (SCCM), and the reaction chamber pressure was 27 ± 7 mPa.

VI.I. ^{3}He-^{3}He IEC Configuration

The configuration used to acquire data for both ^{3}He runs and the ^{4}He runs they were compared with used a standard grid type cathode with the wires on the beam-line removed as described in section VI.D. The power supply and buffer circuit configurations were precisely those described in VI.B. and the feedthrough / stalk assembly is the same as described in VI.C. For some of the earlier runs, data was acquired with the recycle system disabled, and later with the recycle system enabled.

Operation with the recycle system enabled showed little or no difference to that with standard operation. When the recycle system was in operation, the ^{3}He or ^{4}He flow rate was zero. When the recycle system was not in operation, it was ~ 5 SCCM. In either case, the reaction chamber pressure was 27 ± 7 mPa.

While some data was taken with the fourth generation detection system, frequent unsolved problems occurred with the electrical grounds in the lab prevented any of it from being reliable enough to present in this thesis. Therefore, all of the proton detector data presented in the results chapter was taken with the 3rd generation system described in VI.E. The settings for the detection equipment are summarized in table VI-4:

Table VI-4: Summary of Detection System Settings

Hardware	Settings
Ortec 142C Preamp	Bias resistance = 9.1 MΩ, Charge sensitivity (gain) = 20 mV / MeV
Ortec 672 Spectroscopy amp	CG=100, FG=7.0, Input=norm+, shaping=Gaussian, ST=0.5 μs, PZ=Auto, BLR rate=PZ
Tennelec TC953 Power supply	V=100 V
Ortec 427A Delay amps (2)	Delay = 4.75 μs each
Ortec 850 SCA	LLD = 0.24 V, INT mode
Ortec 719 Timer (Gate generator)	Triggered by 850, Interval set to 8000, Count rate = 500 kHz
Ortec TRUMP PCI MCA	5.5 MeV=Chn. 1102, LLD set to chn. 200

VI.J. References

[1] B. B. Cipiti, “The Fusion of Advanced Fuels to Produce Medical Isotopes using Inertial Electrostatic Confinement,” PhD thesis, University of Wisconsin—Madison, (2004).

[2] A. L. Wehmeyer, “The Detection of Explosives Using an Inertial Electrostatic Confinement D-D Fusion Device,” Masters thesis, University of Wisconsin (2005).

[3] R. F. Radel, University of Wisconsin—Madison, Private Communication (2006).

[4] L. N. Large, “Secondary Electron Emission from a Clean Tungsten Surface Bombarded by Various Positive Ions,” *Proc. Phys. Soc.*, **81**, p.1101 (1963).

VII. Results

VII.A. Helicon Source Measurements

Since the helicon source used in these experiments is so compact, it was very difficult to get good measurements with probes. Nonetheless, a temporary Langmuir probe was installed by drilling through the back of the source and gluing in a probe assembly. The assembly consisted of a 2.5 mm diameter alumina rod with a 0.5 mm hole along the long axis through which a .38 mm Ta wire was fed. The wire extended 2.5 mm past the end of the alumina rod providing a surface area of 0.03 cm^2 to the plasma. The probe tip was oriented roughly parallel to the magnetic field (measurements perpendicular to the field resulted in a melted probe). A sample Langmuir probe I-V characteristic is shown in Figure VII-1. More traces, as well as a schematic of the probe setup can be found in Appendix C. These results are discussed in chapter VIII.

Figure VII-1: Langmuir Probe I-V Characteristic for Helicon Source (RF=1500 W, B=700 G)

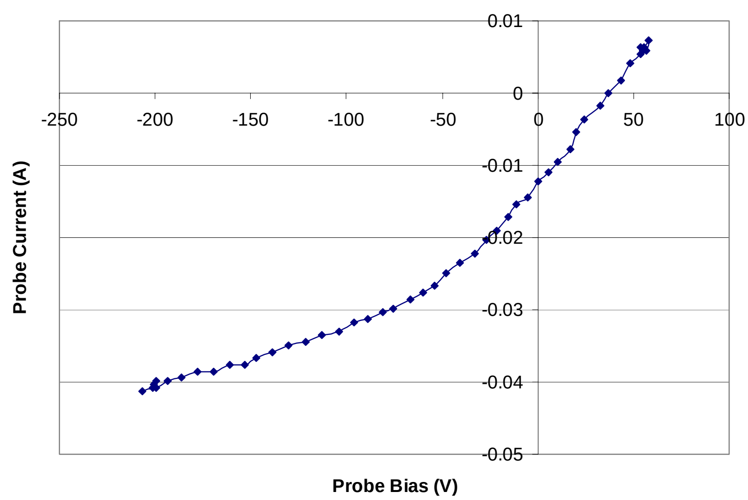

Spectroscopy was considered as a method to determine the ratio of He^+ to He^{++}, but the diagnostic available was not sensitive to the short UV bands where most of the He^{++} transitions occur. Still, a reference spectrum from typical operation is included in figure VII-2. The data was taken with a Newport Multispec spectrometer with a 400 mm^{-1} blaze diffraction grating and a 10 μm wide slit at a range of 12.5 cm from the source center. The spectrometer lens was positioned to observe the center of the RF antenna. A table of strong emission lines is included in Appendix D.

Figure VII-2: Typical Emission Spectrum from He in Helicon Source (RF=2200 W, B=1200 G)

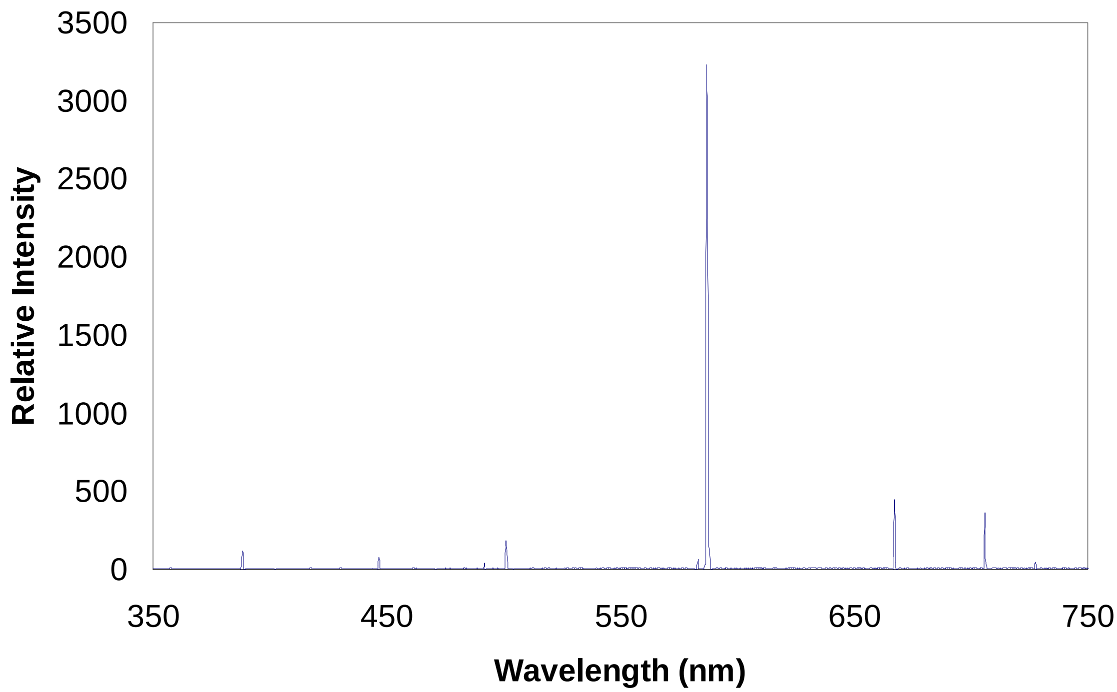

VII.B. IEC Performance Improvements

VII.B.1 Voltage

The performace of IEC devices at the UW has improved dramatically over the last several years, with major contributions coming from the work done to push the experimental parameters for the ^{3}He-^{3}He experiments. The design of a robust buffer circuit and high voltage insulators enabled reliable, long lasting runs at high voltage. A plot of the maximum achievable voltage in the UW-IEC devices versus time is shown in figure VII-3. The maximum achievable voltage at the start of this effort was about 55 kV, and the maximum achieved at the end was ~ 185 kV.

Figure VII-3: Improvements in IEC Voltage During the Present Work

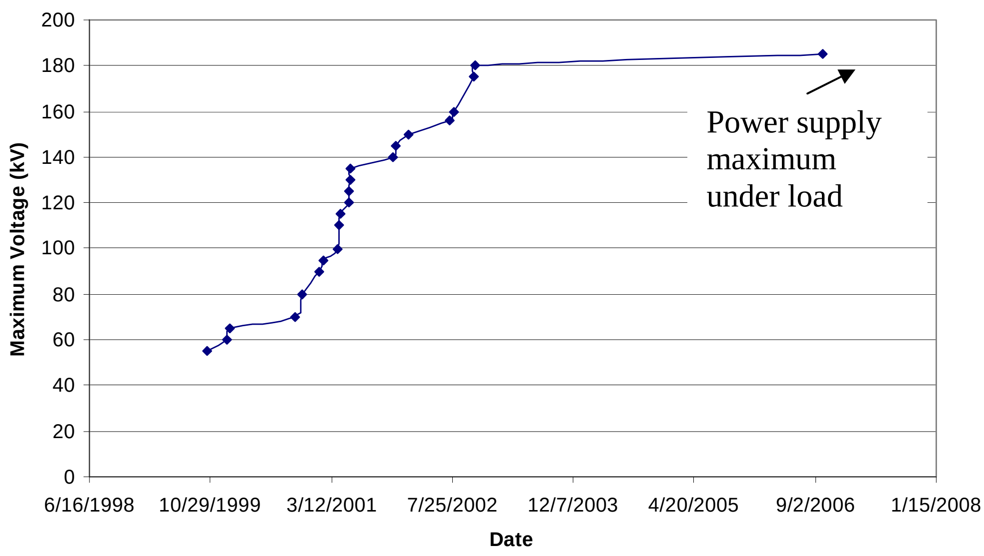

VII.B.2 Pressure

One of the other major goals of this research was to decrease the reaction chamber pressure without sacrificing cathode current in He gasses. Figure VII-4 shows the maximum current achieved versus pressure for pre- and post-ion source development. The gap between the 0.13 Pa and 0.25 Pa points on the pre-ion source curve is an extrapolation due to a lack of data and, in reality, probably has a more quickly rising slope as impact ionization and other atomic processes start to assist the discharge.

Figure VII-4: Maximum Cathode Current versus Reaction Chamber Pressure (He gas)

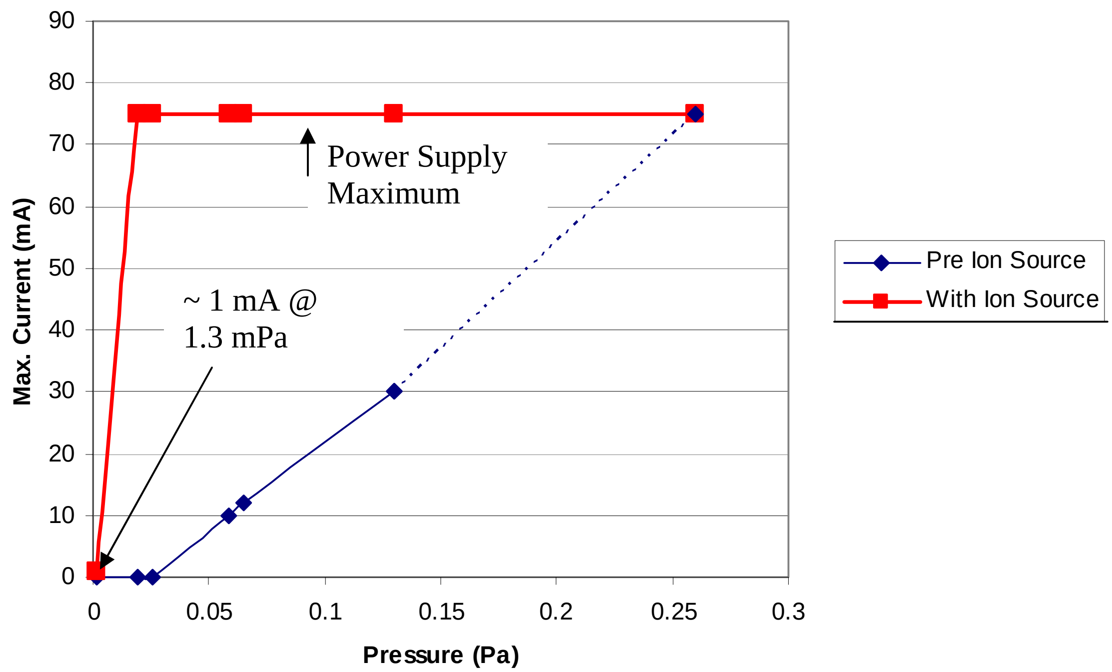

VII.B.3 Recycle System

The gas recycle system is crucial for extended run periods, and results from its operation are summarized in Figure VII-5. It can be seen that after 1 hour of operation, the impurity pressure is still a very small fraction of the He pressure. The impurity shown rising is hydrogen, which is not frozen out by the liquid nitrogen traps. The other major impurities (H_2O - 18, CO/N_2 – 28) actually decrease after 1 hour of run time.

Figures VII-5: Gas Partial Pressures (Uncorrected) in Recycle System (A: Beginning of Operation, B: After One Hour)

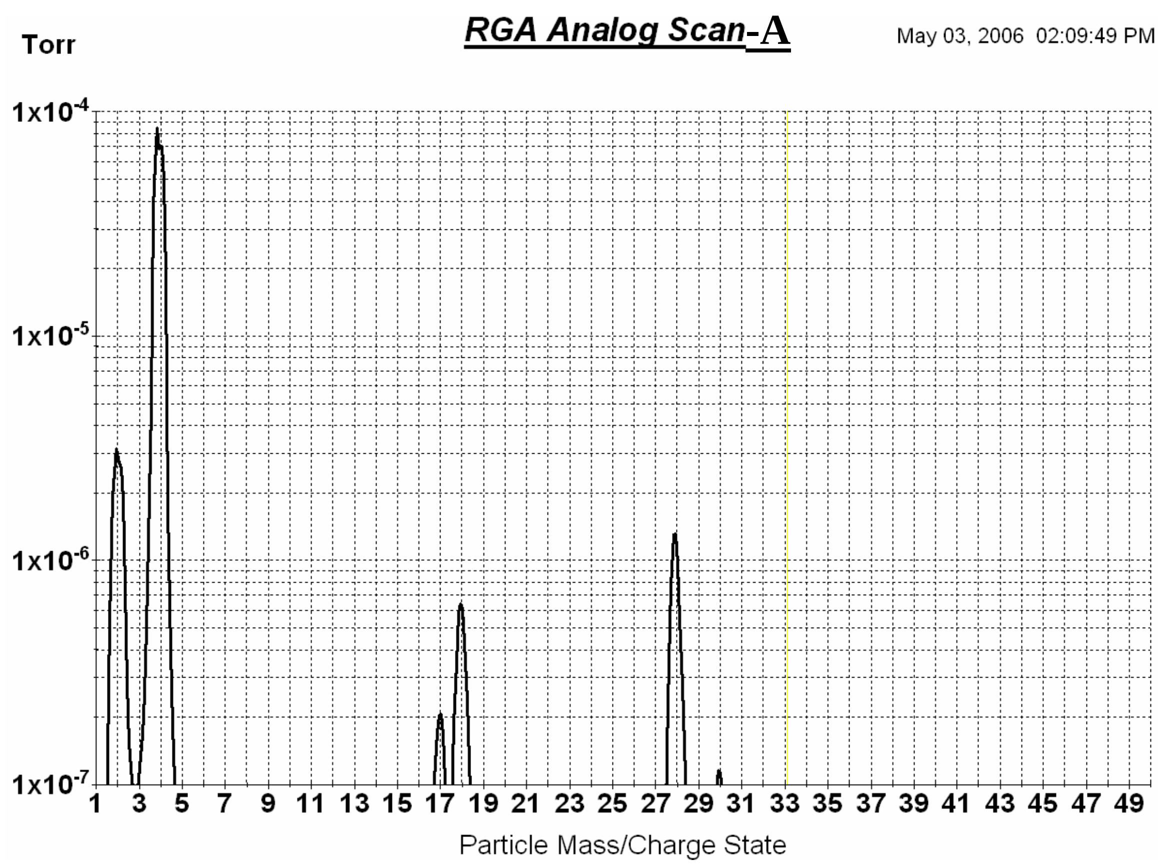

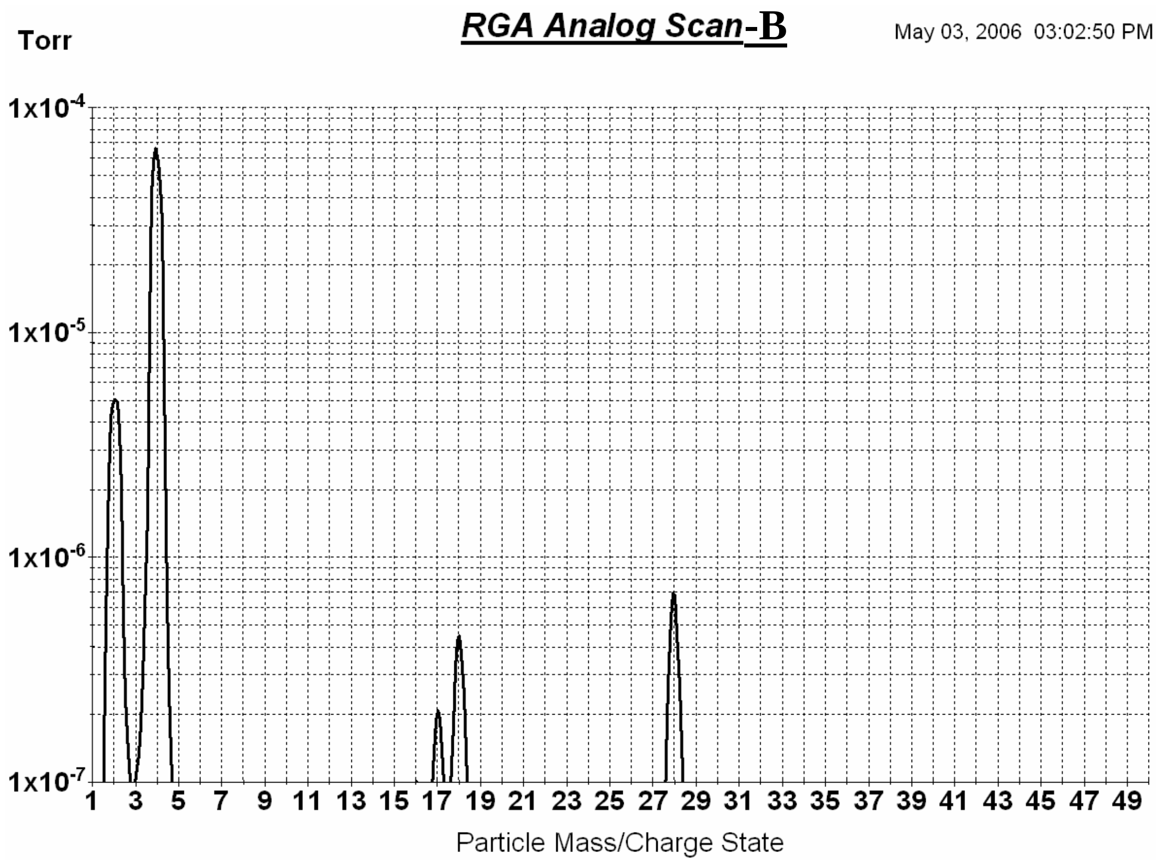

VII.B.4 Proton Detection System

Another of the major goals of this work was to remove all possible noise from the detection system. The methods to do this are detailed in section VI.F., and these efforts led to a substantial decrease in noise levels. A typical proton energy spectrum for 900 second operation at 134 kV, 25 mA in ^{4}He gas with a standard (first generation) detection system is shown in figure VII-6:

Figure VII-6: Noise Due to Arcs Generates Many Counts Before Redesign

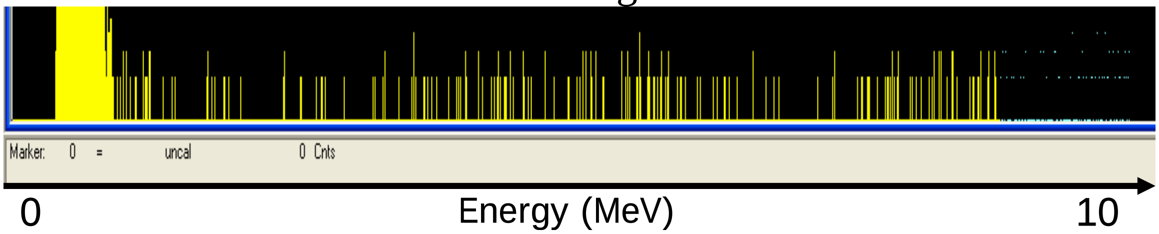

All of the counts in this spectrum are noise—none of them were generated by real protons since the only gas present in the device was ^{4}He. Of the counts in this spectrum, 95% were from high voltage arcing. To remove them, the third generation detection system was installed, and the result from a run at the same conditions as Figure VII-6 is shown in figure VII-7:

Figure VII-7: Arc Suppression Greatly Reduces Noise

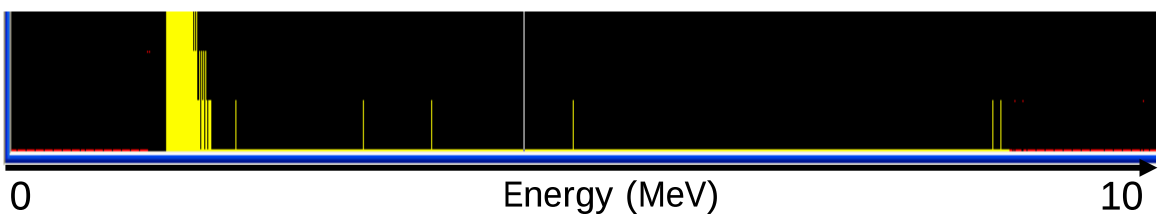

This system completely removed noise from electrical interference due to arcs, and only a few counts remained due to background radiation levels. These remaining counts were eliminated by the fourth generation circuit; however, electrical failures and grounding issues prevented data from being taken reliably with this configuration during operation. Nonetheless, even with the third generation circuit noise levels were dropped to low enough levels that the ^{3}He-^{3}He reaction was detectable, albeit only at high voltage.

VII.C IEC Operation with Ion Source

VII.C.1 Source Calibration with Tungsten Sheet

The ion source calibration was set up as discussed in section VI.H. Calibration was done at RF power levels of 1800 W and 2100 W, since these are very frequently used during operation. Furthermore, the magnetic field was swept from 700 G to 1600 G at each power level. A helicon mode was unobtainable at 1800 W 1600 G. For each value of magnetic field and power, a scan in cathode voltage was performed and the current was measured. The results of these scans are plotted in figures VII-8:

Figures VII-8: W Plate Current Increases with Plate Voltage with Incident ^{4}He Beam (A: RF=1800 W, B: RF=2100 W)

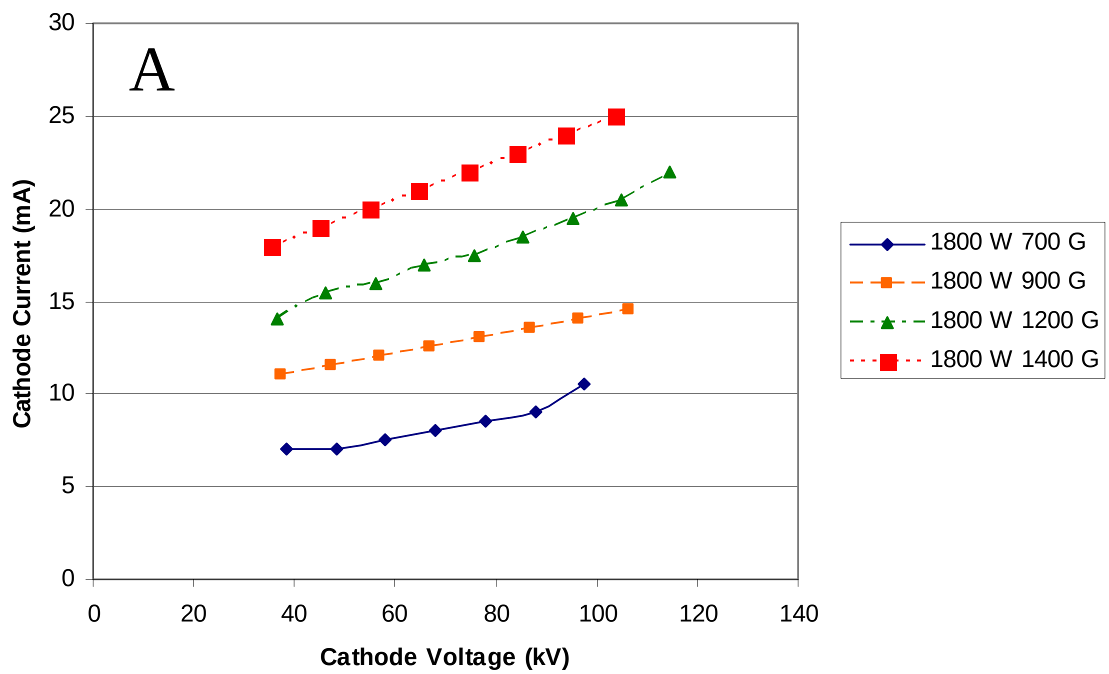

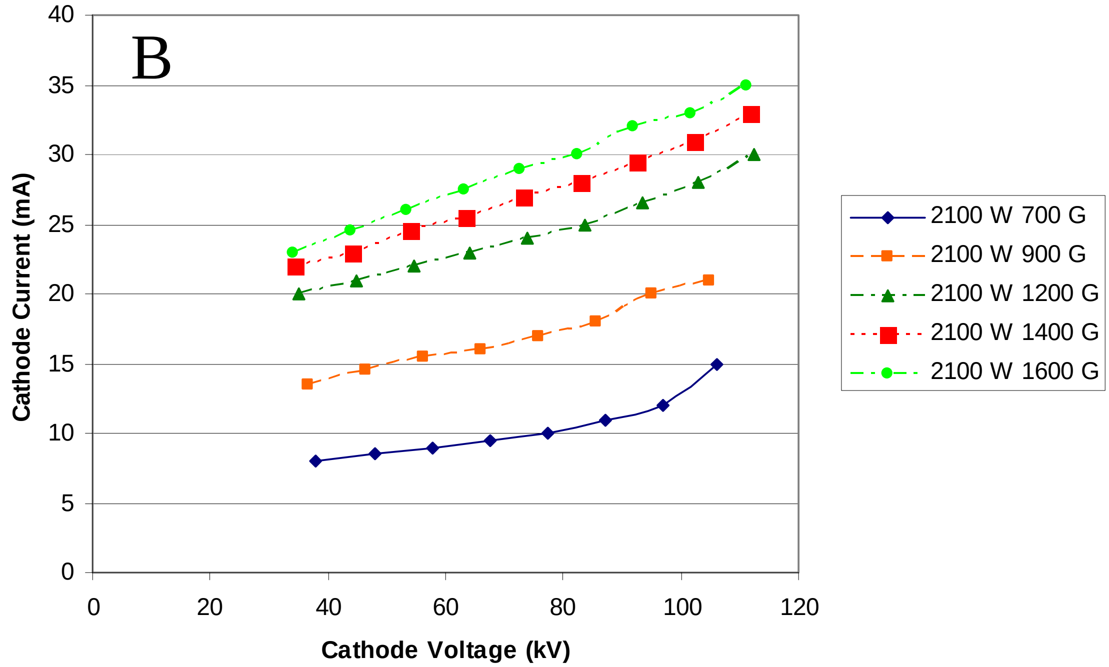

These data show that for a given set of source conditions, the cathode current increased as a function of voltage. It is important to note, however, that cathode current is plotted, not ion current, and secondary electron emission likely played a role in this increase. This is discussed in Chapter VIII. There is also a trend showing an increase in cathode current as both magnetic field and RF power increase, which is expected since either of these should increase the plasma density in the ion source.

VII.C.2 Standard Operation

In order to characterize the gridded device, scans of cathode voltage were made at fixed source conditions and the current was measured. The results of these scans are presented in figures VII-9:

Figures VII-9: Grid Current Increases with Grid Voltage with Incident ^{4}He Beam (A: RF=1800 W, B: RF=2100 W, C:RF=2400 W, D: RF=2700 W)

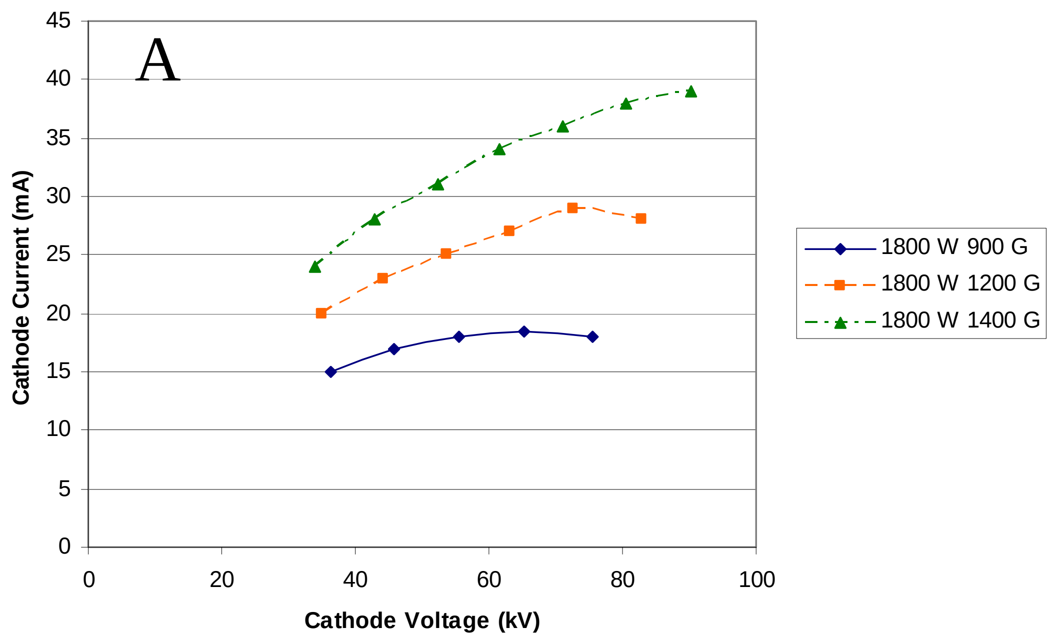

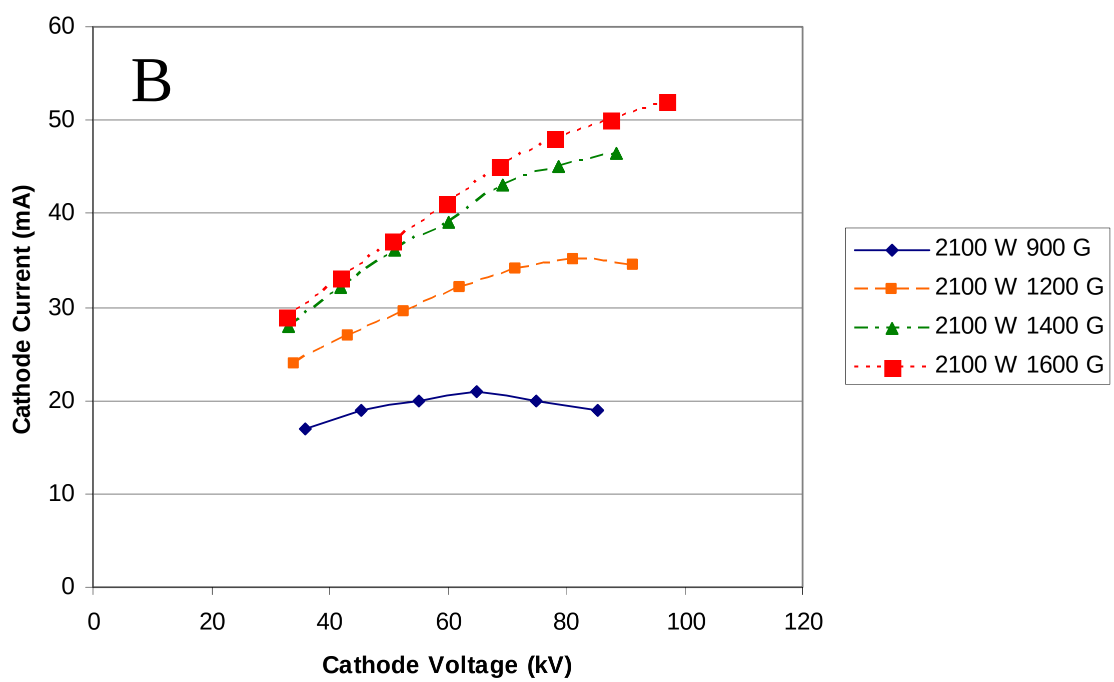

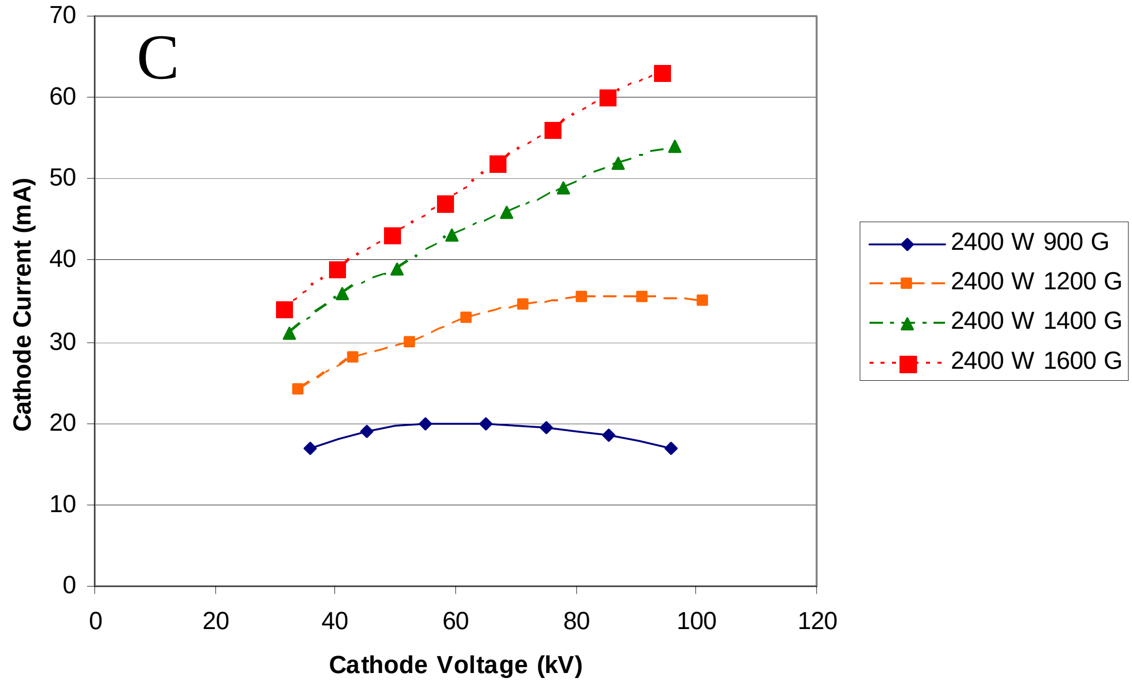

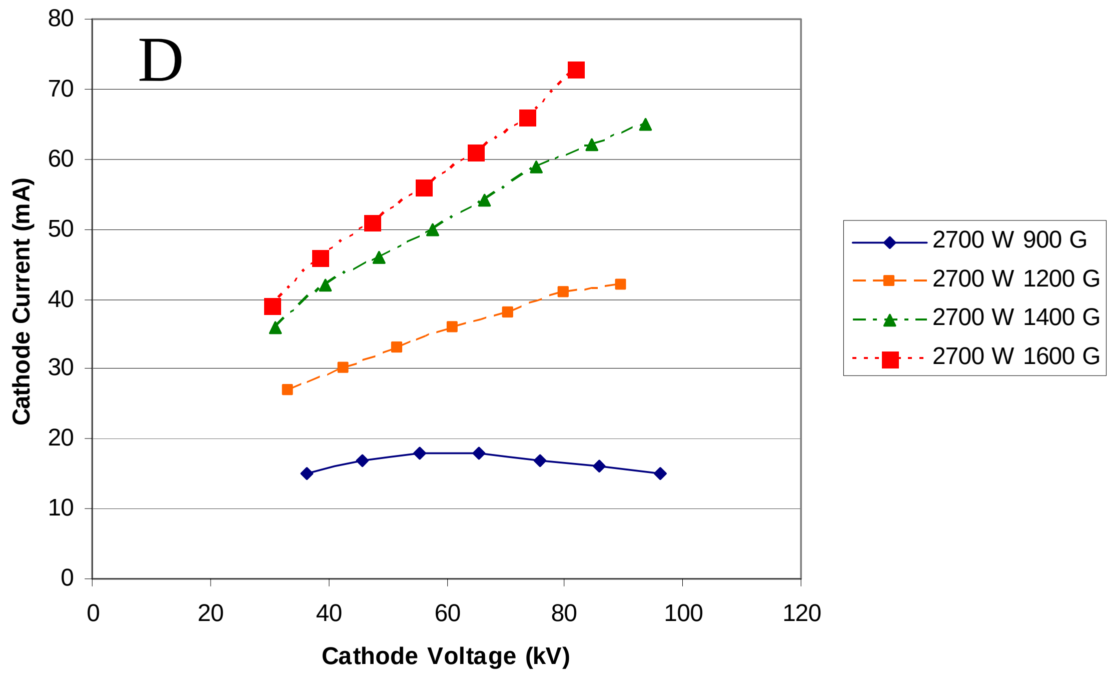

These plots show the response of the cathode current to different source settings and demonstrate the ability to run the device over the entire range of the power supply available. Going to lower currents is also possible—simply decreasing the magnetic field further will decrease the source density and therefore the current.

VII.D ^{3}He-^{3}He Results

The intent of the improvements discussed in the previous sections was to enable the IEC device to operate in a regime that would allow ^{3}He-^{3}He reactions to be observed. Hundreds of experimental runs were done to test and configure the system to this end. However, reliable data was obtained from only about a dozen runs in which the appropriate plasma conditions were reached and all of the equipment required to detect these reactions was working. For the results presented herein, the third generation detection system was used. The data sets presented in this thesis were taken for 900 seconds and runs in ^{3}He-^{3}He were either immediately preceded by or followed by identical runs in ^{4}He. This was to account for day-to-day variations in background radioactivity due to the presence of a nearby neutron generating experiment, which resides in the same shielded room as this experiment.

MCA data from one of these runs with cathode voltages of 124 kV and 134 kV are shown respectively in Figures VII-10. For these runs the reaction chamber pressure was 27 ± 7 mPa, and the cathode current was 25 mA. In this case, the 124 kV ^{4}He case was run first, immediately followed by the ^{3}He 124 kV run, then the 134 kV ^{4}He was run immediately followed by the ^{3}He 134 kV run.

Figures VII-10: Comparison of Proton Counts in ^{3}He and ^{4}He Gas from Run # 193

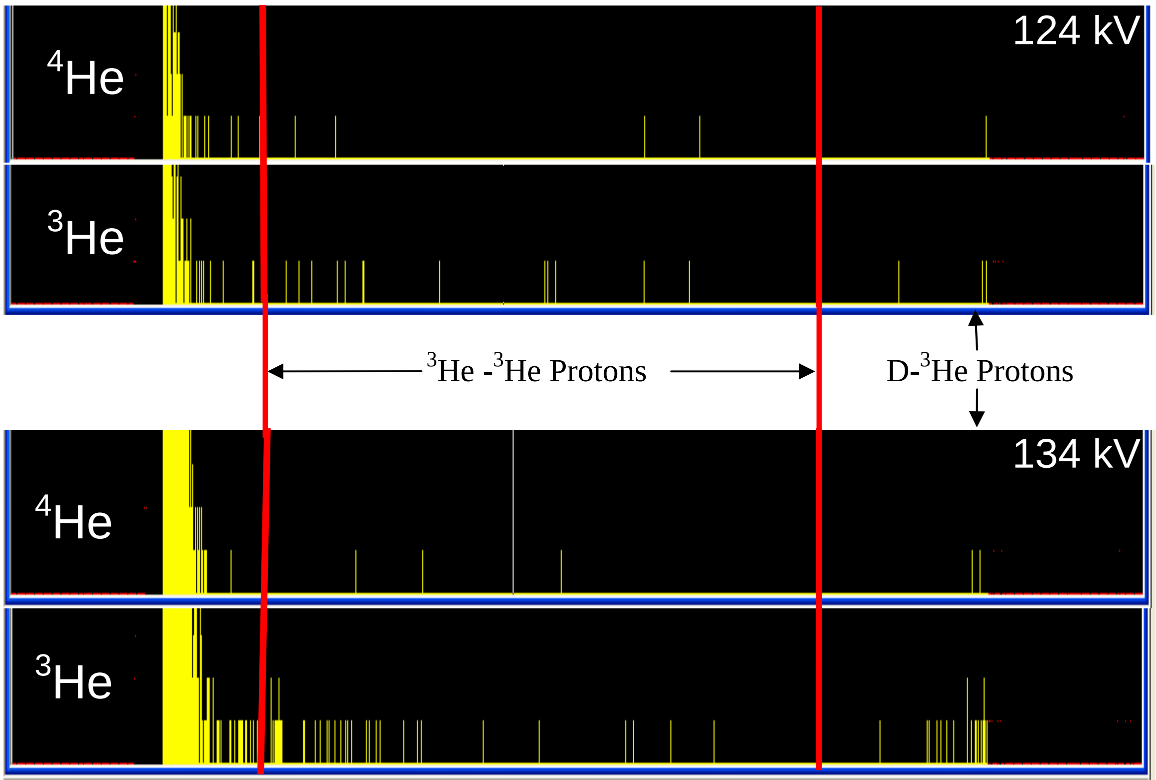

The red line on the right of these plots represents the maximum energy (7 MeV with pile-up) that can theoretically be deposited by a ^{3}He-^{3}He proton into the Si detector due to the thickness of lead present in the third generation configuration. The line on the left is intended to eliminate counting of events that could be due to pile-up, which caused the large number of counts to the left of that line. The counts to the right side of the right line were most likely caused by D-^{3}He protons. Protons from the ^{3}He-^{3}He reaction are expected to be found between the two red lines.

In four successful runs at 124 kV, the total number of counts in the ^{3}He-^{3}He energy range is 44 in 3600 seconds, and the background collected in that time was 18 counts. In three successful runs at 134 kV, the total number of counts detected was 66 counts in 2700 seconds, and the background collected was 9 counts. Using the calibration determined in section VI.F. these data indicate a ^{3}He-^{3}He reaction rate of 144 $\pm$ 44 reactions / sec at 124 kV, and 400 $\pm$ 67 reactions / sec at 134 kV.

VIII. Discussion

This section details the top level accomplishments made on IEC performance, and analyzes the data shown in Chapter VII. The details of IEC performance improvements will remain in Chapter VI, but a summary of the major features developed for this work is shown in Table VIII-1, and described in the paragraphs below:

Table VIII-1: Enhancements to IEC Operation

Feature [Section for Explanation]	**Improvement over Previous Designs**	**Relevance to IEC**
Stainless Steel Double Walled Chamber (1) [VI.A]	Better base pressure	Improved run time with recycle system
Stainless Steel Double Walled Chamber (2) [VI.A]	Water cooling—indefinite run time, previously limited to 30 mins	Allows long run times essential for ^{3}He-^{3}He runs
Stainless Steel Double Walled Chamber (3) [VI.A]	No embedded deuterium	Fewer D-^{3}He reactions and therefore less interference with ^{3}He-^{3}He measurements
Recycle System [VI.A]	^{3}He gas reused, no longer vented immediately to atmosphere	Longer run times available, lower cost run time
Buffer Circuit (1) [VI.B]	Low inductance	Transient voltage level decreased—fewer failures in HV system
Buffer Circuit (2) [VI.B]	Improved design, low field interconnects	Safer, lower explosion hazard, fewer HV failures
High Voltage Stalk / Feedthrough (1) [VI.C]	Maximum voltage increased from 55 kV to 185 kV (170 in He)	Allows higher reaction rates in all fuels
High Voltage Stalk / Feedthrough (2) [VI.C]	Improved geometry	Higher repeatability, longer lifetime

Feature [Section for Explanation]	Improvement over Previous Designs	Relevance to IEC
Cathode Grid [VI.D]	Linear geometry, along beamline	Higher transparency, lower thermionic emission
Ion Source (1) [VI.D]	External instead of internal ionization has allowed for operation at pressures ~ 50 times less than previous minimum	Higher ion energy, better known ion energy, more straightforward ion current
Ion Source (2) [VI.D]	Independent current control	Ion current straightforward, important for many IEC measurements
Ion Source (3) [VI.D]	Inductively coupled	Immune to arcs, high reliability
High Speed Voltage Diagnositc [VI.E]	Mhz measurements instead of khz measurements previously	Better diagnosis of cathode behavior, component of nuclear reaction detectors
Nuclear Reaction Detection System (1) [VI.E]	Gated system when connected to voltage diagnostic eliminates EMP interference	Reduction in noise rate by 50-100 times
Nuclear Reaction Detection System (2) [VI.E]	Transmission system, while not tested in ^{3}He should eliminate noise from background radiation	Should allow for ^{3}He-^{3}He cross-section measurements at lower energy

VIII.A. Helicon Source Results

The helicon source developed for these experiments is almost certainly the first of its kind to operate with ^{3}He gas. It has the highest power density of any source known to this author for its size and allows for operation of IEC devices in a unique parameter space. When this research began, the maximum ^{4}He current available from a commercial source at the neutral flow rate required was < 1 mA, which this device surpasses by an order of magnitude. Table VIII-2 summarizes some of the important properties of this source:

Table VIII-2: Summary of Helicon Source Properties

Source diameter	5 cm
Source length	44 cm
Plasma length	20 cm
Vacuum chamber	4 mm thick quartz tubing, steel / brass ends both water cooled
Antenna type	Nagoya III, water cooled
Matching circuit	L-type, water cooled
Maximum RF power input	3500 W
Magnetic field	Electromagnets, water cooled, 0-2 kG
Electron temperature	5 eV*
Maximum density (He^+)	10^{19} m^{-3}*
Maximum theoretical current (He^+, through 0.6 cm^2 hole at 10^{19} / m^3)	600 mA
Maximum extracted ion current (He^+)	12 mA
Duty cycle	Continuous

*Order of magnitude estimate based on similar sources, see discussion below

To determine the source parameters, Langmuir probe measurements were attempted at the power levels used for IEC operation, but even before the probe could be connected to any measurement circuit the Ta wire and alumina would melt. While a fair amount of data was collected with a Langmuir probe at lower source power levels, the data was quite confusing since it included a positive floating potential-an unusual result in probe measurements of cold plasmas. This likely was due to the long axis of the probe being aligned with the magnetic field of the helicon source. This alignment reduced electron collection along the axis of the probe, as the small electron gyroradius reduces the electron collection area compared to the ion collection area. As a result, deduction of parameters such as electron temperature became very difficult. Furthermore, the ion gyroradius was on the order of the probe diameter, which meant the ion collection area varied with magnetic field in a complicated fashion. Therefore, the electron temperature and density could not be well determined. There are similar sources, such as the mini RFTF at Oak Ridge National Laboratory [1] that have made Langmuir probe measurements at power levels similar to those used in this source and indicated densities of up to 10^{19} m^{-3} with electron temperatures around 5 eV. Since their probes survived and ours melted, it is possible the density in this source was even higher, but the density inferred above should only be considered as an order of magnitude estimate.

VIII.B. IEC Performance

Great strides were made in IEC performance as a result of this work. The goals for maximum voltage, minimum pressure, and ^{3}He conservation have been met or exceeded. The goal of eliminating noise in the proton detection system was largely met, in that a reduction in noise level of 50-100 times occurred. A summary of progress in each of these areas follows.

VIII.B.1 Voltage

At the beginning of this work, the maximum voltage achievable in the UW IEC device was about 55 kV. Operation in the early days of the Wisconsin IEC chamber was unstable and frequently destroyed the insulator materials used in the stalk assemblies. After tremendous time and effort, the maximum operating cathode voltage was increased to 185 kV (170 kV in He), and the reliability of insulators is such that the most recent family has survived over 6 months under very harsh operating conditions. Repeatable, reliable (minutes at a time) operation can now be achieved at 170 kV (maximum for the current high voltage power supply in its present configuration) in D_2 gas and 130 kV in ^{4}He and ^{3}He. These improvements have allowed for the detection of ^{3}He-^{3}He reactions, and have pushed IEC technology rapidly into the near-term application market by being a major factor in a 20 fold increase in the D-D neutron rate from $1 * 10^7$ neutrons / s to $2 * 10^8$ and a 10,000 fold increase in the D-^{3}He proton rate from 10^4 protons / s to 10^8. Further improvements in maximum voltage in D_2 will come from improving power supplies and circuitry, while further improvements ^{3}He gasses is more likely to come from materials that are more resistant to damage from He bombardment.

VIII.B.2 Ion Source

The development of this ion source has allowed for independent control over the device ion current, in contrast to the highly dependant relationship between IEC parameters and ion current that existed previously. This independent control simplifies calculations to relate measured reaction rates to theoretical ones.

Additionally, this ion source has allowed for IEC operation at lower pressure and higher current than was previously possible. The previous minimum operating pressure in He gas was 0.06 Pa at a cathode current of 10 mA. The new minimum operating pressure with a high current is 0.02 Pa, where the cathode current was 75 mA, and could have been higher if a larger power supply were available. Even lower pressure operation has occurred at pressures as low as 0.001 Pa at a cathode current of 1 mA-a regime in which no previous IEC devices had operated. These accomplishments are important for the study of ^{3}He-^{3}He reactions because they result in ion energies that are unaffected by atomic processes. Therefore, higher reaction rates can be achieved and more straightforward reaction rate calculations can be done; important capabilities when trying to measure cross sections. For the future, this technology may be adaptable to the end of operating a low pressure IEC device suitable for studying converged core reactions.

VIII.B.3 ^{3}He Conservation

One of the goals of this thesis was to measure ^{3}He cross sections at low energy. In order to do this, very long run times were needed and at an average cost of $60 / hour (mainly due to ^{3}He consumption), expenses were quite high for a university experiment. Therefore, a recycle system was designed to decrease this cost. While issues with the detection system prevented very long run times for this thesis, the recycle system was completed and tested in ^{4}He gas. It demonstrated the ability to run the IEC device on just a few minutes of initial flow for over an hour with minimal impurity buildup. It is quite likely this system could go much longer without additional He if the traps had a continuous flow of liquid nitrogen, a substance that is much cheaper than ^{3}He. So far, use of the recycle system has demonstrated a reduction of the amount of ^{3}He required by a factor of 10, and would likely reduce it much further if longer runs were done.

VIII.B.4 Proton Detection System

A tremendous amount of work went into trying to create a detection system that would statistically eliminate essentially all sources of noise in the proton counting system. While this effort was not fully completed, a factor of 50-100 noise reduction was accomplished. This development allowed for the detection of ^{3}He-^{3}He protons at high cathode voltages (~130 kV), even though the low voltage reaction rates cannot be reliably measured until the remaining noise is eliminated. A system to meet the goal of complete elimination has been designed and calibrated with D-^{3}He protons. This system was successful in eliminating all background radiation from a sample with no IEC operation, but due to unresolved grounding issues and other sources of noise, it was never used with ^{3}He gas.

VIII.C. Ion Source Calibration

The experiments done with the flat W plate described in chapter VII were designed to determine the ion current supplied by the ion source under various conditions. The ion source current can be calculated by the relation (Eq. VI-26):

$$I_{source} = \frac{I_{plate}}{(1+\gamma)}$$

Where γ for the plate is shown in figure VI-38. Correcting the values measured in Section VII.C. with a fit to the data presented in Chapter VI-38 gives the result shown in figures VIII-1:

Figures VIII-1: He Ion Source Current Output Flat with Voltage

(A: RF=1800 W, B: RF=2100 W)

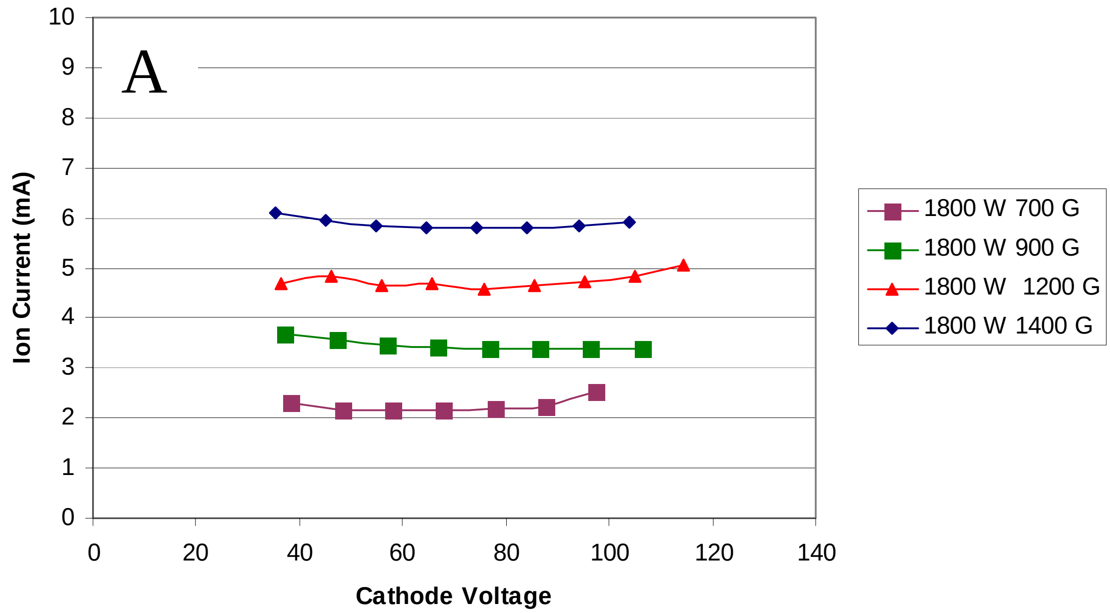

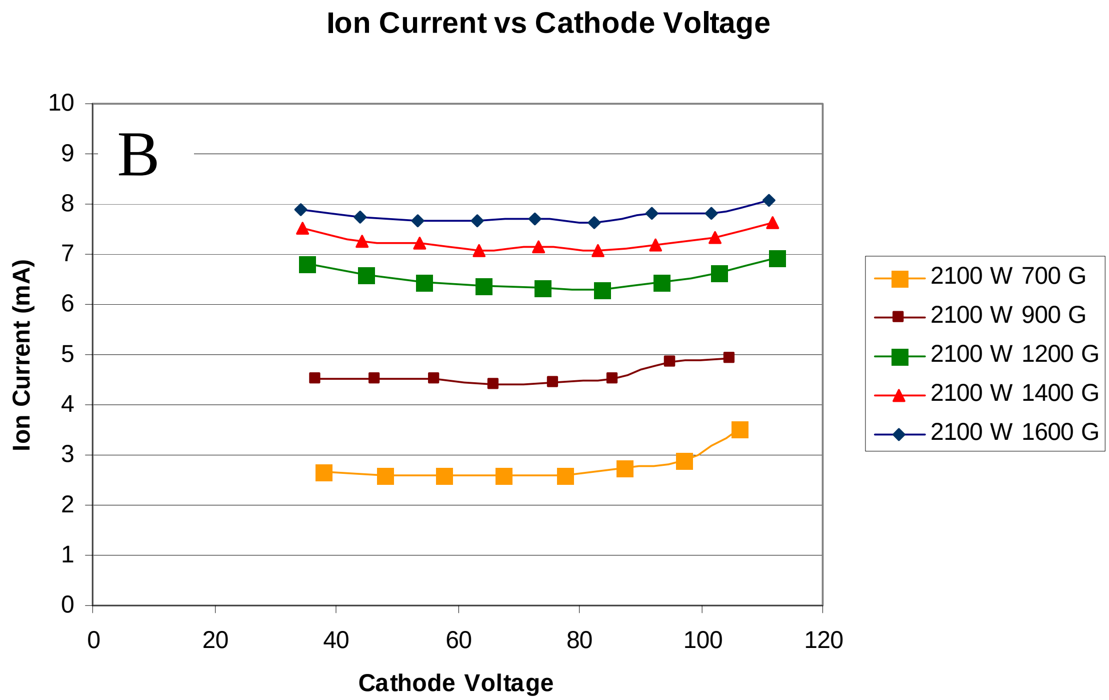

These figures show that the ion current from the source remained relatively constant with cathode voltage. This result is useful, as it gives a way to predict ion currents in the device based only on source parameters. Since the ion current mainly determines the fusion rate at a constant voltage, this is the figure of merit that should be used when comparing one set of IEC operating conditions to another. If an ion source such as this is used, the cathode current is no longer relevant to the fusion rate, but only the source conditions and the cathode voltage.

The technique of correcting the cathode current with known secondary emission coefficients is not applicable to more complicated geometries. An IEC device operating with a grid has ions impacting at a wide range of angles on its wires, with a distribution that is very difficult to characterize. Since angle of incidence plays a major role in secondary emission, there is no easy way to convert from cathode current to ion current, unless the ion current has already been characterized. An analysis of the effective secondary emission coefficient of the cathode grid used in these experiements will be done in section VIII.D.

The magnitude of the current produced by the ion source is also of interest. According to estimates of the plasma density inside the source, the maximum ion current extracted should be on the order of 600 mA (see eq. V-6) or more whereas only 12 mA has been measured. There are two phenomena occurring near the beam aperture of the helicon source that could account for this discrepancy, both of which involve the magnetic field required to create the discharge. The first is that the magnitude of the magnetic field is decreasing rapidly near the aperture. It is quite likely that the plasma density very near this exit is quite a bit lower than that measured in the bulk of the source. The second is that the direction of the magnetic field is reversing direction in the same location. This turn-around of the field lines is likely to steer a majority of the extracted ions back into the walls of the source. Either or both of these effects could severely reduce the maximum current extracted.

VIII.D. Effective Secondary Emission Coefficient

Since the true ion current into the ion source has now been determined as a function of source parameters alone, there is no need to try to determine the effective secondary emission coefficient (SEC) from the cathode grid. Still, as a matter of interest to IEC devices that do not have the ability to characterize ion current directly, it is useful to quantify the SEC from this configuration to give a better understanding of how other devices might operate. Using the known ion current and the cathode current, the secondary emission coefficient for the grid used herein can be calculated by rearranging Eq. VI-26:

$$\gamma = \frac{I_{cathode}}{I_{source}} - 1$$

Using the data in section VII.C. for the standard cathode operation gives the effective secondary emission curves shown in figures VIII-2:

Figures VIII-2: Grid Effective Secondary Emission Coefficient Higher than for Flat Incidence with ^{4}He Beam

(A: 1800 W, B: 2100 W)

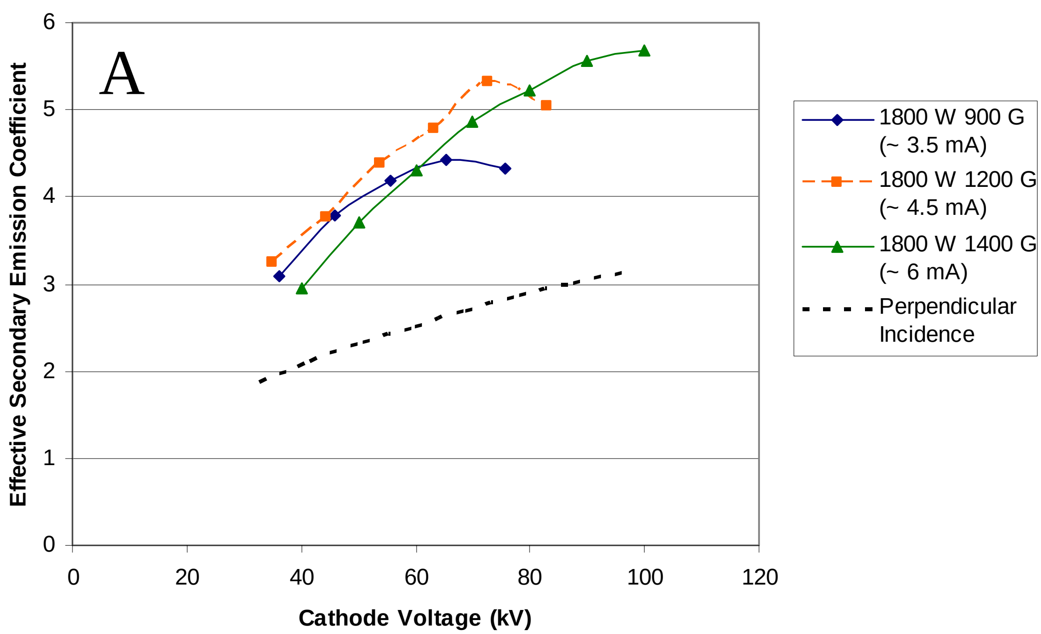

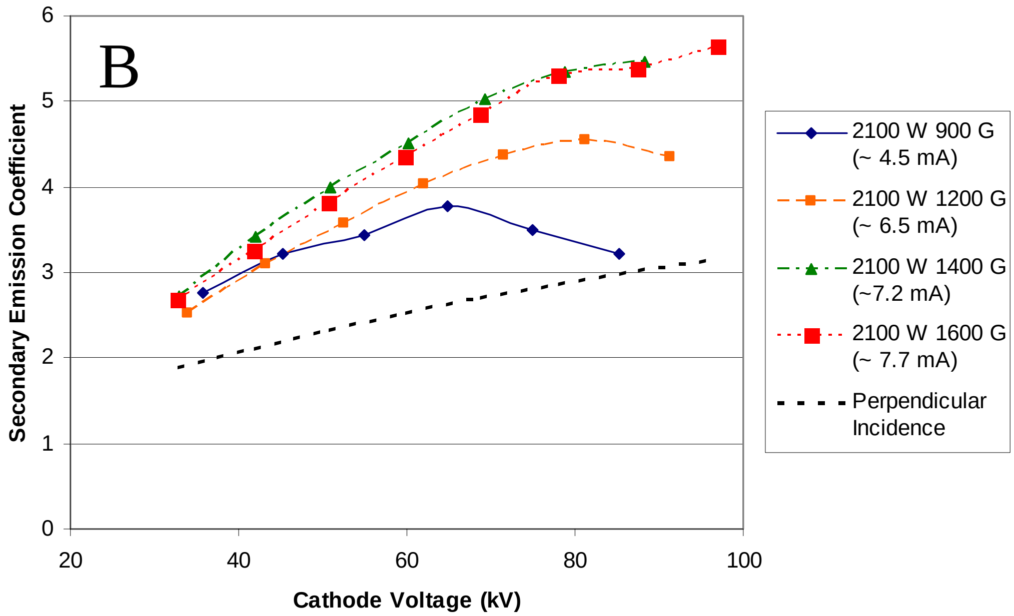

These curves show that the effective SEC from the grid is higher than that for He ions hitting perpendicular to the flat plate. This is expected, because SECs are dependant on angle and increase as ion impacts become more glancing. It is also worth noting that the SEC for the grids sometimes rolls over faster than that for the plate, which could indicate a changing angular distribution of the ions into the grid as cathode voltage increases. Furthermore, changing ion currents seem to affect this distribution as well. These results are not a surprise, but the behavior is rather complex.

VIII.E. ^{3}He-^{3}He Reaction Rate Analysis

Thus far measurements of reaction rate in IEC devices have been characterized primarily by cathode voltage and cathode current. Since the source current is known in these experiments, the metric of cathode current will be replaced by that of source current. For the results shown in section VII.D., this means the source current was 7 ± 1 mA based on the source conditions. Subtracting the background from the number of counts detected at 124 kV, then adding the errors in quadrature gives a detected rate of 26 ± 8 counts in 3600 seconds. Repeating this process for the 134 kV measurement gives 54 ± 9 counts. The actual reaction rate is obtained by multiplying this rate by 20,000; the detector calibration factor determined in section VI.F. For the 124 kV case, the reaction rate measured was 144 ± 44 reactions / sec, and at 134 kV, it was 400 ± 67 reactions /sec.

The theoretical reaction rate for these conditions can be calculated using the techniques described in chapter IV. The expected beam-background rate is calculated using equation IV-16:

$$R_{bb} = n_b \frac{I}{e} \sigma(E) l$$

But since I is the total ion current, it must be expressed in terms of the source current. The source current and the total ion current are related by the grid transparency η through equation VIII-1:

$$I = \frac{I_{source}}{\left(1-\eta^2\right)} \qquad \text{(VIII-1)}$$

Taking I_{source} = 0.007 ± 15% A, η = 0.95, n_b(@27 mPa) = 6.6 * 10^{18} ± 25% m^{-3}, σ(124 keV) = 2.8 * 10^{-35} m^2, and l = 0.20 m, the expected beam-background rate at 124 kV is 16 ± 5 reactions / sec. At 134 keV, the calculation is the same, except that σ(134keV) = 5.3 * 10^{-35} m^2, which gives a predicted beam-background rate of 31 ± 9 reactions / sec. The cross section is taken from figure IV-3, and its error is neglected, since the cross section here is poorly defined.

The embedded fusion rate is calculated using the source current only, since the current impacting the cathode is going to equal the current generated by the source since atomic processes are not expected to be significant. The embedded fusion rate is described by equation IV-17:

$$R_{emb} = \int_0^{r_{final}} I_{source} n_{emb} \sigma(r) dr$$

The embedded density, as described in chapter IV is likely to be about 3.5 * 10^{27} particles / m^3 based on previous work by Cipiti [2]. This density gives an expected fusion rate at 124 keV of 198 ± 30 reactions / sec [5], and 413 ± 60 reactions / sec [6] at 134 keV. Again, the cross section error is not accounted for due to the possibility for large variation.

When relating the embedded fusion rate to the detected count rate, there is an additional factor of two that needs to be taken into consideration because roughly half of the detectable particles produced will head into the grid wires instead of out of them. This means that the predicted embedded rates above would look like half that reactivity to the proton detector. These reactions will be called the detectable beam-embedded fusions and would have reactivity 99 ± 17 reactions / sec (124 kV) and 206 ± 33 reactions / sec (134 kV) for Cipiti's density.

The sum of the above numbers and the expected beam-background rate should give numbers that are directly comparable with measurements of the reaction rate made by the proton detector. For this case, the total expected rate is 16 ± 5 (beam-background) + 99 ± 17 (beam-embedded) =115 ± 18 reactions / sec at 124 kV, and 237 ± 34 reactions / sec at 134 kV. These results are within 50% of the detected rate, and this difference could be due to phenomenon such as the presence of a small amount, on the order of 0.2%, of He^{++} in the helicon source or enhanced cathode transparency due to ion channeling. Table VIII-3 summarizes the comparison between actual and predicted reaction rate:

Table VIII-3: Summary of Measured ^{3}He-^{3}He Reaction Rates

Voltage	**Theoretical Beam-Background Rate (reactions / sec)**	**Theoretical Detecteable Embedded Rate (reactions / sec)**	**Measured Rate (reactions / sec)**
124 kV	16 ± 5	99 ± 17	144 ± 44 (ave)
134 kV	31 ± 9	206 ± 33	400 ± 67 (ave)
134 kV	31 ± 9	206 ± 33	600 ± 89 (max)

The measured rate is not identical to the actual reaction rate, since fusions due to embedded reactions emit half of their protons back into the grid wires. Therefore, the detected rate from embedded fusion should be doubled in order to give a total reaction rate. If the theoretical prediction for the number of embedded reactions compared to beam-background reactions from chapter IV is correct, then the total rate can be calculated by multiplying the suspected embedded fusion rate by two. Table VIII-4 summarizes these results:

Table VIII-4: Summary of Total ^3He-^3He Reaction Rates

Voltage	Theoretical % of Reactions from Embedded Fusion	Measured Rate (reactions / sec)	Inferred Total Fusion Rate
124 kV	86%	144 ± 44 (ave)	268 ± 76 (ave)
134 kV	87%	400 ± 67 (ave)	748 ± 117 (ave)
134 kV	87%	600 ± 89 (max)	1122 ± 155 (max)

VIII.F Summary

This work represents a tremendous increase in IEC capability, which has led to the observation of ^3He-^3He reactions in an IEC device for the first time. The average rate of reactions measured at 134 kV was 400 ± 67 reactions / second and at 124 kV was 144 ± 44 reactions / sec. The agreement with the theoretical rate based on past experimental measurements of He density is an encouraging one, since it is further validation that ^3He-^3He reactions were actually observed. On the other hand, since many of the reactions detected are likely due to embedded fusion, the usefulness of this configuration to measure cross section detail is quite limited. While the embedded rate is expected to dominate the detectable counts for this configuration, it is worth noting that the expected number of beam-background counts at about 10-15% of the detected count rate. If a configuration that removed the cathode grid from the field of view of the detector was designed, and the fourth generation counting system made operational, this would be a detectable count rate that would be useful for measuring the ^3He-^3He reaction cross section. Such an effort will likely take some time but be a valuable contribution to the nuclear physics database.

VIII.F. References

[1] M.D. Carter, et al, “Comparing Experiments with Modeling for Light Ion Helicon Plasma Source,” *Physics of Plasmas,* **9**, [12], p.5097 (Dec. 2002).

[2] B. B. Cipiti, “The Fusion of Advanced Fuels to Produce Medical Isotopes Using Inertial Electrostatic Confinement,” PhD thesis, University of Wisconsin—Madison (2004).

[3] See Appendix A for calculation

[4] See Appendix A for calculation

IX. Conclusions

The objective of this work was to develop IEC technology to the point that it would be sufficient for studying ^{3}He-^{3}He reactions. The requirements to meet this objective and the related accomplishments are listed below:

- Develop a method to increase IEC voltage performance
    - New power supply capable of higher voltage obtained (200 kV)
    - Buffer circuit designed to stabilize operation
    - Insulator strength dramatically improved by changing material to BN (maximum voltage increased from 55kV to 185 kV)
- Develop a method to increase reliability of high voltage system
    - Buffer circuit design features included minimum inductance, low field interconnects
    - Improvement of stalk insulator and conductor geometry (lifetime improved from about 1 month to about 6 months)
- Develop a method to operate for extended time periods in ^{3}He gas
    - New vacuum chamber designed and acquired that incorporates water cooling with a double-wall system
    - Gas recycle system developed to reuse helium gas after it flows through the system (He usage decreased by 20 times)
- Develop a method to operate at lower pressure without sacrificing cathode current

  - Helicon ion source developed which can generate maximum 75 mA cathode current (max allowable by power supply), at pressures as low as 27 mPa, comparte to previous best 10 mA at 60 mPa
- Develop a method to gain independent control over ion current
  - Helicon ion source developed which provides source current independent of cathode voltage and reaction chamber pressure (0-12 mA ion current)
- Develop a method to reduce detection system noise
  - Arc detection system developed which completely eliminates noise due to electromagnetic pulses (factor of 50 to 100 reduction in overall noise level)
  - Transmission detection system designed which should almost completely eliminate noise due to background radioactivity
- **Observe ^{3}He-^{3}He reactions in an IEC device**
  - Average detectable reaction rate of 400 ± 67 reactions / sec (600 ± 89 reactions / sec peak) measured for the first time in such a device
  - Total average ^{3}He-^{3}He reactivity of 748 ± 117 reactions / sec (1122 ± 155 reactions / sec peak)

Thus the overall goal of this work was accomplished, with major efforts in a number of areas. These improvements have also played a significant role in the advancement of IEC technology for use in other areas such as:

- Enhanced understanding of secondary emission
- Special nuclear material detection
- Explosives detection
- Medical isotope generation
- Materials irradiation studies

This work represents seven years of engineering and development, and has pushed some very strong operational boundaries outward. It has paved the way for the IEC device to be used as a tool for detailed studies of the ^{3}He-^{3}He cross section, and founded technologies that will be useful to IEC research and development many near term applications.

X. Future Work

A great deal of work was done to develop IEC capabilities for this thesis and now there is a whole new operational area to explore. Some of these areas are of clear interest at the present time, and others will come into view as more research is done. Some of the more obvious areas of interest as a result of these new capabilities are listed below.

X.A Measurements of the ^{3}He-^{3}He Cross Section

IEC devices can now operate at pressures and voltages capable of observing ^{3}He-^{3}He reactions. With a significant amount of work, the system could be properly modified to make statistically sound measurements of beam-gas target reaction rates, and therefore provide high-resolution cross-section data for these reactions at IEC energies. This would involve removing sources of embedded reactions from the view factor of the cathode, and developing a good model to predict ion recirculation. Furthermore, the fourth generation detection system described in this thesis, or something superior, would have to be used to eliminate background radiation from contributing to the detected count rate.

X.B. Improved Characterization / Development of the Helicon Source

The source developed for this thesis is a high power density, very intense source. It is almost certainly operating at an extraordinarily low efficiency, and a campaign to study this would be useful for a number of applications. Helicon sources are appearing everywhere from scientific research to industrial plasma processing to space propulsion due to their very high ionization efficiency. Still, their behavior is not fully understood, and experiments to characterize this source would be valuable to both the plasma physics and IEC communities. Good probe measurements will likely be very difficult, due to issues described in Chapter VIII, but optical and radio methods could prove invaluable to measuring the source characteristics. Once parameters such as plasma density and electron and ion temperature are understood, it may be possible to do many things, including the possibility of increasing the fraction of He^{++} in the source. This would cause an increase in reaction rates, as well as provide an unavailable capability to the scientific community since there are no steady state high current sources that can do this at the present time.

X.C. Ion Source Application to D-^{3}He Fusion for Near-Term Applications

IEC devices are currently being considered for use as medical isotope generators. Most of the reactions involved require the high energy proton created by D-^{3}He reactions [1]. Recent work [2,3,4] has indicated that for typical IEC operation, most of the D involved in these reactions is tied up in D_3^+ molecules which reduces the energy per nucleon by a factor of three for a given cathode voltage. If the ion source provides a good source of atomic D^+, it is possible there will be a reaction rate enhancement of up to 100 times at 100 kV, simply due to the increase in fusion cross section. This would provide a necessary step forward for a technology that now looks only to be interesting in the lab.

X.D. Modification of Source to Study Converged Core Reactions

The existence of converged core reactions in an IEC device has not yet been shown by any lab. In order for IEC devices to contribute to certain near-term applications, the theoretical efficiency of a converged core configuration must be demonstrated in an actual device. Such a demonstration would require operation at very low pressures and very high currents. While operation at sufficiently low pressure has been demonstrated in this work, much higher ion currents are required for a converged core to form. If the helicon source density stated in chapter VIII is correct, this source should be capable of delivering 600 mA of ion current without an increase in neutral pressure. To do this, a campaign to understand the inefficiency of the present extraction configuration, as well as one to raise the source density by a factor of two, could result in a system that for the first time might observe converged core reactions. Such a discovery would provide valuable insights on the feasibility of IEC systems for the aforementioned applications.

X.E. References

[1] J.W. Weidner, "The Production of ^{13}N from Inertial Electrostatic Confinement Fusion," Master's Thesis, University of Wisconsin-Madison (2003).

[2] G.A. Emmert and J.F. Santarius, "A Charge-Exchange Based Model for the Performance of Gridded, Spherical IEC Devices. Part I: single species atomic ions," University of Wisconsin-Madison (in preparation, 2006).

[3] G.A. Emmert and J.F. Santarius, "A Charge-Exchange Based Model for the Performance of Gridded, Spherical IEC Devices. Part II: molecular ions," University of Wisconsin-Madison (in preparation, 2006).

[4] D. R. Boris, "Plasma Characteristics of the Ion Source Region in the University of Wisconsin Inertial Electrostatic Confinement Fusion Device," *Bulletin of The American Physical Society*, **54**, [7], p.166 (2006).

Appendix A—Fusion Rate Calculations

Beam Background Fusion Rate (Ch. IV Ref. 8)

This calculation is a reference and was intended as a guide to predict the ratio of beam-target to beam-embedded reactions. Chapter IV states that the beam-background reaction rate can be written as $R_{bb} = n_b*I*\sigma(E)*l$, where n_b is the background gas density, I is the ion current (ions/sec), $\sigma(E)$ is the fusion cross section, and l is the path length observed. For the conditions stated (I_{ion}=100 mA, E_{ion}=200 keV, P=27 mPa) they are the following:

$n_b = P / kT = 0.027\ N/m^2 / (1.38 * 10^{-23}\ J/K * 298\ K) = 6.6 * 10^{18}$ atoms / m^3

$I = 0.1\ A / e_c = 0.1\ C/s / 1.6 * 10^{-19}\ C/ion = 6.2 * 10^{17}$ ions / sec

$\sigma(E) = 10^{-28} * (5.57-8.24*(E/2) + 15.8*(E/2)^2)/((E/2)*(2.718\verb|^|(4.86/(E/2)^{1/2}))) =$

$1.04 * 10^{-33}\ m^2$ (Fit from reference 2, chapter 4—E is in center of mass MeV)

l = 0.2 m

$R = 6.6 * 10^{18}$ atoms / $m^3 * 6.2 * 10^{17}$ ions / sec $* 1.04 * 10^{-33}\ m^2$ / atom * 0.2 m =

850 reactions / sec

Beam Embedded Fusion Rate (Ch. IV Ref. 9)

From chapter IV, the embedded fusion reaction rate can be written as: $R_{emb} = \int I*n_{emb}*\sigma(E)*dl$. I is the ion current, in ions / sec and is constant over the integral. N_{emb} is the embedded density, which is based on experimental data from ref. 3, chap. IV and is also constant. The energy of the particle as it travels into the wire is found numerically using the stopping power of the grid material taken from the NIST database, adapted for

[3]He. The path length into the material was divided into steps of dl = 0.01 μm and the energy of the ion at each step was decreased from the previous by the stopping power A(E) at the current step. The recursion relation for this is:

$E_n = E_{n-1} - A(E_{n-1}) * dl$, where n is the step number into the material, and $E_{n=0}$ is the initial ion energy. This gives the ion energy as a function of path length into the grid, and the fusion rate at each step size can be evaluated as though the energy were constant over that step. The fusion rate in each incremental step is $I*n_{emb}*\sigma(E_n)*dl$, and these steps are summed until the cross section is negligible. An expression for the total fusion rate in the grid for I_{cath}=10 mA, E_{ion}=200 keV, $n_{emb}=3.5 * 10^{27} / m^3$ is:

$R_{emb}=\sum I*n_{emb}*\sigma(E_n)*dl$

The calculations were carried out in excel, and for the conditions in chapter IV, the results are displayed below:

Table A-1: Theoretical Embedded Fusion Calculation at 200 keV

Distance into grid (um)	Energy of Particle (MeV)	Stopping Power (MeV/cm)	sigma (barns)	Incremental fusion rate
0	0.2	4.00E+03	1.03924E-05	1702.2686
0.01	0.195997574	3.97E+03	9.09076E-06	1489.0669
0.02	0.192029861	3.93E+03	7.92678E-06	1298.4069
0.03	0.18809696	3.90E+03	6.88898E-06	1128.4152
0.04	0.184198971	3.86E+03	5.96655E-06	977.32113
0.05	0.180335998	3.83E+03	5.1493E-06	843.45549
0.06	0.176508144	3.79E+03	4.42765E-06	725.24925
0.07	0.172715515	3.76E+03	3.79262E-06	621.23174
0.08	0.168958218	3.72E+03	3.23583E-06	530.02855
0.09	0.165236362	3.69E+03	2.74945E-06	450.35932
0.1	0.161550058	3.65E+03	2.32622E-06	381.03511
0.11	0.157899418	3.61E+03	1.95944E-06	320.9556
0.12	0.154284557	3.58E+03	1.64289E-06	269.10607
0.13	0.150705591	3.54E+03	1.3709E-06	224.55414
0.14	0.147162638	3.51E+03	1.13826E-06	186.44635
0.15	0.143655818	3.47E+03	9.40199E-07	154.00458

0.16	0.140185254	3.43E+03	7.72419E-07	126.52231
0.17	0.136751071	3.40E+03	6.31018E-07	103.36083
0.18	0.133353395	3.36E+03	5.12486E-07	83.945277
0.19	0.129992354	3.32E+03	4.1368E-07	67.760728
0.2	0.126668082	3.29E+03	3.31796E-07	54.348187
0.21	0.123380711	3.25E+03	2.64351E-07	43.300613
0.22	0.120130377	3.21E+03	2.09151E-07	34.258979
0.23	0.116917221	3.18E+03	1.64276E-07	26.908382
0.24	0.113741383	3.14E+03	1.28048E-07	20.974246
0.25	0.110603009	3.10E+03	9.90149E-08	16.218636
0.26	0.107502246	3.06E+03	7.59261E-08	12.436694
0.27	0.104439244	3.03E+03	5.77121E-08	9.453245
0.28	0.101414157	2.99E+03	4.3465E-08	7.1195599
0.29	0.098427143	2.95E+03	3.24195E-08	5.3103091
0.3	0.095478361	2.91E+03	2.3936E-08	3.9207143
0.31	0.092567976	2.87E+03	1.74842E-08	2.8639048
0.32	0.089696154	2.83E+03	1.26281E-08	2.0684869
0.33	0.086863069	2.79E+03	9.01299E-09	1.4763276
0.34	0.084068894	2.76E+03	6.35258E-09	1.040552
Total fusion rate				
12000				

This shows an embedded fusion rate of 1.2 * 10^4 reactions / sec for this case

Embedded Fusion Rate (Ch. VIII Ref. 3,4)

For these calculations, the above process is repeated at a lower voltage. A table of results for the two voltages of interest is attached:

Table A-2: Theoretical Embedded Fusion Calculation at 124 keV

Distance into grid (um)	Energy of Particle (MeV)	Stopping Power (MeV/cm)	sigma (barns)	Incremental fusion rate
0	0.124	3.26E+03	2.76112E-07	45.227161
0.01	0.120742647	3.22E+03	2.18751E-07	35.831355
0.02	0.117522444	3.18E+03	1.72057E-07	28.182973
0.03	0.114339533	3.15E+03	1.34311E-07	22.000094
0.04	0.111194058	3.11E+03	1.04018E-07	17.038125
0.05	0.108086165	3.07E+03	7.98914E-08	13.086215
0.06	0.105016005	3.03E+03	6.08292E-08	9.9638244
0.07	0.101983731	2.99E+03	4.58941E-08	7.5174591
0.08	0.098989499	2.96E+03	3.42954E-08	5.6175861
0.09	0.09603347	2.92E+03	2.53709E-08	4.1557467
0.1	0.093115805	2.88E+03	1.85707E-08	3.0418744
0.11	0.090236673	2.84E+03	1.34421E-08	2.201823
0.12	0.087396243	2.80E+03	9.61606E-09	1.57511
0.13	0.084594691	2.76E+03	6.7941E-09	1.1128739
0.14	0.081832196	2.72E+03	4.73775E-09	0.7760429
0.15	0.07910894	2.68E+03	3.2583E-09	0.5337098
0.16	0.076425111	2.64E+03	2.20821E-09	0.3617047
0.17	0.073780901	2.60E+03	1.47347E-09	0.241354
0.18	0.071176508	2.56E+03	9.67126E-10	0.1584153
Total fusion rate (reactions / sec)				
199				

Table A-3: Theoretical Embedded Fusion Calculation at 134 keV

Distance into grid (um)	Energy of Particle (MeV)	Stopping Power (MeV/cm)	sigma (barns)	Incremental fusion rate
0	0.134	3.37E+03	5.33526E-07	87.391605
0.01	0.130631947	3.33E+03	4.31176E-07	70.626624
0.02	0.127300636	3.29E+03	3.46259E-07	56.717244
0.03	0.124006201	3.26E+03	2.76232E-07	45.246803
0.04	0.120748778	3.22E+03	2.18849E-07	35.847396
0.05	0.117528505	3.18E+03	1.72137E-07	28.195985
0.06	0.114345523	3.15E+03	1.34375E-07	22.010574
0.07	0.111199977	3.11E+03	1.04069E-07	17.046502
0.08	0.108092013	3.07E+03	7.9932E-08	13.09286
0.09	0.105021781	3.03E+03	6.08611E-08	9.9690521
0.1	0.101989435	2.99E+03	4.5919E-08	7.5215365
0.11	0.098995132	2.96E+03	3.43146E-08	5.6207376
0.12	0.096039029	2.92E+03	2.53856E-08	4.1581595
0.13	0.093121292	2.88E+03	1.85818E-08	3.0437032
0.14	0.090242087	2.84E+03	1.34505E-08	2.2031946
0.15	0.087401584	2.80E+03	9.62227E-09	1.5761273
0.16	0.084599958	2.76E+03	6.79865E-09	1.1136195
0.17	0.081837388	2.72E+03	4.74104E-09	0.7765826
0.18	0.079114058	2.68E+03	3.26066E-09	0.5340955
Total fusion rate (reactions / s)				
413				

Appendix B: Inductance calculations

For wirewound resistors:

Inductance of resistors dominates all other parts of the circuit. The resistors are 3.9 cm in diameter, 24 cm long and have 1350 turns of wire. The inductance of a resistor is:

$$L = \frac{\mu_o N^2 A}{l} = \frac{\mu_o * 1350^2 * 6.6 * 10^{-4} m^2}{0.24m} = 6.3mH$$

The circuit is made up of 4 series sets of two parallel resistors. Inductance in parallel adds like:

$$\frac{1}{L_{total}} = \frac{1}{L_1} + \frac{1}{L_2} + \cdots \frac{1}{L_n}$$

Which means each parallel set has 3.15mH, and the four sets in series add to give a total inductance of 12.6mH

For carbon resistors:

Inductance is now low enough that effects of coaxial cable must be included. There are two pieces of cable and the resistors themselves. The first piece of cable is 4.6 m long, and has an inner conductor diameter of 5mm and an outer conductor diameter of 20mm. The second piece is 3.7 m long and has an ID of 6.6mm and an OD of 25mm. The resistors are each 0.25m long and have a diameter of 29mm and are enclosed in a conductive drum with diameter 580mm. The inductance for each is calculated below assuming all current returns through the shields:

The first piece of cable:

$$L = \frac{\mu_o l}{2\pi} \ln\left(\frac{r_o}{r_i}\right) = \frac{\mu_o * 4.6m}{2\pi} \ln\left(\frac{20mm}{5mm}\right) = 1.3 * 10^{-6} H$$

The second piece:

$$L = \frac{\mu_o l}{2\pi} \ln\left(\frac{r_o}{r_i}\right) = \frac{\mu_o * 3.7m}{2\pi} \ln\left(\frac{25mm}{6.6mm}\right) = 1.0 * 10^{-6} H$$

The resistors in the barrel—each resistor is:

$$L = \frac{\mu_o l}{2\pi} \ln\left(\frac{r_o}{r_i}\right) = \frac{\mu_o * 0.24m}{2\pi} \ln\left(\frac{580mm}{29mm}\right) = 0.14 * 10^{-6} H$$

And the combination of the four series sets of parallel resistors gives:

$$L = 4 * \left(\frac{1}{0.14 * 10^{-6}} + \frac{1}{0.14 * 10^{-6}}\right)^{-1} = 0.28 * 10^{-6} H$$

Giving a total inductance of 2.6*10^{-6} H

It is possible that the current that returns to the power supply can do so by a route other than through the shield. This is the result of redundant grounding that is necessary for the safety of the people working on the experiment. In the worst case, no current travels through the shield, the inductance of the buffer circuit would look as if all the wires were unshielded. In this case the inductance is dominated by the two cable sections. The inductance of a solid conductor in space can be expressed as:

$$L = 2*10^{-7}*l\left(\ln\left(\frac{2*l}{r}\right)-1\right)$$

For the first section of wire this gives:

$$L = 2*10^{-7}*4.6m\left(\ln\left(\frac{2*4.6m}{0.005m}\right)-1\right) = 6\mu H$$

And for the second:

$$L = 2*10^{-7}*3.7m\left(\ln\left(\frac{2*3.7m}{0.0066m}\right)-1\right) = 4.5\mu H$$

In which case the total inductance is 10.5 μH

Appendix C—Langmuir Probe Layout and Readings

Figure C-1: Langmuir Probe Inside Helicon Source

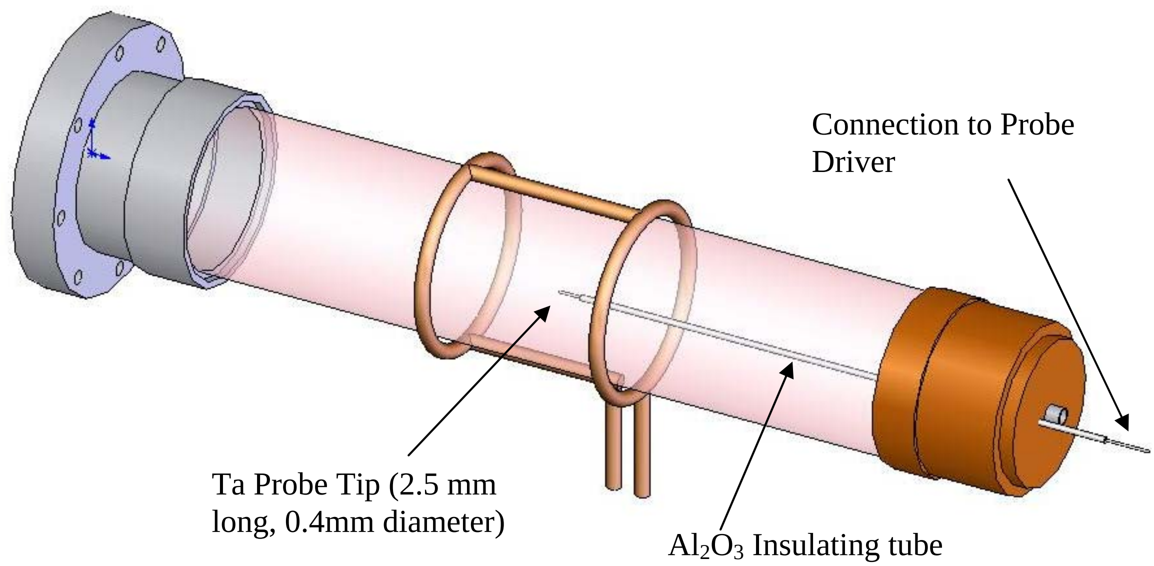

The helicon source assembly with Langmuir probe installed is shown above. At typical run power levels, both the Al_2O_3 tube and Ta probe would melt. Some I-V curves taken with lower power settings are shown in the pages that follow. Complications due to the external magnetic field made these readings very difficult to interpret, and therefore no reliable calculation of source density and temperature was made.

Figures C-2: Langmuir Probe I-V Curves from He in Helicon Source

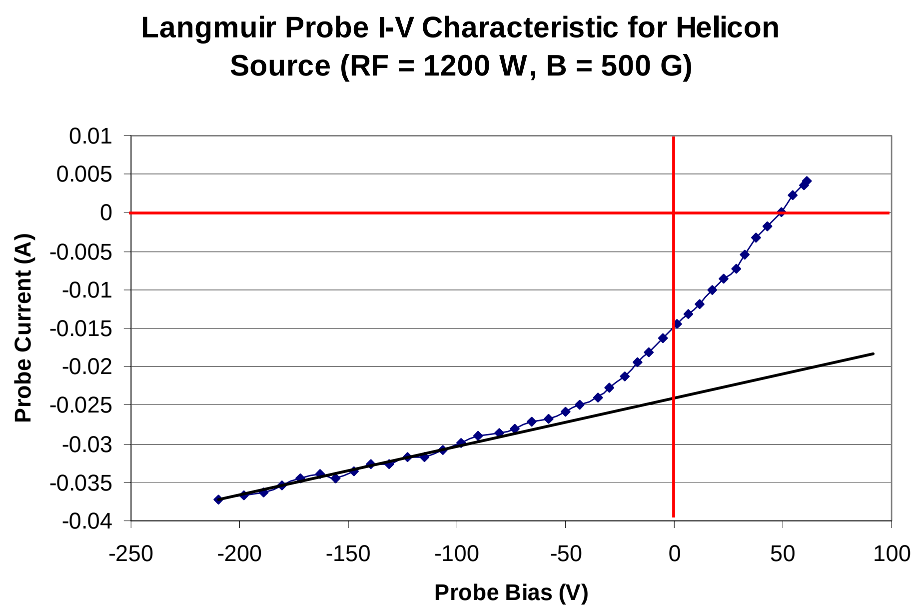

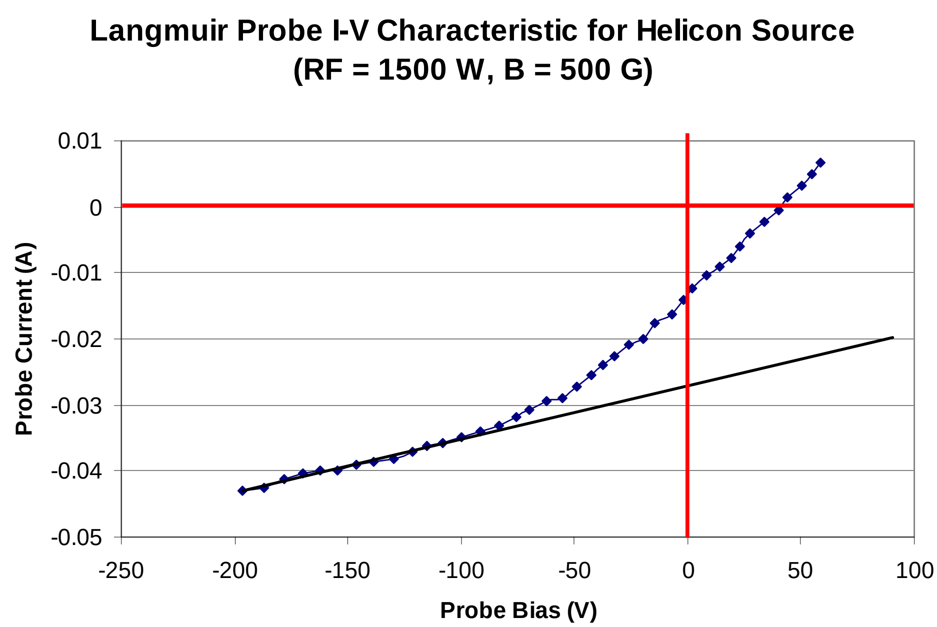

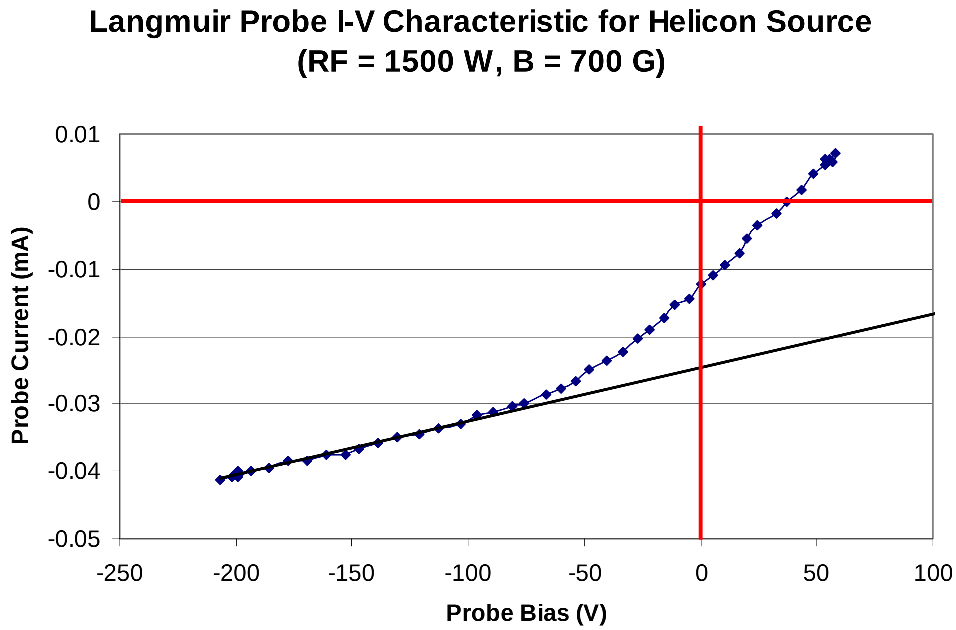
Langmuir Probe I-V Characteristic for Helicon Source
(RF = 1500 W, B = 700 G)
Probe Current (mA)
0.01
0
-0.01
-0.02
-0.03
-0.04
-0.05
-250
-200
-150
-100
-50
0
50
100
Probe Bias (V)

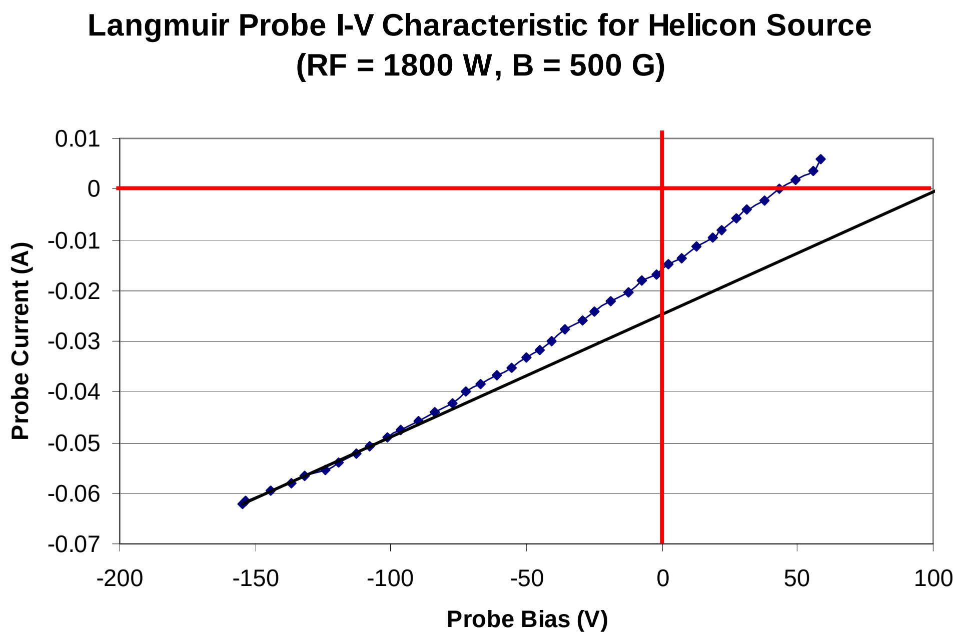
Langmuir Probe I-V Characteristic for Helicon Source
(RF = 1800 W, B = 500 G)
Probe Current (A)
0.01
0
-0.01
-0.02
-0.03
-0.04
-0.05
-0.06
-0.07
-200
-150
-100
-50
0
50
100
Probe Bias (V)

Langmuir Probe I-V Characteristic for Helicon Source (RF = 1800 W, B = 700 G)

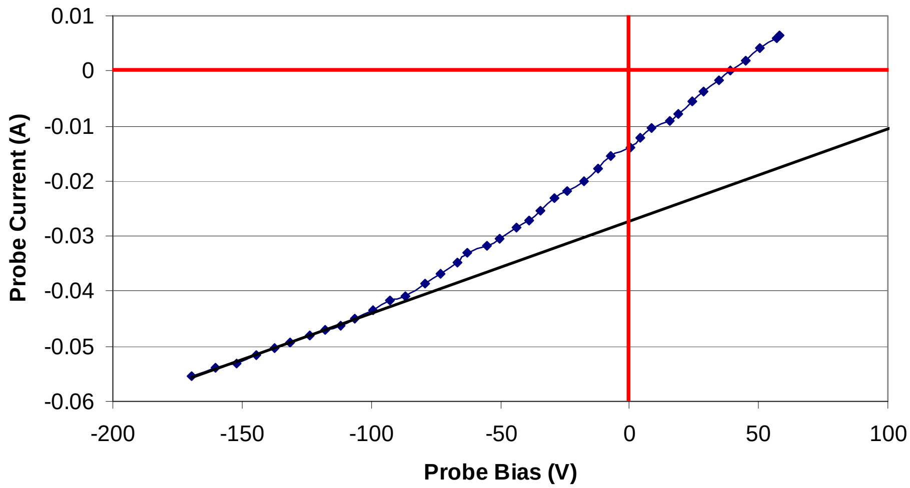

Langmuir Probe I-V Characteristic for Helicon Source (RF = 1800 W, B = 900 G)

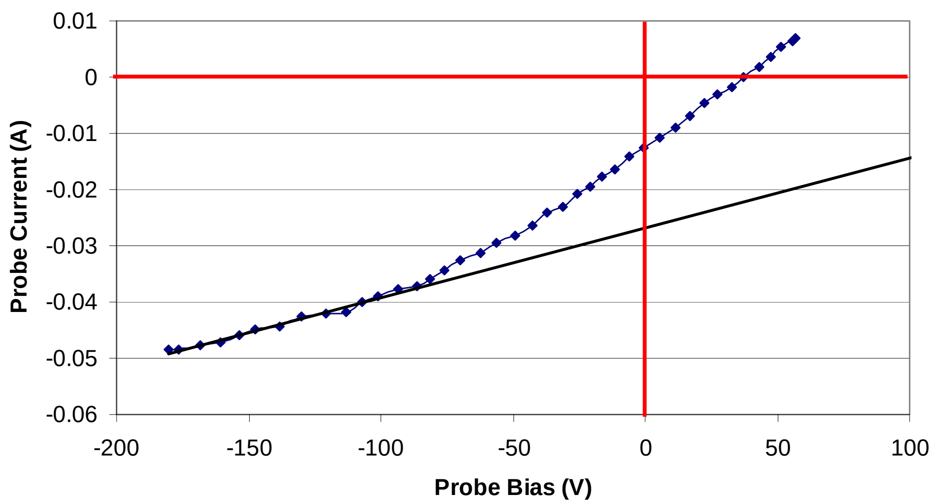

Appendix D

Table D-1: Major Emission Lines from He in Helicon Source @ RF = 2200 W, B = 1200 G

Line (nm)	Relative Intensity
587.1	3155
587.3	2511
587.6	765
667.3	449
706.0	364
586.8	355
587.8	213
501.1	183
667.6	163
706.2	124
388.3	120
588.1	105
501.4	93
667.0	82
446.7	80
586.5	68
386.6	68
583.3	65